X-RAY ABSORPTION SPECTROSCOPIC ANALYSIS OF METAL-CONTAINING PROTEINS AND PEPTIDES

by

JACOB ESTES SHOKES

(Under the Direction of ROBERT A. SCOTT)

ABSTRACT

X-ray absorption spectroscopy (XAS) was used to characterize the binding sites of numerous transition metals in different proteins and peptides providing detailed structural and/or functional information about the system. In particular, it resulted in direct structural evidence of an Fe-Se interaction in heterodisulfide reductase reacted with CoM-SeH, further validating the proposed mechanism of Duin and colleagues involving the direct attachment of CoM-SH to an iron, thus forming a $[4Fe\text{-}4S]^{3+}$ cluster with a five-coordinate Fe site. Studies on metals in fibril formation presented vital structural details of Zn(II) and Cu(II) complexes along the self-assembly pathway, which is crucial for understanding and possible prevention of amyloid formation at the early stage of Alzheimer's disease. Additionally, studies on heavy metal responsive regulator proteins have provided a framework for understanding metal selectivity helping to bridge the gap between inorganic and biological chemistry that can be applied to the understanding of nature's selection process. Other biological systems that were studied include purine hydroxylase, heavy metal resistance proteins, and iron-sulfur cluster proteins.

INDEX WORDS: X-ray absorption spectroscopy, XAS, metalloenzymes, metalloprotein, EXAFS, amyloid, heterodisulfide reductase, heavy metal

X-RAY ABSORPTION SPECTROSCOPIC ANALYSIS OF METAL-CONTAINING PROTEINS AND PEPTIDES

by

JACOB ESTES SHOKES

B.S., The Florida State University, 2000

A Dissertation Submitted to the Graduate Faculty of The University of Georgia in Partial Fulfillment of the Requirements for the Degree

DOCTOR OF PHILOSOPHY

ATHENS, GEORGIA

2006

X-RAY ABSORPTION SPECTROSCOPIC ANALYSIS OF METAL-CONTAINING PROTEINS AND PEPTIDES

by

JACOB ESTES SHOKES

Major Professor: Robert A. Scott

Committee: Marly K. Eidsness
Richard B. Meagher

Electronic Version Approved:

Maureen Grasso
Dean of the Graduate School
The University of Georgia
August 2006

DEDICATION

To my wonderful family

AKNOWLEDGMENTS

With but a few words, I can't possibly thank all who have helped and pushed me in my quest for knowledge. Here I can recognize those whose dedication and support was unwavering throughout the years. To these people, and to all whose names do not appear, yet whose actions and generosity have made my pursuit in school and life more successful and enjoyable, thank you. In particular, I am indebted to the following:

To my parents, whose endless love and support has kept me focused allowing me to achieve my goals in school, as well as life, who have shown me the importance of family and commitment, and who have always been a tremendous source of inspiration and pride. To my brother and his loving wife for their incredible support and motivation, and with whom I look forward to spending many years to come, high-five. To Robert Scott, an inspiring teacher and role model, who taught me the value of self-motivation and organization. To Marly Eidsness, for serving on my advisory committee and for all the helpful advise and guidance. To the Scott group members (i.e. Nate), who helped me become a better scientist. To all the friends I've made in the chemistry department and throughout Athens (including the McCormicks) that have accepted me and made my stay in Athens more enjoyable. To all my friends growing up, who never stopped being my friend, even through the strongest Hurricanes, I salute you. Lastly to Glenna Mae, I miss you.

TABLE OF CONTENTS

CHAPTER 1

INTRODUCTION

Overview of X-ray Absorption Spectroscopy

Investigating the coordination geometries of metal sites in biomolecules is vital for understanding their structural and functional significance in biology. This understanding is formulated with information obtained from a number of scientific techniques and instrumentation including, nuclear magnetic resonance (NMR), x-ray absorption spectroscopy (XAS), atomic absorption spectroscopy (AAS), circular dichroism (CD), resonance raman (RR), electron-nuclear double resonance (ENDOR) etc. In particular, XAS takes advantage of photons in the x-ray region of the electromagnetic spectrum making it an effective tool for extracting direct local structural information about elements from a wide variety of materials, including biological, solid state, surfaces, and other amorphous solids. XAS experiments can provide information about the electronic structure (oxidation states, spin-states, and orbital occupancies) and molecular structure (type of ligands and metric parameters) of a *specific element*, offering a fundamental link between electronic and molecular structural information in coordination chemistry (Scott 1985; Penner-Hahn 1999).

X-ray absorption edges. X-ray photons (~10^4 eV) display wavelengths on the Angstrom (Å) scale making them useful in probing the molecular structure of a system (e.g. x-ray diffraction). In XAS, when the well-defined photon energy is equal to the ionization energy of a core electron in an absorbing atom it triggers *photo*ionization of the electron to the continuum. At this point a discontinuity can be observed in the x-ray absorption spectrum commonly

referred to as an x-ray absorption edge (Figure 1.1). Absorption edges are classified according to the electronic orbital from which the electron is ejected (1s for *K* edges, 2p for L_{II}, L_{III} edges) (Penner-Hahn 1999). All elements have different ionization energies for each orbital allowing for a monochromatically tunable light source to investigate the absorption edges of every element after and including sulfur. In addition, this sensitivity results in differences in absorption edge position and shape of an element, depending on its oxidation state, structural arrangements, and/or ligand composition. As a result, comparison of absorption edge shapes and patterns and qualitative curve-fitting analysis can be valuable in predicting the charge of the absorbing atom, electronic configurations, and site symmetry of a particular element.

Chemical processes can affect the shape and position of an absorption edge; for example, a change in redox state of a metal site generally causes a shift in edge position. The energy of the edge position typically increases with an increase in oxidation state of the metal (Scott 1985). Reduction in metal clusters (e.g. Cu-S and Fe-S clusters) can also result in edge shifts to lower energy. Figure 1.1 compares the Fe K edge data for two Rieske-type, archaeal sulredoxin samples (oxidized and dithionite-reduced) prepared by Dr. Toshio Iwasaki of Nippon Medical School. Compared to oxidized sulredoxin (dashed), the dithionite-reduced sample (solid) clearly

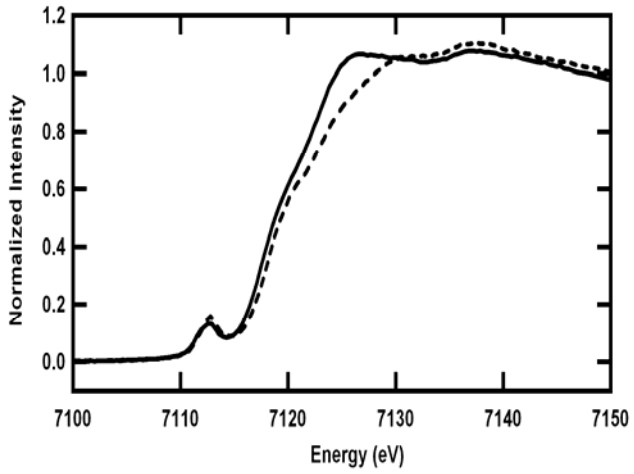

Figure 1.1. Fe K-edge X-ray absorption edge spectra for oxidized sulredoxin (dashed) and dithionite-reduced sulredoxin (solid) at pH=6.8. 1s→3d pre-edge transition peak is located at ca. 7112 eV.

reveals a shift to lower energy upon reduction of the Rieske [2Fe-2S] cluster (Iwasaki, Shokes et al. Submitted for publication).

Transition metals can exist in many coordination environments that give rise to different edge positions, pre-edge peaks, and shoulders in the absorption edge. First row transition metals can produce bound-state electronic transitions (1s→3d and 1s→4p) generating weak transitions (peaks and shoulders) on the low energy side of absorption edges (Penner-Hahn 1999). Thus, with the help of qualitative curve-fitting and knowledge of selection rules, these pre-edge features can be used to help assign the electronic and geometric structure of the metal site. In Figure 1.1, the pre-edge features at ca. 7113 eV in both data sets are assigned to 1s→3d transitions of two tetrahedral Fe centers in the Rieske clusters (Iwasaki, Shokes et al. Submitted for publication).

Finally, edge shifts have been assigned to a change in ligand composition (e.g. S_4 vs. S_2N_2) where soft ligands usually result in a decrease in edge energy (Scott 1985). Consequently, it is not always obvious whether a change in edge position or shape is a result of a bound-state transition, ligand composition, or oxidation-reduction. However, with precise sample preparation, well-designed experiments, and reliable analysis techniques, it is possible to provide reasonable explanations for absorption edge shifts and changes (e.g. among K edges).

EXAFS. The energy region 30-1100 eV above the absorption edge is referred to as the Extended X-Ray Absorption Fine Structure (EXAFS). The physical interaction of the emitting photoelectron with electron density surrounding nearby atoms influences the absorption coefficient by causing fractional modulations in the EXAFS pattern (approximately sinusoidal waves) that encode structural information about a metal and its surrounding atoms. The basis of EXAFS theory is electron scattering and how different scattering atoms present different phase

shifts and backscattering amplitudes based on their electron density. These wave characteristics can be resolved to give information about the coordination site, associating amplitude with atomic number and coordination number, frequency with the metal-ligand distance, and phase with atomic number (Scott 1985; Penner-Hahn 1999).

The interactions dictating the EXAFS of a sample are normally split into different "shells" based on their distance from the absorbing atom. Assignment of "shells" can be accomplished by investigation of the Fourier transform (FT) plot of the theoretical EXAFS, which gives a straightforward, radial distribution analysis of the metal-ligand interactions. Ligands that contain multiple "shells" (e.g. imidazole ligands) will contribute numerous, complex scattering pathways, called multiple scattering pathways. These multiple scattering pathways depend directly on the distances and bond angles in the pathway of interest (pathways consist of 3-5 atoms within a radius of 6Å from the metal atom) and play an important role in analyzing EXAFS data. Our group regularly utilizes published procedures form Ferreira et al. (Ferreira, Franco et al. 2002) to analyze data representing metal sites with ligands that contribute multiple scattering interactions.

Another trait affecting EXAFS is that heavier atoms generate increased scattering power compared to lighter elements (Scott 1985). For example, in the presence of a large number of sulfur scattering atoms it is difficult to accurately predict the number of oxygen/nitrogen backscatterers bound to a particular metal because sulfur backscattering always dominates the EXAFS spectrum. This phenomenon inspired the development of a comparative curve-fitting analysis designed by Dr. James Penner-Hahn and co-workers (Clark-Baldwin, Tierney et al. 1998), that predicts the coordination shell, $ZnS_x(N,O)_{4-x}$, of 4-coordinate Zn sites with two shells of sulfur and other light scattering atoms based on theoretical fits of the EXAFS data. Our lab

frequently assigns this analysis to biological samples that have metal sites directly bound to both sulfur and nitrogen/oxygen ligands (Colangelo, Lewis et al. 2000). For example, in chicken GATA-L-CF (hypothesized to contain Zn in a predominantly sulfur environment) from the GATA family of zinc finger-like transcription factors, we utilize this comparative analysis to better define x in a model $ZnS_x(N,O)_{4-x}$ coordination sphere for the sample. Figure 1.2 illustrates how data for Zn-GATA is most similar to ZnS_4 model compound data, strengthening the EXAFS curve-fitting results (Ghering, Shokes et al. 2004).

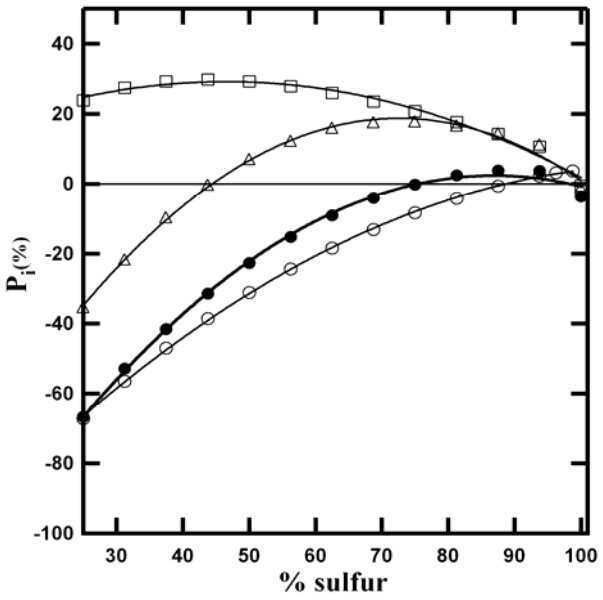

Figure 1.2. Percent improvement, P_i plotted as a function of percent sulfur. Dotted lines represent third-order polynomial fits to the model complexes for ZnS_4 [(open circles), Z_3N_1(open triangles) and ZnS_2N_2 (open squares) Zn EXAFS fits. The solid

Detailed curve-fitting analysis of EXAFS data can provide information about *how many* of *what type* of ligands are at *what distance* from the metal. EXAFS analysis has the ability to determine metal-ligand distances and coordination numbers with an accuracy of ±0.01 Å and ca. 25%, respectively. Therefore, combining information obtained from x-ray absorption edges and EXAFS, a detailed examination of the local structural environment of an element can be provided.

Advantages and capabilities. XAS has advantages over other structural techniques (e.g. small molecule crystallography) by providing information about oxidation state and spin-state of an element. There is no requirement for a metal to reside in a specific chemical state

(oxidation/spin state); XAS has no "blind spots", detecting all occurrences of a given element in the sample. It should be noted that, for spectroscopically dilute samples, x-ray fluorescence excitation is utilized for its superior sensitivity. XAS also has no need for samples with long-range order, and all samples discussed herein are non-crystalline systems. Recent advances in performance conditions and experimental setups of synchrotron radiation sources currently allows for the characterization of solutions with metal concentrations in the sub-millimolar range.

XAS data are often utilized to reveal if addition of a particular substance to a system results in a structural change at the metal site. We take advantage of this by addition of substrate analogs and inhibitors (e.g. cyanide) to the sample. For example, in collaboration with Dr. William Self and coworkers, our lab recently performed experiments of this type with purine hydroxylase (PH), a selenium-dependent molybdenum hydroxylase from *Clostridium purinolyticum*. PH catalyzes the hydroxylation of hypoxanthine (HX) to produce xanthine during the fermentative conversion of purine to uric acid (Self and Stadtman 2000). Spectroscopic characterization of the enzyme revealed the presence of a molybdenum cofactor, and subsequent experiments with cyanide confirmed the presence of a dissociable selenium moiety (Self, Wolfe et al. 2003).

EPR experiments utilizing the hypoxanthine-reduced form of PH have revealed the presence of a Mo(V) center and two different [2Fe-2S] clusters, while experiments utilizing ^{77}Se revealed no detectable interaction between Mo and Se (Self, Wolfe et al. 2003). Thus, we employed X-ray absorption spectroscopy to generate direct structural information on the Mo, Se, and Fe sites in as isolated PH, hypoxanthine (HX)-treated PH, and KCN-treated PH. Spectroscopic investigation of the Mo sites revealed that upon addition of HX, the Mo site is

slightly reduced with no detectable change in coordination environment. The Mo coordination environment in both samples is most consistent with a model that contains two short oxygens ligands, two sulfur ligands, and one solvent ligand. The KCN-treated sample also revealed similar XAS plots for Mo suggesting no direct interaction between Mo and Se. Se XAS suggests that Se does not detect a Mo in its coordination environment and Se directly binds to the CN^- ion. The Fe K edge indicated a reduction in the Fe centers upon addition of substrate to as isolated PH.

XAS has shown some success in determining the individual percentages of different element species and oxidation states in a system. For example, in collaboration with Dr. Richard Meagher of the Department of Genetics at UGA, XAS data were used to investigate the speciation of arsenic in transgenic plants samples (aqueous As(III) vs. As(V) vs. $As(III)(GS)_3$, GSH = glutathione) used for phytoremediation in As-contaminated sites. The plants contained an insert of a yeast arsenate reductase gene, *AtACR2* from *Arabidopsis thaliana*. Three samples were investigated, one wild-type and two RNAi knockdown plant lines, and the As K edge spectra illustrate that none of the plant samples contain significant arsenate. The wild-type sample was estimated to contain ~37% arsenite, while both AtACR2Ri knockdown plants were estimated to contain ~17% arsenite (the remaining component was determined to consist mainly of $As(III)(GS)_3$) (Dhankher, Rosen et al. Submitted for publication).

Limitations. Several limitations in experimental resolution of XAS are widely known and accepted by experimenters. They include its inability to give the exact geometric arrangement of ligand atoms (no angular resolution), as well as its inability to distinguish between scattering atoms closely related in atomic number (e.g. C, N, O). The range of detection (k_{max} = 12-18 $Å^{-1}$) is limited by the small signal-to-noise ratio encountered as one ventures further away from the

absorption edge. It is common to find two shells of atoms at similar distances from the absorbing atom that will introduce a "damping factor" in the EXAFS making it difficult to resolve individual shells/atoms. Furthermore, single and multiple scattering components can cause "interference" in the EXAFS yielding even more complex spectra. High energy X-rays can inflict radiation damage to a sample, possibly causing complete destruction of the metal site or "photoreduction" of the metal center (e.g. Cu(II)→Cu(I)). It is common practice to keep samples at cryogenic temperatures and to investigate the integrity of a sample during and after the data collection. Detector saturation and collection time (one sample averaging four, 20-min scans) also limit the effectiveness of XAS.

The focus of my research utilizes XAS to characterize the binding site of numerous transition metals in different proteins and peptides and to use this information to develop structure-function relationships, as well as any implications it has to biochemistry, molecular toxicology, and other chemical aspects. The ability to apply these implications to biology first requires knowledge of heavy metals and metalloids and how they interact and co-exist (often as metalloproteins) with organisms and the environment.

Introduction to heavy metals, metalloids, and metalloproteins found in humans and the environment

Heavy metals are metals and metalloids that have a reasonably high density (> 4.5 g/cm^3) and occur naturally in the Earth's crust. As elements, heavy metals are indestructible (cannot be completely degraded or destroyed) and have potential to be extremely toxic at low concentrations. Numerous natural and artificial forms of heavy metals are found in humans and can be classified as essential (Fe, Se, Zn), beneficial (Mn, Ni, V), or toxic (Cd, Pb, Hg). Toxic metals are of major concern because they can cause neurotoxicity, immunotoxicity, and

carcinogenic affects in humans. Some carcinogenic metals even have the ability to imitate essential metals invading important molecular sites causing breakdown of essential metal function. For example, the geochemical behavior and binding preferences of arsenic are highly similar to those of phosphorus. It is also important to note that naturally occurring metals exist as reactive species, thus they do *not* require bioactivation or any other activation process (Sarkar 2002). Thus, the adverse health risks of heavy metals and their ability to bioaccumulate in organisms emphasize the importance of not only limiting human exposure, but of developing a way to reduce the toxicity of these metals (together with effective bioremediation techniques).

Since the determination of the first structure of a "metalloprotien" (myoglobin) by John Kendrew and coworkers in 1960, transition metals have been found to play large roles in an ever-increasing number of biological processes (Kendrew 1959). It is estimated that one-third of all known proteins in cells exploit metals either as a cofactor or through incorporation into the molecule. Metals are most commonly utilized in stabilization of the proteins' structure and/or in a functional role, such as electron transport/transfer, small molecule transport/transfer, and binding and activating of substrates. Interestingly, many metal ions can be used for different functions (e.g. protein stability vs. metal transport) because of their versatility to be "tuned" for a specific function by altering binding ligands, coordination geometry, and nearby residues (e.g. H-bonding) (Sarkar 1987; Sarkar 1989). Thus, the direct structural characterization of metal sites in proteins by XAS experiments is crucial for identifying determinants that control and/or influence the binding and activity of protein metal sites.

Selected environmental and medical effects of heavy metals

Over the course of my graduate studies, I have conducted numerous experiments on biomolecules containing metal sites. The success of each project relies on our collaboration with

many researchers around the world. Below, I summarize a few of the major projects which I have taken part in, first discussing the reason for the project and then reviewing the important results of the data obtained indicating any gaps in knowledge that it has filled (a more detailed discussion of each project is presented in subsequent chapters).

Se as an essential component of biological systems. Selenium is a rare trace element that is an essential component of many biological systems, mainly through its incorporation into proteins as selenocysteine. Of particular interest are the selenium-dependent antioxidant enzymes (e.g. glutathione peroxidases) and the potential role selenium plays in preventing cancers in humans (Baraboi and Shestakova 2004). Study of Se in other selenoproteins, such as thioredoxin reductase and purine hydroxylase (described above), is also crucial in determining the molecular role of selenium in biological systems (Self and Stadtman 2000; Zagrodzki 2002). The XAS experiments conducted on PH are currently helping to define the role of Se in the selenium-dependent molybdenum hydroxylase family of enzymes. These are described in detail in Chapter 3.

Se as a spectroscopic probe of sulfur-based enzymology. Selenium can be employed as a spectroscopic probe in systems where a single sulfur atom plays a crucial role, by substitution of the S with Se allowing the site to be structurally characterized by a host of spectroscopic techniques (e.g. EPR, XAS). For example, in methanogenic archaea heterodisulfide reductase (HDR) is an iron-sulfur enzyme that mediates the reversible conversion of the heterodisulfide, CoM-S-S-CoB, into the sulfhydryls CoM-SH and CoB-SH. During methanogenesis, methyl coenzyme M (CH_3-S-CoM) reductase catalyzes the reaction of CH_3-S-CoM with coenzyme B (CoB-SH) producing methane and CoM-S-S-CoB (Duin, Madadi-Kahkesh et al. 2002). The

disulfide product then acts as an electron acceptor of the electron transport chain involved in disulfide respiration (Staples, Gaymard et al. 1998).

Recently, electron paramagnetic resonance (EPR) and varibable-temperature magnetic circular dichroism spectroscopic experiments (performed by Duin and colleagues (Duin, Bauer et al. 2003)) on oxidized HDR incubated with CoM-SH revealed a characteristic S=1/2 $[4Fe\text{-}4S]^{3+}$ cluster, the EPR spectrum of which is broadened in the presence of CoM-^{33}SH (Duin, Bauer et al. 2003). These results provide indirect evidence that the disulfide binds directly to the iron-sulfur cluster during reduction. We report in Chapter 2 Se XAS analysis of HDR treated with the selenium analog of coenzyme M (CoM-SeH) providing direct structural evidence for this interaction (Shokes, Duin et al. 2005).

Se K edge EXAFS confirms a direct interaction of the Se in CoM-SeH-treated HDR with an Fe atom of an Fe-S cluster at an Fe-Se distance of 2.4 Å, suggesting direct binding of the Se (an S in the natural substrate) to an Fe of the Fe-S cluster (Figure 1.3). The XAS data illustrate that the unique Fe-S cluster in HDR mediates cleavage of the heterodisulfide through a direct interaction with the substrate, CoM-S-S-CoB (Shokes, Duin et al. 2005).

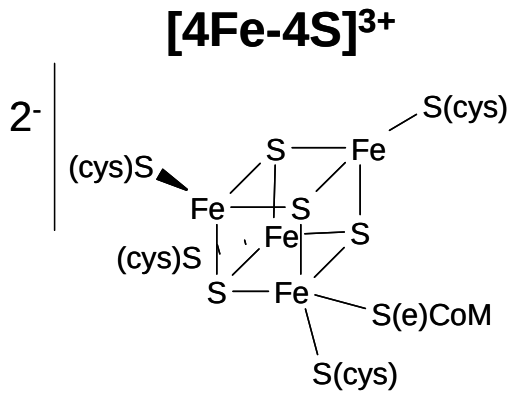

Figure 1.3. Proposed structure of the active site in Hdr +CoM-S(e)H (Shokes, Duin et al. 2005)

Metals in neurodegenerative diseases. Over the last decade, much attention has been given to the neurobiology of metals and the pivotal role they play in a number of neurodegenerative diseases, including: Alzheimer's, Lou Gehrig's, Huntington's, epilepsy, and

multiple sclerosis (Sarkar 2002). In particular, Alzheimer's disease (AD), a progressive irreversible brain disorder, has been associated with amyloid (fibril) formation, a self-assembly process that is thought to contribute to the degradation of neurons in the brain. Understanding the details of fibril formation is not only relevant to treating AD, but could also open the possibility of using self-assembly in the design of new materials with specific properties. The amyloid-β (Aβ) peptide, which is a major component of neuronal plaques found in the brains of AD patients, is formed by proteolytic cleavage of the β-amyloid precursor protein (Selkoe 1994; Selkoe 1994). These neuronal plaques are the central result of aggregate formation caused by the "misfolding" of the Aβ peptides. Even though the role of amyloid plaques in AD is not currently understood, they do appear as a common fingerprint in its pathogenesis. Interestingly, high amounts of Zn(II) and Cu(II) have been found in amyloid plaques of AD patients. Zn(II) and Cu(II) are proposed to accelerate fibril formation or inhibit self-assembly under particular conditions of pH, respectively (Bush, Pettingell et al. 1994; Atwood, Moir et al. 1998). These findings suggest that metal ions could play an important role in amyloid aggregation, neurotoxicity and neurological disease.

Dr. David Lynn's group at Emory University prepared two synthetic, truncated peptides (Aβ(13-21)K16A, and Ac-Aβ(13-21)H14A) mimicking the aggregation properties of the amyloid-β peptide in hopes of understanding how Zn(II), Cu(II)-histidine binding modulate the structure and kinetics of amyloid formation (Lynn and Meredith 2000). Our group utilized XAS experiments to extend the investigations of Dr. Lynn's group on fibril formation by providing direct structural information about the metal binding sites (including both Zn(II) and Cu(II)) along the self-assembly pathway. The Zn XAS data were most consistent with a Zn-$(imid)_2(N/O)_2$ coordination sphere for both Aβ(13-21)K16A and Ac-Aβ(13-21)H14A peptides.

Additionally, experiments revealed highly similar data for Zn(II) and Cu(II) bound forms of Ac-Aβ(13-21)H14A, as well as Cu(II)-bound Aβ(13-21)K16A, suggesting highly similar coordination environments. We also showed a relationship between Zn(II)-induced misfolding kinetics and the morphology of the resulting fibrils. Together these studies have provided a better understanding for the mechanism of amyloid self-assembly by illustrating that Zn(II) can regulate amyloid morphology via distinct coordination environments and that a single histidine is sufficient for typical amyloid fibril formation (Dong, Shokes et al. 2006). Detailed description of these results can be found in Chapter 4.

SmtB/ArsR family of metalloregulators. In order for organisms to cope with the toxic effects of heavy metals, nature has developed a set of P-type ATPase efflux pumps and metal-sequestering proteins that effectively remove the metals from the cytosol in numerous bacterial genomes (Xu, Zhou et al. 1998). Expression of these pumps is usually under the control of a set of metal-responsive transcriptional regulators. For example, *Staphylococcus aureus* CzrA and *Mycobacterium tuberculosis* NmtR are homologous zinc/cobalt-responsive and nickel/cobalt-responsive transcriptional repressors *in vivo*, respectively, and members of the ArsR/SmtB superfamily of prokaryotic metal sensor proteins (Busenlehner, Pennella et al. 2003). The molecular basis of this metal selectivity is not fully understood. The group of our collaborator, David P. Geidroc (Texas A&M University) has illustrated that Zn(II) is the most potent negative allosteric regulator of the *czr* operator/promoter (O/P), binding *in vitro* with the trend Zn(II)>Co(II)>>Ni(II), while the opposite holds for the binding of NmtR to the *nmt* O/P, Ni(II)>Co(II)>Zn(II) (Pennella, Shokes et al. 2003). Characterization of the metal coordination complexes of CzrA and NmtR by UV/visible and XAS analysis reveals that metals that form 4-coordinate tetrahedral complexes with CzrA [Zn(II) and Co(II)] are potent regulators of DNA

binding, while metals that form 5- or 6-coordinate complexes with NmtR [Ni(II) and Co(II)] are the strongest allosteric regulators in this system. Ni XAS data for NmtR and CzrA are most consistent with a Ni-$(imid)_3(N/O)_3$ coordination environment. The Zn(II) coordination complexes of CzrA and NmtR also cannot be distinguished from one another by XAS, with the best fit a His_3-carboxylate complex in both cases (Pennella, Shokes et al. 2003).

It was concluded that NmtR requires hexacoordinate metal binding (as observed for Ni(II) and Co(II)) to affect allosteric de-repression of transcription, while CzrA requires tetrahedral metal binding (as observed for Co(II) and Zn(II)) to achieve the same biological function. Thus [Zn(II)]NmtR adopts a less effective (tetrahedral) coordination, while [Ni(II)]CzrA is hexacoordinate and similarly ineffective. Nature has adapted the allosteric coupling of metal coordination to DNA binding to take advantage of inorganic coordination preferences. The exact mechanism of this allosteric coupling, and how the coupling must differ for CzrA and NmtR, is still under investigation. However, the XAS data indicate that metal coordination number and geometry play a dominant role in determining which metal ions negatively allosterically regulate operator/promoter binding *in vitro* (Pennella, Shokes et al. 2003). See Chapter 5 for more details.

Baterial resistance to heavy metal ions. High levels of toxic metals in polluted areas have led to evolution of bacteria expressing genes for resistance mechanisms to toxic metals and metalloids. Not only do these genes have the ability to bind and transport heavy metals both intracellularly and across cell membranes, they have been shown to reduce toxic metals to a volatile or non-reactive state (Solioz and Vulpe 1996). These bacteria handle toxic metals using CPx-type ATPases (a subgroup of P-type ATPases) that have a CPx motif in the membrane and a CXXC (heavy-metal associated, HMA) motif for metal binding. The CXXC sequence motif is

deemed the framework necessary for proteins to bind metal ions. HMA motifs are common to Cd, Cu, and Zn resistance CPx-type ATPases and are also found in other heavy metal operons (e.g. *mer* operon) (Solioz and Vulpe 1996).

In collaboration with Dr. Lucia Banci's group at the University of Florence, XAS experiments were used to investigate the coordination sphere of the Cd-detoxifying P1-type ATPase, CadA. Two samples were prepared, CadA and CadA in the presence of TCEP [tris(2-carboxyethyl)phosphine hydrochloride], and analyzed by Cd XAS. The data revealed predominantly sulfur-containing coordination environments for all Cd(II) ions. In addition, as detailed in Chapter 6, the CadA + TCEP sample contained a small FT peak at 3.7 Å that was tentatively assigned to a Cd-Cd interaction formed by a thiolate-bound Cd(II) dinuclear cluster. The proposed dinuclear model determined by Cd NMR and XAS experiments is shown in Figure 1.4 (Banci, Bertini et al. 2006).

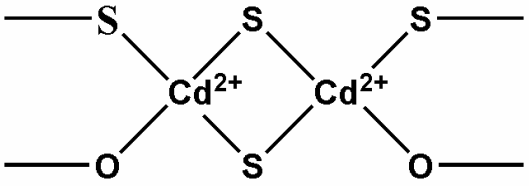

Figure 1.4. The proposed binding model for the Cd(II) dinuclear cluster for CadA + TCEP (Banci, Bertini et al. 2006).

The unique CXXC binding motif also exists in mercury resistance operons, found in certain prokaryotes. These genes make up an intricate detoxification system that is used to shuttle Hg(II) *into* the cell and reduce it to volatile Hg(0). The intracellular process is catalyzed by the mercuric reductase, MerA (in some bacteria in combination with MerB, an organomercurial lyase), which is dependent on NADPH for reduction. Elemental mercury then exits the cell by passive diffusion through the cell membrane. Transcription of the *mer* operon is tightly controlled by the Hg(II)-responsive metallorgulatory protein MerR (Brunker, Rother et al. 1996). Thus, determination of the Hg(II) coordination spheres in these proteins would provide a

more detailed understanding of the mechanistic aspects of the operon, as well as suggest possible engineering methods for bioremediation strategies. Our laboratory has utilized XAS experiments to assign the coordination environment of Hg to the binding motif of MerB in the presence of DTT and MerR to be Hg-S_3 and Hg-S_3, respectively (Benison, Di Lello et al. 2004; Song, Caguiat et al. 2004). A more detailed description of these results is provided in Chapter 6.

References

Atwood, C. S., R. D. Moir, et al. (1998). "Dramatic aggregation of Alzheimer abeta by Cu(II) is induced by conditions representing physiological acidosis." J Biol Chem **273**(21): 12817-26.

Banci, L., I. Bertini, et al. (2006). "Structural basis for metal binding specificity: the N-terminal cadmium binding domain of the P1-type ATPase CadA." J Mol Biol **356**(3): 638-50.

Baraboi, V. A. and E. N. Shestakova (2004). "[Selenium: the biological role and antioxidant activity]." Ukr Biokhim Zh **76**(1): 23-32.

Benison, G. C., P. Di Lello, et al. (2004). "A stable mercury-containing complex of the organomercurial lyase MerB: catalysis, product release, and direct transfer to MerA." Biochemistry **43**(26): 8333-45.

Brunker, P., D. Rother, et al. (1996). "Regulation of the operon responsible for broad-spectrum mercury resistance in Streptomyces lividans 1326." Mol Gen Genet **251**(3): 307-15.

Busenlehner, L. S., M. A. Pennella, et al. (2003). "The SmtB/ArsR family of metalloregulatory transcriptional repressors: Structural insights into prokaryotic metal resistance." FEMS Microbiol Rev **27**(2-3): 131-43.

Bush, A. I., W. H. Pettingell, et al. (1994). "Rapid Induction of Alzheimer a-Beta Amyloid Formation by Zinc." Science **265**(5177): 1464-1467.

Clark-Baldwin, K., D. L. Tierney, et al. (1998). "The limitations of X-ray absorption spectroscopy for determining the structure of zinc sites in proteins. When is a tetrathiolate not a tetrathiolate?" Journal of the American Chemical Society **120**(33): 8401-8409.

Colangelo, C. M., L. M. Lewis, et al. (2000). "Structural evidence for a common zinc binding domain in archaeal and eukaryal transcription factor IIB proteins." Journal of Biological Inorganic Chemistry **5**(2): 276-283.

Dhankher, O. P., B. P. Rosen, et al. (Submitted for publication). "Enhanced long-distance transport and hyperaccumulation of

arsenic in transgenic Arabidopsis silenced for endogenous

arsenate reductase AtACR2 expression."

Dong, J., J. E. Shokes, et al. (2006). "Modulating amyloid self-assembly and fibril morphology with Zn(II)." J Am Chem Soc **128**(11): 3540-2.

Duin, E. C., C. Bauer, et al. (2003). "Coenzyme M binds to a [4Fe-4S] cluster in the active site of heterodisulfide reductase as deduced from EPR studies with the [S-33]coenzyme M-treated enzyme." Febs Letters **538**(1-3): 81-84.

Duin, E. C., S. Madadi-Kahkesh, et al. (2002). "Heterodisulfide reductase from Methanothermobacter marburgensis contains an active-site [4Fe-4S] cluster that is directly involved in mediating heterodisulfide reduction." Febs Letters **512**(1-3): 263-268.

Ferreira, G. C., R. Franco, et al. (2002). "Unraveling the substrate-metal binding site of ferrochelatase: an X-ray absorption spectroscopic study." Biochemistry **41**(15): 4809-18.

Ghering, A. B., J. E. Shokes, et al. (2004). "Spectroscopic determination of the thermodynamics of cobalt and zinc binding to GATA proteins." Biochemistry **43**(26): 8346-55.

Iwasaki, T., J. E. Shokes, et al. (Submitted for publication). "THE pH-DEPENDENT STRUCTURAL TRANSITIONS OF AN ARCHAEAL HIGH-POTENTIAL RIESKE

[2FE-2S] CENTER: RADIOLYTIC CRYOREDUCTION AND X-RAY ABSORPTION SPECTROSCOPIC STUDIES ON SULREDOXIN."

Kendrew, J. C. (1959). "Structure and Function in Myoglobin and Other Proteins." Federation Proceedings **18**(1): 740-751.

Lynn, D. G. and S. C. Meredith (2000). "Review: model peptides and the physicochemical approach to beta-amyloids." J Struct Biol **130**(2-3): 153-73.

Pennella, M. A., J. E. Shokes, et al. (2003). "Structural elements of metal selectivity in metal sensor proteins." Proc Natl Acad Sci U S A **100**(7): 3713-8.

Penner-Hahn, J. E. (1999). "X-ray absorption spectroscopy in coordination chemistry." Coordination Chemistry Reviews **192**: 1101-1123.

Sarkar, B. (1987). "Metal Protein Interactions." Progress in Food and Nutrition Science **11**(3-4): 363-400.

Sarkar, B. (1989). "Metal - Protein Interactions in Transport, Accumulation, and Excretion of Metals." Biological Trace Element Research **21**: 137-144.

Sarkar, B. (2002). Heavy Metals in the Environment. New York, NY, Marcel Dekker, Inc.

Scott, R. A. (1985). "Measurement of metal-ligand distances by EXAFS." Methods Enzymol. **117**: 414-459.

Self, W. T. and T. C. Stadtman (2000). "Selenium-dependent metabolism of purines: A selenium-dependent purine hydroxylase and xanthine dehydrogenase were purified from Clostridium purinolyticum and characterized." Proc Natl Acad Sci U S A **97**(13): 7208-13.

Self, W. T., M. D. Wolfe, et al. (2003). "Cofactor determination and spectroscopic characterization of the selenium-dependent purine hydroxylase from Clostridium purinolyticum." Biochemistry **42**(38): 11382-90.

Selkoe, D. J. (1994). "Alzheimer's disease: a central role for amyloid." J Neuropathol Exp Neurol **53**(5): 438-47.

Selkoe, D. J. (1994). "Amyloid beta-protein precursor: new clues to the genesis of Alzheimer's disease." Curr Opin Neurobiol **4**(5): 708-16.

Shokes, J. E., E. C. Duin, et al. (2005). "Direct interaction of coenzyme M with the active-site Fe-S cluster of heterodisulfide reductase." FEBS Lett **579**(7): 1741-4.

Solioz, M. and C. Vulpe (1996). "CPx-type ATPases: a class of P-type ATPases that pump heavy metals." Trends Biochem Sci **21**(7): 237-41.

Song, L., J. Caguiat, et al. (2004). "Engineered single-chain, antiparallel, coiled coil mimics the MerR metal binding site." J Bacteriol **186**(6): 1861-8.

Staples, C. R., E. Gaymard, et al. (1998). "Role of the [Fe4S4] cluster in mediating disulfide reduction in spinach ferredoxin:thioredoxin reductase." Biochemistry **37**(13): 4612-20.

Xu, C., T. Zhou, et al. (1998). "Metalloid resistance mechanisms in prokaryotes." J Biochem (Tokyo) **123**(1): 16-23.

Zagrodzki, P. (2002). "[Thioredoxin reductase--a new target for molecular medical investigations]." Postepy Hig Med Dosw **56**(2): 155-67.

CHAPTER 2

DIRECT INTERACTION OF COENZYME M WITH THE ACTIVE-SITE FE-S CLUSTER OF HETERODISULFIDE REDUCTASE

[1]Shokes, J. E., Duin, E. C., Bauer, C., Jaun, B., Hedderich, R., Kock, J., Scott, R.A. 2005. FEBS Letters. 579:13302-13309
Reprinted here with permission of publisher.

Abstract

Heterodisulfide reductase (HDR) catalyzes the formation of coenzyme M (CoM-SH) and coenzyme B (CoB-SH) by the reversible reduction of the heterodisulfide, CoM-S-S-CoB. This reaction recycles the two thiol coenzymes involved in the final step of microbial methanogenesis. Electron paramagnetic resonance (EPR) and variable temperature magnetic circular dichroism (VTMCD) spectroscopic experiments on oxidized HDR incubated with CoM-SH revealed a S=1/2 $[4Fe\text{-}4S]^{3+}$ cluster, the EPR spectrum of which is broadened in the presence of CoM-^{33}SH [Duin, EC, et al. (2002) *FEBS Lett.*, **512**, 263-268; Duin, EC, et al. (2003) *FEBS Lett.*, **538**, 81-84.]. These results provide indirect evidence that the disulfide binds to the iron-sulfur cluster during reduction. We report here direct structural evidence for this interaction from Se X-ray absorption spectroscopic (XAS) investigation of HDR treated with the selenium analog of coenzyme M (CoM-SeH). Se K edge EXAFS confirms a direct interaction of the Se in CoM-SeH-treated HDR with an Fe atom of the Fe-S cluster at an Fe-Se distance of 2.4 Å.

Introduction

Heterodisulfide reductase from methanogenic archaea is an iron-sulfur enzyme that mediates the reversible conversion of the heterodisulfide, CoM-S-S-CoB, into the sulfhydryls CoM-SH and CoB-SH. During methanogenesis, methyl coenzyme M (CH_3-S-CoM) reductase catalyzes the reaction of CH_3-S-CoM with coenzyme B (CoB-SH) producing methane and CoM-S-S-CoB. The disulfide product then acts as an electron acceptor of the electron transport chain involved in disulfide respiration (Thauer 1998).

Recent studies reported the observation of a paramagnetic intermediate generated upon half-reaction of the EPR-silent oxidized enzyme with CoM-SH in the absence of CoB-SH (Madadi-Kahkesh, Duin et al. 2001). The S = 1/2 species, designated as CoM-HDR, can be reduced in a one-electron step but not further oxidized. The g-values, 2.013, 1.991, 1.938 (for HDR from *M. marburgensis*), and signal broadening in the ^{57}Fe-enriched enzyme indicated that the intermediate is iron-based. The combination of VTMCD experiments and EPR with ^{33}S-labeled CoM-SH lead to the proposal that the reaction intermediate is a novel substrate-bound $[4Fe\text{-}4S]^{3+}$ cluster with two thiolate ligands at a unique Fe site (Duin, Madadi-Kahkesh et al. 2002; Duin, Bauer et al. 2003). Using ^{57}Fe pulsed ENDOR at two very different frequencies, 9 and 94 GHz, direct evidence was provided that the paramagnetic species in CoM-HDR is a $[4Fe\text{-}4S]^{3+}$ cluster with unusually large ^{57}Fe isotropic hyperfine coupling values that reveal the complex nature of the interaction between the cluster and the CoM-SH substrate (Bennati, Weiden et al. 2004). Taken together these results provide indirect evidence that the reactant disulfide or product CoM-SH binds directly to the iron-sulfur (Fe-S) cluster during the catalytic cycle.

With the substrate analog seleno-coenzyme M (2-selenylethane-sulfonate; CoM-SeH), a similar EPR signal was obtained again indicative for direct binding of the compound to the active-site cluster of HDR (Duin, Bauer et al. 2003). We report herein direct structural characterization of this interaction using Se X-ray absorption spectroscopic (XAS) investigation of HDR incubated with CoM-SeH prepared from CoM-Se-Se-CoM by reduction with dithiothreitol (DTT).

Methods

Synthesis of CoM-SeH. 2-Selenylethanesulfonate (CoM-SeH) was freshly prepared prior to use from the corresponding diselenide (CoM-Se-Se-CoM, synthesized by $NaBH_4$ reduction of 2-selenocyanoethanesulfonate (Duin, Bauer et al. 2003)) by DTT reduction. CoM-Se-Se-CoM (40 mM) and DTT (80 mM) in 2 mL water were incubated for 14 h at room temperature under N_2. CoM-SeH was purified by anion exchange chromatography on Mono Q (0.5 × 5 cm) under anaerobic conditions. The sample was loaded on the column equilibrated with 50 mM MOPS, pH 7. Subsequently the column was washed with 30 mL of this buffer to remove DTT. CoM-SeH and CoM-Se-Se-CoM were separated by applying a linear NaCl gradient (0 to 0.5 M; 60 mL). CoM-SeH was identified and quantified with Ellmans reagent.

Sample preparation. Heterodisulfide reductase was purified from *Methanothermobacter marburgensis* under strictly anaerobic conditions as described (Madadi-Kahkesh, Duin et al. 2001). Protein was judged to be >95 % pure by SDS/PAGE. The protein concentration was determined by using the method of Bradford with bovine serum albumin (Serva) as standard. The method was calibrated by a quantitative amino acid analysis. The CoM-SeH adduct of HDR was made by oxidizing the enzyme (13 mg protein in 1 mL 50 mM Tris/HCl, pH 7.6) with 2 mM duroquinone ($E^{\circ\prime}$ = +86 mV vs. NHE) followed by the addition of 0.5 mM CoM-SeH, and

incubation at room temperature for 30 min. Alternatively, the CoM-Se-HDR adduct was formed by adding a mixture of CoM-Se-Se-CoM (0.8 mM) and DTT (0.4 mM), that had been preincubated for 12 h, to HDR. To remove non-protein bound substrate, the 1-mL samples were diluted to 4.5 mL and concentrated to 0.1 mL by ultrafiltration using Amicon Ultra-4 Centrifugal Filter Units (Millipore) with a 100-kDa cut-off. This washing step was repeated 4 times. The washed protein was finally concentrated to 0.1 mL and ethylene glycol was added to a final concentration of 20%. The final enzyme concentration was 0.8 mM. The sample was loaded into a 24 × 3 × 2 mm polycarbonate cuvet (with one 24 × 3-mm wall consisting of 25μm X-ray-transparent Mylar tape) and immediately frozen in liquid nitrogen.

X-ray absorption spectroscopy. X-ray absorption spectra were collected at the Stanford Synchrotron Radiation Laboratory (SSRL) on beamline 9-3 with the SPEAR2 ring operating at 3.0 GeV, 60-100 mA. Fluorescence excitation spectra were recorded with the sample at 10 K using 1 mm vertically apertured beam incident on a Si[220] double-crystal monochromator that was fully tuned. The averaged XAS data represent 10 scans, each of 21 min duration. EXAFSPAK software (www-ssrl.slac.stanford.edu/exafspak.html) was used for data reduction and analysis, according to standard procedures (Scott 2000). Energy calibration was achieved using the first inflection of the edge of powdered elemental Se (assumed to be 12658 eV). The Fourier transforms (FTs) of the extended X-ray absorption fine structure (EXAFS) data were generated using sulfur-based phase correction. The substrate/product analogs, CoM-Se-Se-CoM and CoM-SeH, were analyzed in the same manner; however, the availability of high substrate concentration in solution (~7.7 mM) produced a higher signal-to-noise ratio for the data, allowing fewer scans to be recorded. The multiple scattering model (designed for the aqueous CoM-SeH sample), calculated using FEFF version 8.2 (Ankudinov, Ravel et al. 1998; Poiarkova

and Rehr 1999), was based on linear Se···H-O, from hydrogen-bonded water molecules near the Se atom.

Results

Figure 2.1 compares the Se XAS data for a sample of the diselenide, CoM-Se-Se-CoM (dashed line) with the reduced sample, nominally CoM-SeH (solid line). Detailed curve-fitting analysis of the CoM-Se-Se-CoM data revealed a best fit assuming a Se-C,Se coordination environment, as expected (Table 2.1, fit 2).

The diselenide was reduced (to CoM-SeH) using DTT and was subsequently purified by anion exchange chromatography to remove unreacted CoM-Se-Se-CoM and DTT. Reduction was expected to result in Se coordination to one carbon atom (and perhaps a hydrogen atom, which cannot be detected by XAS). In the FTs (Fig. 2.1B), the Se-Se peak (~2.3 Å) is reduced significantly in the "CoM-SeH" sample (solid line), but not eliminated. This led us to question whether partial reoxidation to the diselenide had occurred after reduction and purification. To quantify any diselenide remaining (or reformed by partial oxidation) in the "CoM-SeH" sample, we used the Se-Se fitting parameters of the known diselenide EXAFS (Table 2.1, fit 2), and fit the "CoM-SeH" Se EXAFS to determine the amount of diselenide remaining. Assuming the same Debye-Waller factor (σ_{as}^2) for Se-Se found in CoM-Se-Se-CoM fits, we determined that each Se sees approximately 0.4 Se in addition to a C (Table 2.1, fits 6-8), implying that about 25% CoM-Se-Se-CoM remained in this "CoM-SeH" sample.

It can also be seen in Fig. 2.1B that the "CoM-SeH" FT (solid line) exhibits another interaction at ~3.2 Å that we suggest represents the oxygen atoms of hydrogen-bonded water molecules (with reasonable Se···O distances of ~3.2 Å) in this aqueous sample. Two to four H_2O

molecules (with three most likely) could be hydrogen bonded in this way to the CoM-Se^- anion (Table 2.1, fits 6-8).

HDR was reacted either with anaerobically purified "CoM-SeH" (HDR + CoM-SeH) or with the crude reaction mixture of CoM-Se-Se-CoM and DTT (HDR + CoM-Se-Se-CoM + DTT). In both cases, excess reactant was removed by extensive washing (by ultrafiltration) of the protein sample. Aliquots of each sample were analyzed by EPR spectroscopy to confirm the formation of the CoM-SeH-induced EPR signal that has been described previously (Duin, Bauer et al. 2003). Se XAS results for both samples are presented in Figure 2.2 and the data are nearly identical in both edge and EXAFS regions. Both edge data (Fig. 2.2A) and the position of the major FT peak (Fig. 2.2B) suggest a Se environment quite different from that in the CoM-Se-Se-CoM substrate alone. Based on curve-fitting analysis, the best fits for both HDR samples are consistent with a model that contains one Se-C bond at 1.98 Å and one Se-Fe interaction at ~2.4 Å (Table 2.1, fits 10, 13). The Se EXAFS and FTs of these samples are similar to those for CoM-Se-Se-CoM (Fig. 2.2B and inset). In fact, the HDR Se EXAFS data can be fit with shells of Se-C and Se-Se (Table 2.1, fits 11, 14). However, these alternative fits are slightly less satisfactory (higher f') and yield Se-Se distances longer than found in the diselenide (Table 2.1; fits 2, 11, 14). Most convincingly, the Se edge data are drastically different (Fig. 2.2A), suggesting very different Se coordination environments in CoM-SeH-reacted HDR compared to CoM-Se-Se-CoM; The major Se species in the CoM-SeH-reacted HDR sample cannot be the diselenide.

Discussion

To provide a spectroscopic method to study the CoM-HDR reaction intermediate, which is formed when oxidized HDR reacts with CoM-SH in the absence of CoB-SH, we utilized the Se analog of CoM-SH. We performed Se XAS investigations on CoM-SeH and CoM-Se-Se-

CoM, from which CoM-SeH was synthesized, for comparison with the CoM-SeH adduct of HDR, allowing us to determine whether any free CoM-SeH or diselenide existed in the HDR samples. This was a concern since we do observe some diselenide in a DTT-reduced sample (Fig. 2.1; Table 2.1, fits 6-8).

Two experiments with HDR using CoM-SeH generated under different conditions (described in the Experimental Section) resulted in nearly identical XAS data (Fig. 2.2, solid and dotted lines). Se EXAFS and FTs are reminiscent of those of the substrate diselenide (Fig. 2.2B). However, the predominant Se environment in the HDR samples cannot be the substrate diselenide. First, extensive ultrafiltration assures that we are examining a protein-associated site. Second, the Se edge convincingly demonstrates that this Se environment is quite different from that of the diselenide (Fig. 2.2A). Third, attempts to fit the Se EXAFS of HDR samples with a Se-Se interaction results in chemically unreasonable Se-Se bond distances (Table 2.1, fits 11, 14). Apparently, Se-Se and Se-Fe scattering have sufficiently similar phase that they are difficult to distinguish *a priori*. This ambiguity has been pointed out in early studies on Fe_2Se_2 compounds (Weatherill, Rauchfuss et al. 1986).

The best fit of the Se EXAFS data for both HDR samples is a model that contains one Se-C bond (at 1.98 Å) and one Se-Fe interaction at ~2.4 Å (Table 2.1, fits 10, 13). The Cambridge Structural Database (Wavefunction, Inc.) was searched for Fe-Se-C fragments, from which a chemically reasonable average Se-Fe bond distance of 2.42 ± 0.02 Å was found (McConnachie and Ibers 1991; Schumann, Arif et al. 1991; Forde, Morris et al. 1994; Liaw, Ou et al. 1994; Liaw, Horng et al. 1997; Liaw, Chiang et al. 2000; Zheng, Miao et al. 2000), consistent with our determination of 2.41 Å for HDR + CoM-SeH.

These data provide a direct structural framework to interpret the EPR experiments performed by Duin and colleagues on HDR incubated with the substrate CoM-^{33}SH (Duin, Bauer et al. 2003). Particularly, it provides direct structural evidence of an Fe-Se interaction in HDR reacted with CoM-SeH, further validating their proposed mechanism involving the direct attachment of CoM-SH to an iron, thus forming a $[4Fe\text{-}4S]^{3+}$ cluster with a five-coordinate Fe site.

Acknowledgments

The XAS data were collected at the Stanford Synchrotron Radiation Laboratory, a national user facility operated by Stanford University on behalf of the U.S. Department of Energy, Office of Basic Energy Sciences. The SSRL Structural Molecular Biology Program is supported by the Department of Energy, Office of Biological and Environmental Research, and by the National Institutes of Health, National Center for Research Resources, Biomedical Technology Program. These studies were supported in part by the National Institutes of Health (GM42025 to RAS) and by the Max-Planck-Gesellschaft, the Deutsche Forschungsgemeinschaft (SPP 1071), and the Fonds der Chemische Industrie (to RH).

References

Ankudinov, A. L., B. Ravel, et al. (1998). "Real-space multiple-scattering calculation and interpretation of x-ray-absorption near-edge structure." Physical Review B **58**(12): 7565-7576.

Bennati, M., N. Weiden, et al. (2004). "^{57}Fe ENDOR spectroscopy on the iron-sulfur cluster involved in substrate reduction of heterodisulfide reductase." J. Am. Chem. Soc. **126**(27): 8378-8379.

Duin, E. C., C. Bauer, et al. (2003). "Coenzyme M binds to a [4Fe-4S] cluster in the active site of heterodisulfide reductase as deduced from EPR studies with the [S-33]coenzyme M-treated enzyme." Febs Letters **538**(1-3): 81-84.

Duin, E. C., S. Madadi-Kahkesh, et al. (2002). "Heterodisulfide reductase from Methanothermobacter marburgensis contains an active-site [4Fe-4S] cluster that is directly involved in mediating heterodisulfide reduction." Febs Letters **512**(1-3): 263-268.

Forde, C. E., R. H. Morris, et al. (1994). "Neutral 4-Coordinate (Selenolato)Iron(II) Complexes - Syntheses and Structures of $Fe(Se\text{-}2,6\text{-}i\text{-}Pr_2C_6H_3)_2(PMe_2Ph)_2$ and $Fe(Se\text{-}2,6\text{-}i\text{-}Pr_2C_6H_3)_2(Et_2PCH_2CH_2PEt_2)$." Inorg. Chem. **33**(25): 5647-5653.

Liaw, W. F., C. Y. Chiang, et al. (2000). "Heterobimetallics of nickel-iron dinitrosyl: Electronic control by chelate and diatomic ligands." Inorg. Chem. **39**(3): 480-484.

Liaw, W. F., Y. C. Horng, et al. (1997). "Distorted square planar Ni(II)-chalcogenolate carbonyl complexes $[Ni(CO)(SPh)_n(SePh)_{3-n}]^-$ (n=0, 1, 2): Relevance to the nickel site in CO dehydrogenases and [NiFeSe] hydrogenase." J. Am. Chem. Soc. **119**(39): 9299-9300.

Liaw, W. F., D. S. Ou, et al. (1994). "Bis(Selenolate) and Bis(Thiolate) Derivatives of Iron(II) Phosphine Complexes - Crystal-Structure of Cis,Cis,Trans-$Fe(CO)_2(SeMe)_2(PMe_3)_2$." Inorg. Chem. **33**(11): 2495-2496.

Madadi-Kahkesh, S., E. C. Duin, et al. (2001). "A paramagnetic species with unique EPR characteristics in the active site of heterodisulfide reductase from methanogenic archaea." Eur J Biochem **268**(9): 2566-77.

McConnachie, J. M. and J. A. Ibers (1991). "Synthesis of the PPh_4^+ and NEt_4^+ Salts of $M(SePh)_4^{2-}$ (M = Mn, Fe, Co, Ni) and the Structure of $[NEt_4]_2[Fe(SePh)_4]$.Mecn." Inorg. Chem. **30**(8): 1770-1773.

Poiarkova, A. V. and J. J. Rehr (1999). "Multiple-scattering x-ray-absorption fine-structure Debye-Waller factor calculations." Physical Review B **59**(2): 948-957.

Schumann, H., A. M. Arif, et al. (1991). "Structure and Bonding in Cationic Cyclopentadienyliron Complexes Containing Thioethers, Selenoethers, and Telluroethers as Ligands." Inorg. Chem. **30**(7): 1618-1625.

Scott, R. A. (2000). X-Ray Absorption Spectroscopy. Physical Methods in Bioinorganic Chemistry. Spectroscopy and Magnetism. L. Que. Sausalito, CA, University Science Books**:** 465-503.

Thauer, R. K. (1998). "Biochemistry of methanogenesis: a tribute to Marjory Stephenson. 1998 Marjory Stephenson Prize Lecture." Microbiology **144 (Pt 9)**: 2377-406.

Weatherill, T. D., T. B. Rauchfuss, et al. (1986). "Structural Evidence Concerning the Frontier Orbitals in $[Fe_2S_2(CO)_6]^{2-}$, $[Fe_2Se_2(CO)_6]^{2-}$ - Redox-Active Dichalcogen Ligands." Inorg. Chem. **25**(9): 1466-1472.

Zheng, H. B., S. B. Miao, et al. (2000). "Chemical reactivity of [(μ-RSe)(μ-S){Fe-2(CO)$_6$}$_2$(μ$_4$-S)]$^-$: synthesis and characterization of (μ-RSe)(μ-R'S) {Fe-2(CO)$_6$}$_2$(μ$_4$-S) and (μ$_3$-S)$_2$Fe-3(CO)$_8$[Se(Ph)Fe(CO)$_2$Cp]." Polyhedron **19**(6): 713-718.

Figure Legends

Figure 2.1. Se K edge spectra (A), and Fourier transforms (B) (k = 2-13 $Å^{-1}$) for CoM-Se-Se-CoM (dashed) and CoM-SeH (solid). k^3-weighted EXAFS data are presented as inset to B.

Figure 2.2. Se K edge spectra (A) and Fourier transforms (B) (k = 2-13 $Å^{-1}$) for HDR + CoM-SeH (solid), HDR + CoM-Se-Se-CoM + DTT (dotted), and the diselenide substrate, CoM-Se-Se-CoM (dashed; same data as in Fig. 1). k^3-weighted EXAFS data are presented as inset to B.

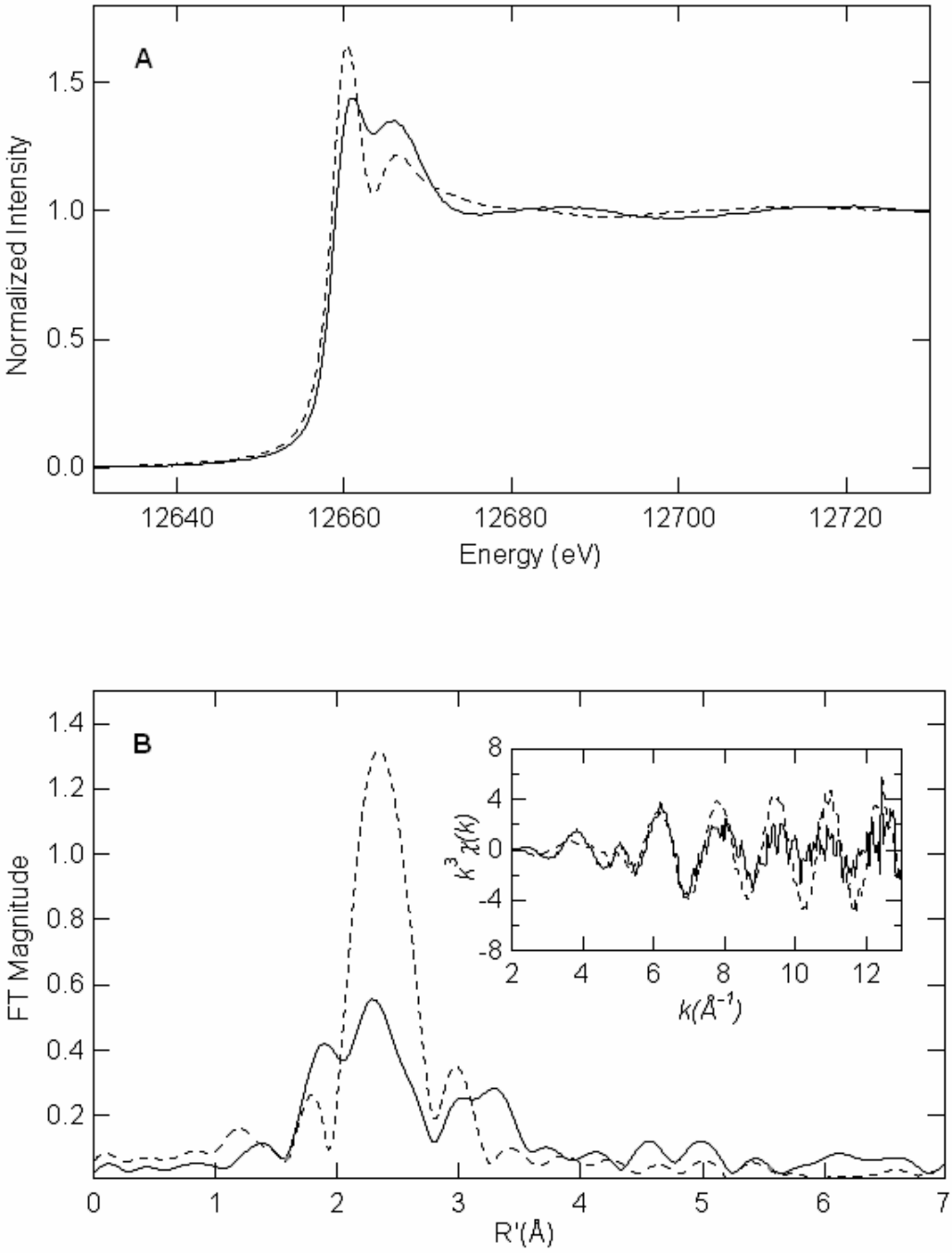
A
Normalized Intensity
1.5
1.0
0.5
0.0
12640
12660
12680
12700
12720
Energy (eV)
B
FT Magnitude
1.4
1.2
1.0
0.8
0.6
0.4
0.2
0
1
2
3
4
5
6
7
R'(Å)
$k^3\chi(k)$
8
4
0
-4
-8
2
4
6
8
10
12
$k(Å^{-1})$

Figure 2.1

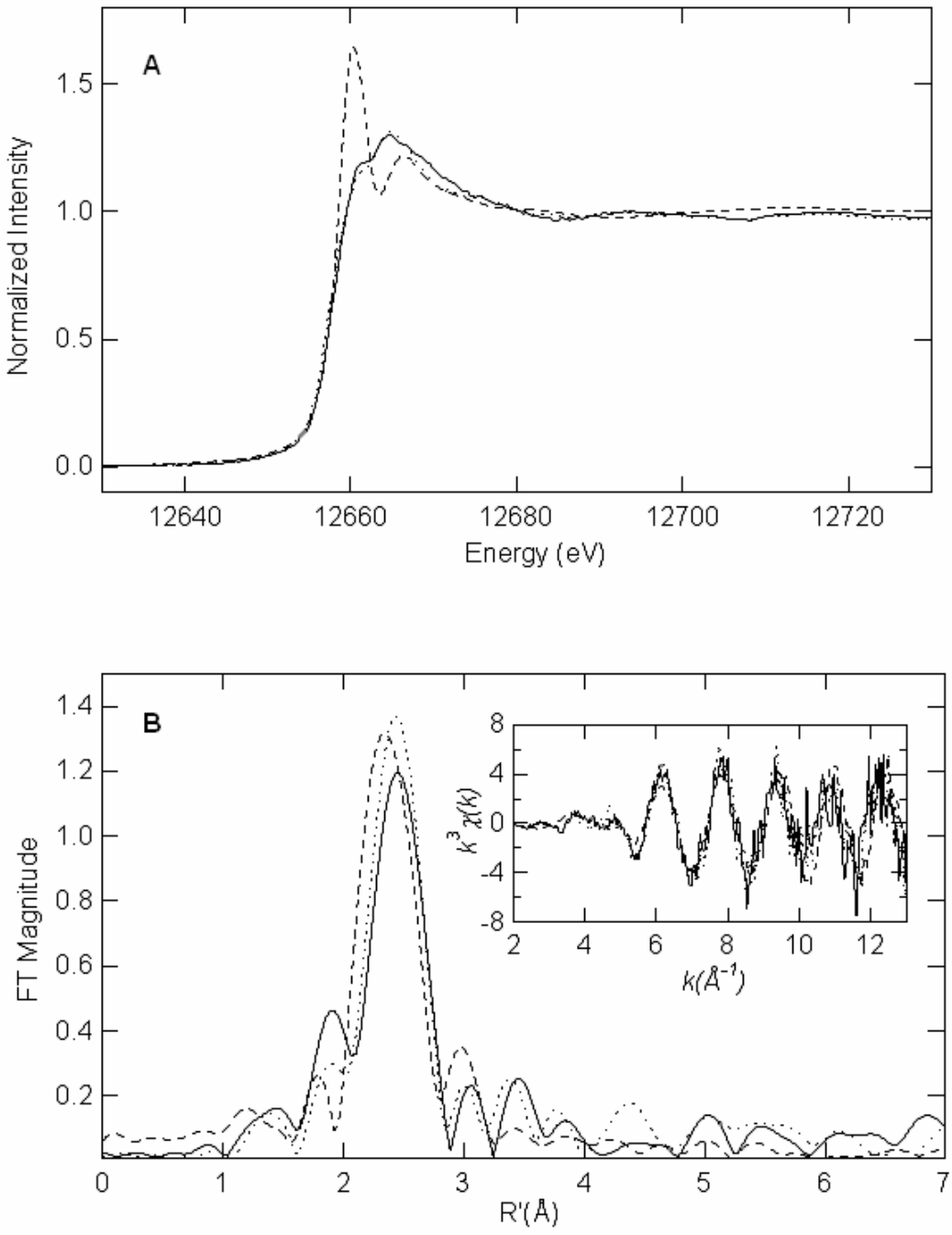
A
Normalized Intensity
1.5
1.0
0.5
0.0
12640
12660
12680
12700
12720
Energy (eV)
B
FT Magnitude
1.4
1.2
1.0
0.8
0.6
0.4
0.2
0
1
2
3
4
5
6
7
R'(Å)
8
4
0
-4
-8
2
4
6
8
10
12
k(Å⁻¹)

Figure 2.2

Table 2.1. Curve fitting results for Se EXAFS[a]

Sample filename (*k* range) $\Delta k^3\chi$	Fit	Shell	R_{as} (Å)	σ_{as}^2 (Å2)	ΔE_0 (eV)	f[b]
CoM-Se-Se-CoM	1	$Se\text{-}Se_1$	2.31	0.0027	–1.68	0.060
ECM2A (2-13 $Å^{-1}$)	2	$Se\text{-}C_1$	1.97	0.0013	–2.89	0.042
$\Delta k^3\chi = 10.56$		$Se\text{-}Se_1$	2.31	0.0023		
	3	$Se\text{-}C_1$	1.99	0.0041	–7.74	0.056
		$Se\text{-}Fe_1$	2.37	0.0012		
CoM-SeH	4	$Se\text{-}C_1$	2.99	0.0037	3.28	0.134
ECOMC (2-13 $Å^{-1}$)	5	$Se\text{-}C_1$	1.91	–0.0002[c]	–10.16	0.098
$\Delta k^3\chi = 9.43$		$Se\text{-}Se_1$	2.29	0.0069		
	6	$Se\text{-}C_1$	1.92	–0.0009	–7.42	0.082
		$Se\text{-}Se_{0.42}$	2.28	[0.0023][d]		
		$Se\text{-}H_2$	1.88	0.0034		
		$Se\text{-}O_2$	[3.25]	0.0059		
	7	$Se\text{-}C_1$	1.92	–0.0009	–6.98	0.081
		$Se\text{-}Se_{0.41}$	2.29	[0.0023]		
		$Se\text{-}H_3$	1.88	0.0054		
		$Se\text{-}O_3$	[3.25]	0.0094		

	8	Se-C_1	1.92	–0.0008	–7.54	0.081
		Se-$Se_{0.41}$	2.28	[0.0023]		
		Se-H_4	1.88	0.0074		
		Se-O_4	[3.24]	0.0128		
HDR+CoM-Se-Se-CoM+DTT	9	Se-C_1	1.99	0.0050	0.63	0.189
EHR0C (2-13 Å^{-1})	10	Se-C_1	1.98	0.0005	1.06	0.085
$\Delta k^3\chi$ = 12.24		Se-Fe_1	2.40	0.0011		
	11	Se-C_1	1.98	–0.0010	5.93	0.096
		Se-Se_1	2.34	0.0024		
HDR+CoM-SeH	12	Se-C_1	1.91	–0.0001	–9.54	0.167
EHRQC (2-13 Å^{-1})	13	Se-C_1	1.97	–0.0003	0.73	0.091
$\Delta k^3\chi$ = 13.06		Se-Fe_1	2.41	0.0016		
	14	Se-C_1	1.97	–0.0011	2.11	0.095
		Se-Se_1	2.35	0.0034		

[a] Shell is the chemical unit defined for the multiple scattering calculation. Subscripts denote the number of scatterers per metal. R_{as} is the metal-scatterer distance. σ_{as}^2 is a mean square deviation in R_{as}. ΔE_0 is the shift in E_0 for the theoretical scattering functions.

[b] f' is a normalized error (chi-squared):

$$f' = \frac{\left\{ \sum_i \left[k^3 \left(\chi_i^{obs} - \chi_i^{calc} \right) \right]^2 / N \right\}^{1/2}}{\left[\left(k^3 \chi^{obs} \right)_{max} - \left(k^3 \chi^{obs} \right)_{min} \right]}$$

[c] Negative values for σ_{as}^2 are not physically possible. We find that the amplitude of weak scattering from C atoms in the presence of other dominant scattering interactions (Se-Se in this case) can be overestimated (by decreasing σ_{as}^2 slightly below zero) in these fits.

[d] Values in square brackets were fixed during optimization.

CHAPTER 3

STRUCTURAL DETERMINATION OF THE COFACTORS IN PURINE HYDROXYLASE

Introduction

Selenium-dependent molybdenum hydroxylases are a unique class of molybdoenzymes that utilize selenium in the form of a labile cofactor to help catalyze hydroxylation reactions involving heterocyclic or aliphatic substrates (Hille, Retey et al. 1998). This class of molybdenum hydroxylases possess two [2Fe-2S] clusters, flavin adenine dinucleotide (FAD), one molybdopterin group, and one Mo. Typically, the Mo site is bound by a single Mo=O ligand, a "cyanolyzable" sulfur (Mo=S) ligand, one hydroxyl ligand, and two sulfur ligands derived from the ditholene of the molybdopterin cofactor. The hydroxylase family includes enzymes such as xanthine dehydrogenase and nicotinic acid hydroxylase from *Clostridium purinolyticum* (Self and Stadtman 2000) and *Clostridium barkeri* (Dilworth 1982), respectively.

In the fermentative interconversion of purines to uric acid, purine hydroxylase (PH) from *Clostridium purinolyticum* catalyzes the hydroxylation of the 6-postion on the purine ring of hypoxanthine to produce xanthine (Self and Stadtman 2000). Spectroscopic characterization of PH revealed the presence of a molybdenum cofactor, and subsequent experiments with cyanide confirmed the presence of a dissociable Se moiety, removed by cyanide, and dependence on Se for PH enzymatic activity (Self and Stadtman 2000). Recently, variable temperature electron paramagnetic resonance (EPR) analysis of the hypoxanthine (HX)-treated form of PH revealed the presence of a Mo(V) center and two different Fe-S clusters, [2Fe-2S]I and [2Fe-2S]II (Self,

Wolfe et al. 2003), observed in a variety of Mo-containing enzymes such as aldehyde oxidoreductase from *Desulfovibrio gigas* (Rebelo, Dias et al. 2001; Self, Wolfe et al. 2003). EPR experiments utilizing ^{77}Se-enriched PH revealed no detectable interaction between the Mo and Se atoms, suggesting Se is not bound to the Mo center. Furthermore, cyanide-treated PH and as isolated PH produce almost identical EPR spectra strengthening the hypothesis that selenium is not a direct ligand of the Mo atom (Self, Wolfe et al. 2003). The Mo active site was predicted to be bound by two sulfurs, two short oxygen (Mo=O) ligands, and a water molecule. Herein we utilize Mo and Fe X-ray absorption spectroscopic (XAS) experiments to generate direct structural information on the metal sites and provide further insight into the mechanistic aspects of the enzyme.

Methods

Purification of Purine Hydroxylase (sample preparation performed by Stadtman and Self laboratories). Purification of PH was carried out as previously described (Self, Wolfe et al. 2003). PH samples for XAS analysis were concentrated to approximately 75 mg/mL using Amicon microspin concentrators (30,000 MW cutoff, Millipore, Billerica, MA), and subsequently dialyzed overnight in buffer containing 50% glycerol, 100 mM Tricine, pH 8.0. Subsequent concentration using Amicon microspon concentrators was necessary to obtain PH samples at 1 mM concentration (approximately 150 mg/mL). Samples treated with KCN (15 mM final concentration) were incubated at room temperature under anaerobic conditions (95% nitrogen, 5 % hydrogen) in a Coy anaerobic chamber (Coy Labs, Grass Lake, Michigan) for up to 6 h. PH activity was assayed at time intervals to confirm a KCN-dependent decrease in activity as previously reported (Self and Stadtman 2000; Self, Wolfe et al. 2003). Treatment of PH with hypoxanthine (HX) was also performed under anaerobic conditions, since oxygen can

act as an electron acceptor for PH with HX as a substrate (data not shown). HX-treated PH was allowed to incubate for 5 min at room temperature before loading into XAS cuvets. All concentrated samples (treated and untreated) were loaded into 24 × 3 × 2 mm polycarbonate cuvets (with one 24 × 3 mm wall consisting of 25-μm X-ray transparent Mylar tape) under anaerobic conditions and immediately frozen in liquid nitrogen.

X-ray absorption spectroscopy. X-ray absorption spectra were collected at the Stanford Synchrotron Radiation Laboratory (SSRL) on beam lines 7-3 and 9-3 with the SPEAR2 ring operating at 3.0 GeV, 60-100 mA. Fluorescence excitation spectra were recorded with the sample at 10 K using a 1-mm vertically apertured beam incident on a Si[220] double-crystal monochromator. The averaged XAS data represent 10 scans, each of 21 min duration. EXAFSPAK software (www-ssrl.slac.stanford.edu/exafspak.html) was used for data reduction and analysis, according to standard procedures (Scott 2000). Energy calibration was achieved using the first inflection of the edge of an internal metal foil standard for each metal under investigation (Mo = 20000.3 eV and Fe = 7111.2 eV). The Fourier transforms (FTs) of the extended X-ray absorption fine structure (EXAFS) data were generated using sulfur-based phase correction for both Fe and Mo. XAS experiments were repeated on identically prepared samples at different times to ensure reproducibility.

Results

XAS experiments were performed on three different PH samples (preparation described in Methods): as isolated, hypoxanthine-treated PH (PH + HX), and cyanide-treated PH (PH + CN^-). Comparison of the Mo K edge spectra (Figure 3.1A) reveals an edge shift of ~1.3 eV to lower energy position upon addition of hypoxanthine, suggesting partial reduction of the Mo center (Figure 3.1A). The data also display a shoulder at ~20010 eV (Figure 3.1A inset), that

originates from a dipole-allowed transition along the Mo=O bond and is sensitive to the number of Mo=O ligands present (Kutzler, Scott et al. 1981). Compared to the as isolated sample, the PH + CN^- sample shows a more defined shoulder in this region, implying an increase in the number of Mo=O ligands present and/or a change in coordination geometry.

Figure 3.1B reveals only minor changes in the Mo EXAFS of as isolated PH and PH + HX, suggesting small changes in the Mo coordination sphere upon HX addition. The Mo coordination spheres of as isolated PH and PH + HX both consist of two short (double-bonded) oxygens at ca 1.7 Å and two sulfur-containing ligands (at ca 2.45 Å), the latter presumably arising from the molybdopterin ligand (Table 3.1). Fits with an additional (N,O)-containing ligand at a single-bond distance (ca 1.95 Å) show slight improvements in goodness of fit (f') and reasonable Debye-Waller factors, suggesting a five-coordinate environment containing a solvent ligand. The FTs also suggest a more ordered (symmetric) set of Mo-S bond distances for PH + HX, compared to PH, reflected in the higher intensity of the FT peak at ~2.4 Å.

As suggested by the Mo K edges (Figure 3.1A), the FTs for PH + CN^- show an increase in the peak intensity at ~1.7 Å, indicating a more ordered set of oxygen ligands. Thus, when PH + CN^- Mo EXAFS is fit to a coordination shell similar to the one described above (MoO_2S_2O; Table 3.1, Fit 9), a small Debye-Waller factor is produced for the short oxygen ligands while an unreasonably high Debye-Waller factor is produced for the long oxygen (OH/OH_2) ligand. Thus, the curve-fitting analysis for PH + CN^- is more consistent with a model that contains three short oxygen ligands at 1.69 Å and two sulfur ligands at 2.45 Å (Table 3.1, Fit 10).

Fe XAS of all three samples suggests that the major Fe component consists of typical Fe_2S_2 clusters, with each Fe coordinated tetrahedrally by four sulfurs (at ca 2.26 Å) and detecting one other Fe at about 2.72-2.77 Å (Table 3.2). Figure 3.2A compares the Fe K edges for all three

samples. The Fe K edge of PH + HX is shifted to lower energy than that for as isolated PH and PH + CN^-, consistent with reduction of the Fe_2S_2 clusters upon addition of substrate. The as isolated and PH + CN^- samples display nearly identical Fe K-edge plots implying highly similar coordination environments. However, the amplitude of the FT peak at ~2.7 Å is significantly reduced in the cyanide-treated sample (Figure 3.2B) suggesting some breakdown of the Fe_2S_2 clusters. To quantify the amount of Fe scatterer detected by each Fe absorber compared to the as isolated enzyme, we used the Fe···Fe Debye-Waller factor of as isolated PH and fit the PH + CN^- Fe EXAFS allowing the Fe···Fe number to vary. Slightly over half the Fe detects another Fe at about 2.77 Å (Table 3.2, Fit 6), suggesting that some cyanide-induced degradation of Fe_2S_2 clusters may occur. In addition, the PH + CN^- sample displays a FT peak at ~4.9 Å that likely results from the formation of species containing the Fe-C≡N-Fe moiety that would give rise to an Fe···Fe interaction at this distance.

Discussion

Including one longer Mo-O interaction improves the quality of the Mo EXAFS fits, at least for PH and PH + HX samples (Table 3.1). This "solvent" ligand can be identified as either a hydroxide or a water molecule, although the bond distance (ca 1.95 Å) suggests the former. Additionally, fits involving Mo bound to three sulfurs atoms (Table 3.1) are less satisfactory (higher f') and produce unreasonably large Debye-Waller factors for all samples. Thus, the PH active site appears to display a MoO_2S_2O coordination environment (Figure 3.3a), a structure that belongs to the molybdenum hydroxylase family, although it appears to exist in the desulfo form (the "cyanolyzable" sulfur is replaced by an oxo ligand). Addition of substrate HX results in a shift to lower energy of both the Mo (Figure 3.1A) and Fe (Figure 3.2A) edges, suggesting

reduction at both sites. By contrast, very little difference in the Mo EXAFS is observed beyond a slight ordering of Mo-S distances (Figure 3.3b).

To help determine whether selenium was bound to molybdenum, cyanide was added to the as isolated PH to inactivate the enzyme and release selenium from it. Cyanide treatment results in a significant change to both Mo and Fe XAS spectra. The changes to the Fe EXAFS are likely the result of cyanide-induced degradation of some of the Fe_2S_2 clusters. The changes to the Mo EXAFS are best explained by an increase in the number of short Mo=O interactions, at the expense of a longer Mo-O distance (Figure 3.3c). Addition of a Se atom to the Mo coordination environment in the fitting procedure resulted in unreasonable parameters for all samples (fit not shown). This confirms earlier EPR experiments that were interpreted in terms of Se having no interaction with Mo. Se XAS experiments are currently underway to determine whether Se detects a Mo in its coordination environment and to determine the nature of the dissociable Se cofactor.

Acknowledgments

The XAS data were collected at the Stanford Synchrotron Radiation Laboratory, a national user facility operated by Stanford University on behalf of the U.S. Department of Energy, Office of Basic Energy Sciences. The SSRL Structural Molecular Biology Program is supported by the Department of Energy, Office of Biological and Environmental Research, and by the National Institutes of Health, National Center for Research Resources, Biomedical Technology Program. These studies were supported in part by the National Institutes of Health (GM42025 to RAS) and the intramural program at the National Heart, Lung and Blood Institute, NIH, Bethesda, Maryland. The authors would also like to thank Dr. Matt Wolf (NHLBI, NIH) for helpful discussions that contributed to the analysis of the data.

References

Dilworth, G. L. (1982). "Properties of the selenium-containing moiety of nicotinic acid hydroxylase from Clostridium barkeri." Arch Biochem Biophys **219**(1): 30-8.

Hille, R., J. Retey, et al. (1998). "Mechanistic aspects of molybdenum-containing enzymes." FEMS Microbiol Rev **22**(5): 489-501.

Kutzler, F. W., R. A. Scott, et al. (1981). "Single-Crystal Polarized X-Ray Absorption-Spectroscopy - Observation and Theory for (Moo2s2)2-." Journal of the American Chemical Society **103**(20): 6083-6088.

Rebelo, J. M., J. M. Dias, et al. (2001). "Structure refinement of the aldehyde oxidoreductase from Desulfovibrio gigas (MOP) at 1.28 A." J Biol Inorg Chem **6**(8): 791-800.

Scott, R. A. (2000). X-Ray Absorption Spectroscopy. Physical Methods in Bioinorganic Chemistry. Spectroscopy and Magnetism. L. Que. Sausalito, CA, University Science Books**:** 465-503.

Self, W. T. and T. C. Stadtman (2000). "Selenium-dependent metabolism of purines: A selenium-dependent purine hydroxylase and xanthine dehydrogenase were purified from Clostridium purinolyticum and characterized." Proc Natl Acad Sci U S A **97**(13): 7208-13.

Self, W. T., M. D. Wolfe, et al. (2003). "Cofactor determination and spectroscopic characterization of the selenium-dependent purine hydroxylase from Clostridium purinolyticum." Biochemistry **42**(38): 11382-90.

Table 3.1. Curve fitting results for Mo EXAFS[a]

Sample filename (*k* range) $\Delta k^3\chi$	Fit	Shell	R_{as} (Å)	σ_{as}^2 ($Å^2$)	ΔE_0 (eV)	f[b]
Purine Hydroxylase, wt	1	Mo-O_2	1.69	0.0031	–2.75	0.106
MPH0C (2-13 $Å^{-1}$)		Mo-S_2	2.44	0.0058		
$\Delta k^3\chi$ = 11.46	2	Mo-O_2	1.69	0.0033	–1.31	0.110
		Mo-S_3	2.44	0.0086		
	3	Mo-O_2	1.70	0.0031	–0.24	0.094
		Mo-S_2	2.45	0.0059		
		Mo-O	1.95	0.0033		
PH + hypoxanthine	4	Mo-O_2	1.69	0.0031	–2.89	0.086
MPHHC (2-13 $Å^{-1}$)		Mo-S_2	2.41	0.0043		
$\Delta k^3\chi$ = 12.22	5	Mo-O_2	1.70	0.0030	–1.18	0.089
		Mo-S_3	2.41	0.0072		
	6	Mo-O_2	1.69	0.0030	–2.62	0.081
		Mo-S_2	2.41	0.0044		
		Mo-O	1.97	0.0063		
PH + CN^-	7	Mo-O_2	1.70	0.0022	–3.15	0.074
MPHCA (2-13 $Å^{-1}$)		Mo-S_2	2.46	0.0058		

$\Delta k^3\chi = 11.28$	8	Mo-O_2	1.70	0.0022	–3.15	0.080
		Mo-S_3	2.46	0.0089		
	9	Mo-O_2	1.70	0.0017	–1.68	0.071
		Mo-S_2	2.47	0.0059		
		Mo-O	1.93	0.0084		
	10	Mo-O_3	1.69	0.0048	–6.15	0.086
		Mo-S_2	2.45	0.0061		

[a] Shell is the chemical unit defined for the multiple scattering calculation. Subscripts denote the number of scatterers per metal. R_{as} is the metal-scatterer distance. σ_{as}^2 is a mean square deviation in R_{as}. ΔE_0 is the shift in E_0 for the theoretical scattering functions.

[b] f' is a normalized error (chi-squared):

$$f' = \frac{\left\{ \sum_i \left[k^3 \left(\chi_i^{obs} - \chi_i^{calc} \right) \right]^2 / N \right\}^{1/2}}{\left[\left(k^3 \chi^{obs} \right)_{max} - \left(k^3 \chi^{obs} \right)_{min} \right]}$$

Table 3.2. Curve fitting results for Fe EXAFS[a]

Sample filename (*k* range) $\Delta k^3\chi$	Fit	Shell	R_{as} (Å)	σ_{as}^2 (Å2)	ΔE_0 (eV)	f[b]
Purine Hydroxylase, wt	1	Fe-S_4	2.25	0.0049	–2.26	0.119
FPH0A (2-13 Å^{-1})	2	Fe-S_4	2.25	0.0049	–1.61	0.112
$\Delta k^3\chi$ = 15.85		Fe-Fe	2.72	0.0056		
PH + hypoxanthine	3	Fe-S_4	2.26	0.0045	–1.84	0.093
FPHHA (2-13 Å^{-1})	4	Fe-S_4	2.26	0.0045	–1.20	0.079
$\Delta k^3\chi$ = 18.20		Fe-Fe	2.73	0.0042		
PH + CN^-	5	Fe-S_4	2.26	0.0055	–0.16	0.094
FPHCA (2-13 Å^{-1})	6	Fe-S_4	2.26	0.0054	–0.18	0.089
$\Delta k^3\chi$ = 15.98		Fe-$Fe_{0.56}$	2.77	[0.0056]		

[a] Shell is the chemical unit defined for the multiple scattering calculation. Subscripts denote the number of scatterers per metal. R_{as} is the metal-scatterer distance. σ_{as}^2 is a mean square deviation in R_{as}. ΔE_0 is the shift in E_0 for the theoretical scattering functions.

[b] f' is a normalized error (chi-squared):

$$f' = \frac{\left\{ \sum_i \left[k^3 \left(\chi_i^{obs} - \chi_i^{calc} \right) \right]^2 / N \right\}^{1/2}}{\left[\left(k^3 \chi^{obs} \right)_{max} - \left(k^3 \chi^{obs} \right)_{min} \right]}$$

Figure Legends

Figure 3.1. (A) Mo K edge spectra; and (B) Fourier transforms (k^3 weighting; k = 2-13 Å^{-1}) for PH (solid), PH + HX (dotted), and PH + CN^- (dashed). Expanded view of the edge transition and k^3-weighted EXAFS data are presented as insets to A and B, respectively.

Figure 3.2. (A) Fe K edge spectra; and (B) Fourier transforms (k^3 weighting; k = 2-13 Å^{-1}) for PH (solid), PH + HX (dotted), and PH + CN^- (dashed). k^3-weighted EXAFS data are presented as inset to B.

Figure 3.3. Proposed structures of the PH active site: (a) as isolated, (b) PH + HX and (c) PH + CN^-.

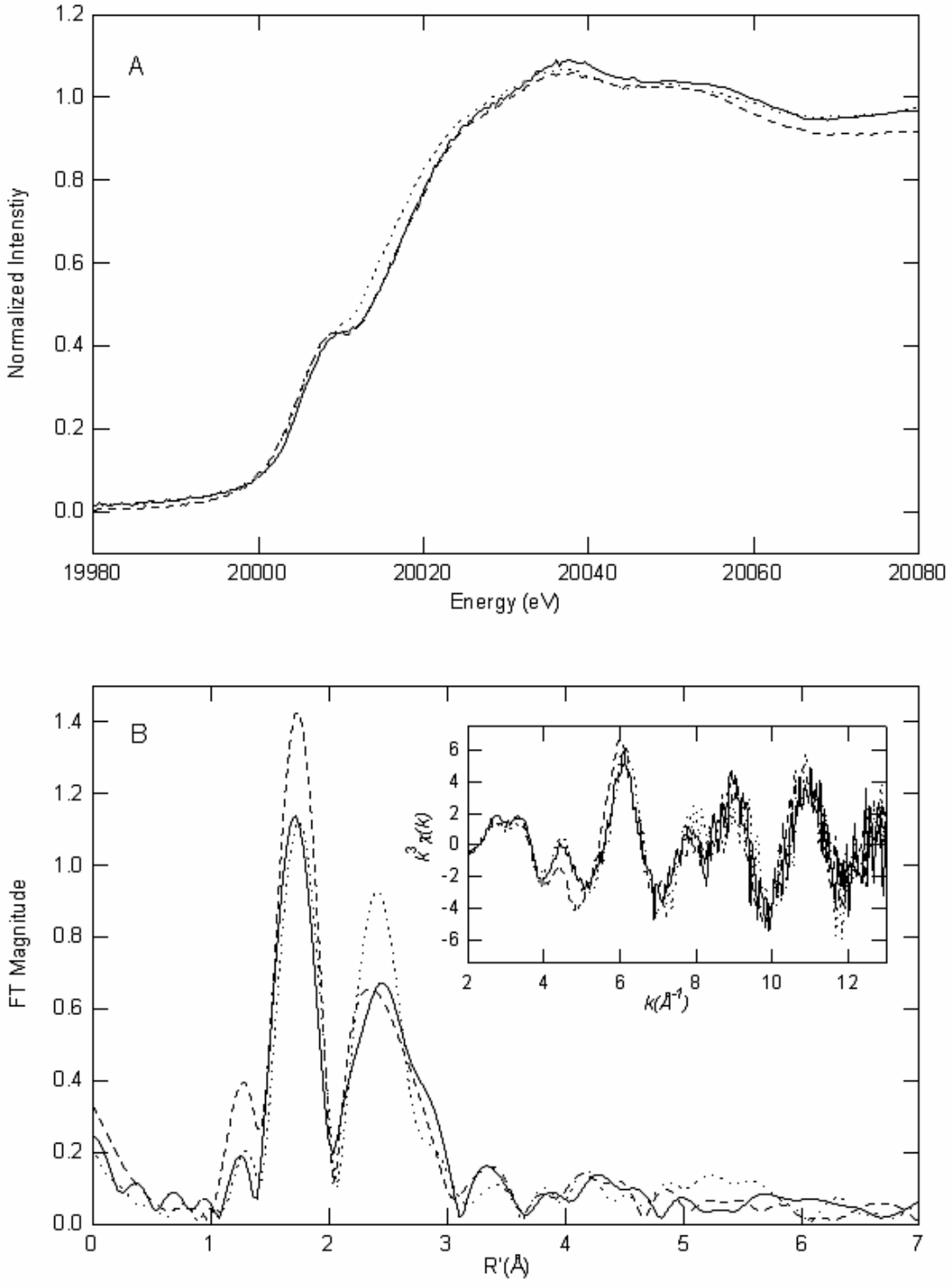
A
Normalized Intenstiy
Energy (eV)
B
FT Magnitude
R'(Å)
$k^3\chi(k)$
$k(Å^{-1})$

Figure 3.1

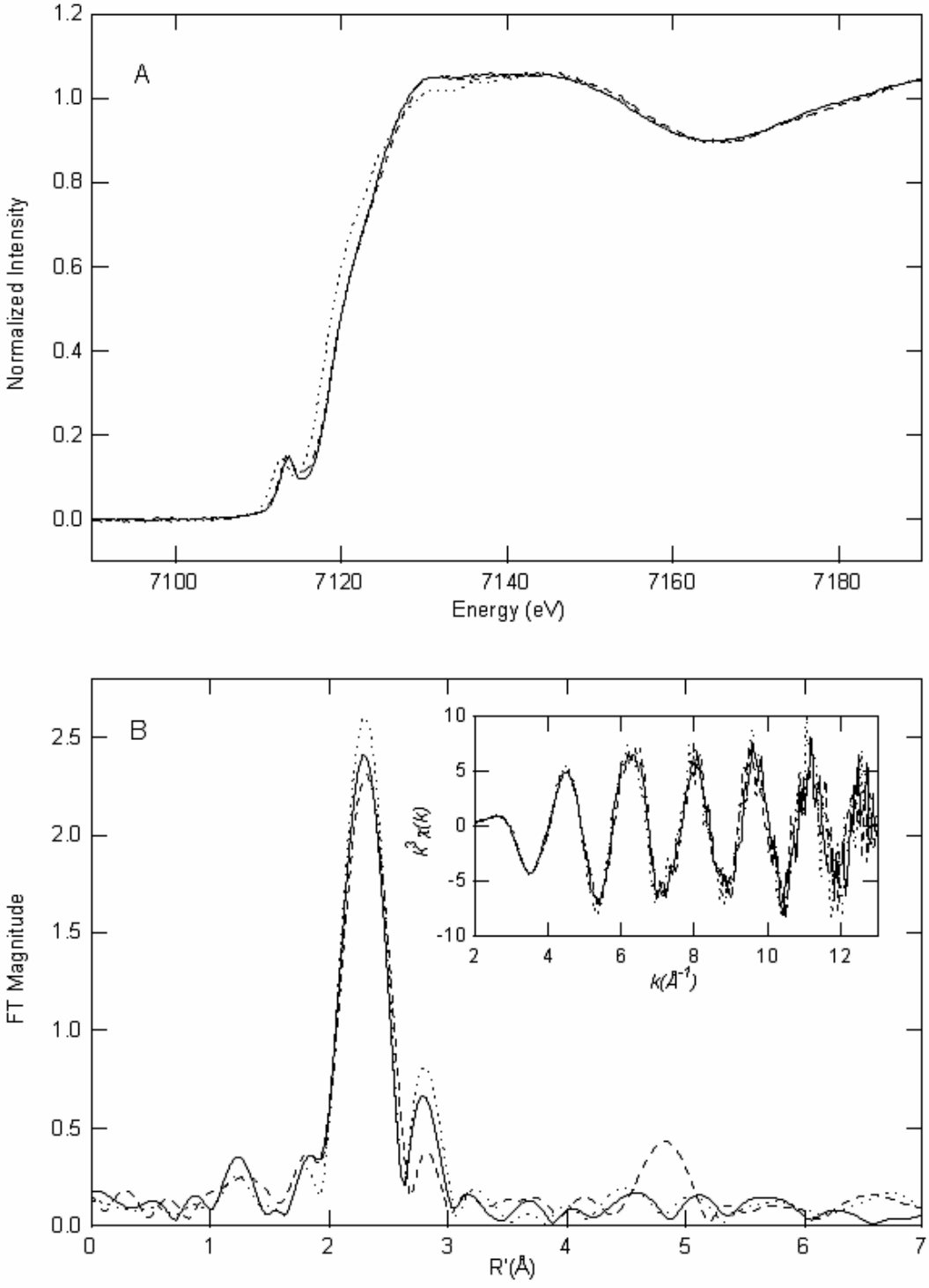
A
Normalized Intensity
Energy (eV)
B
FT Magnitude
R'(Å)
$k^3\chi(k)$
$k(Å^{-1})$

Figure 3.2

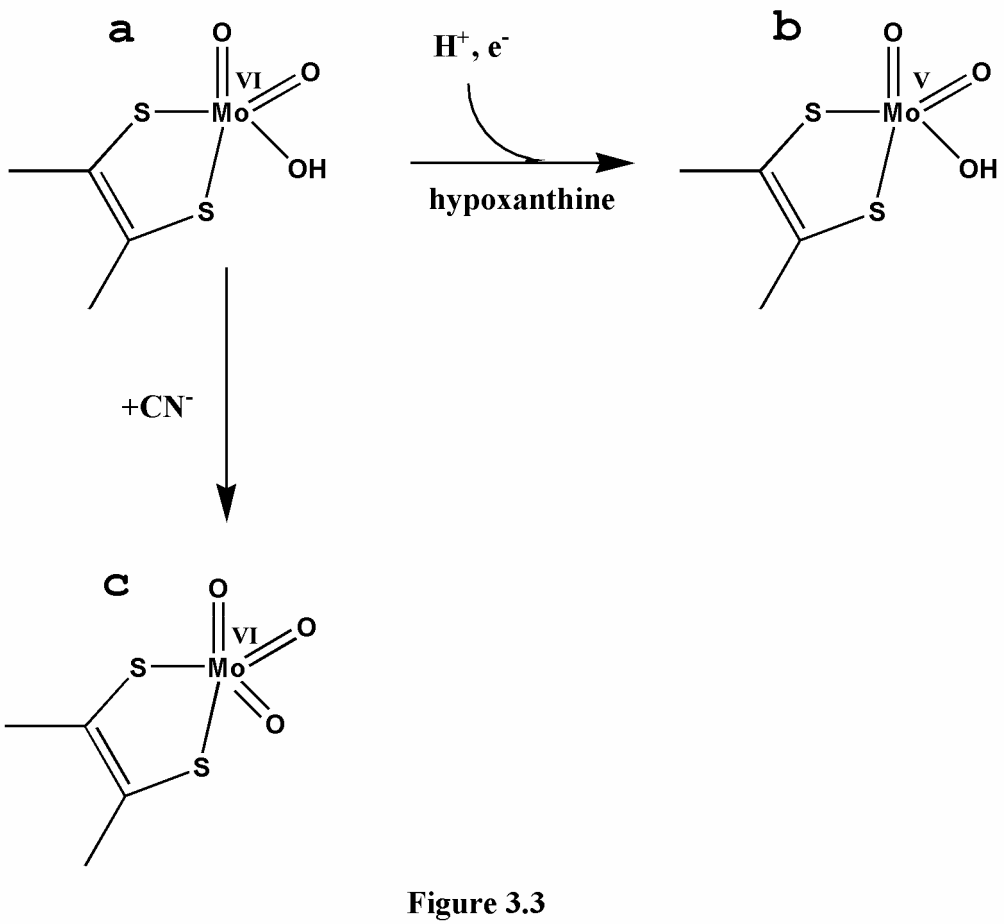

Figure 3.3

CHAPTER 4

METALS IN AMYLOID (FIBRIL) FORMATION

Introduction

Amyloid (fibril) formation, a self-assembly process, is associated with a number of human diseases, most notably Alzheimer's disease (AD) (Brown, Tummolo et al. 1997; Suh, Jensen et al. 2000; Morgan, Lakdawala et al. 2002). Understanding the details of fibril formation is not only relevant to the treatment of amyloid diseases, but could also open the possibility of using self-assembly in the design of new materials with specific properties. The amyloid-β (Aβ) peptide, which is a major component of neuronal plaques found in the brains of AD patients, is formed by proteolytic cleavage of the β-amyloid precursor protein (βAPP; Figure 1) (Selkoe 1994; Selkoe 1994). These neuronal plaques are the central result of aggregate formation caused by the "mis-folding" of the Aβ peptides. Even though the role of amyloid plaques in AD is not currently understood, they do appear as a common fingerprint in its pathogenesis. Interestingly, the presence of high amounts of Zn^{2+} and Cu^{2+} have been found in amyloid plaques of AD patients (Bush, Pettingell et al. 1994; Atwood, Moir et al. 1998), suggesting these metal ions could play an important role in amyloid aggregation, neurotoxicity and neurological disease.

In general, Aβ is a 39 to 43 amino acid peptide (Figure 4.1) with low solubility and a molecular weight indicative of aggregation (Masters, Simms et al. 1985). These properties have contributed to the limited amount of detailed structural data for amyloid fibrils. In addition, it has been hypothesized that metal-histidine binding plays a crucial role in Aβ aggregation and probably also in neurotoxicity; however, direct structural information regarding the metal-Aβ

interaction, particularly at the histidine site, is lacking. This problem has launched a large scale *in vitro* characterization of synthetic peptides to further understand the steps of peptide aggregation and the role of specific metals (i.e. Zn^{2+} and Cu^{2+}) in aggregation. For example, the truncated peptides, Aβ(10-21) and Aβ(13-21)K16A, have been prepared by Dr. David Lynn's group at Emory University in hopes of understanding how Zn^{2+}-, Cu^{2+}-histidine binding modulate the structure and kinetics of amyloid formation. Recently, experiments probing the Zn^{2+} and Cu^{2+} binding effects on fibril formation of Aβ peptides led to the discovery that Zn^{2+} has an ability to accelerate fibril formation, and that under particular conditions (pH dependent), Cu^{2+} can actually inhibit self-assembly (Suzuki, Miura et al. 2001). Structural characterization of metal-Aβ(13-21)K16A complexes by combined techniques (UV, Circular Dichroism, NMR and EPR) have also indicated different coordination geometries for Cu^{2+} and Zn^{2+} active sites (Lynn and Meredith 2000; Lakdawala, Morgan et al. 2002). Moreover, they found that the final morphology of the overall structure can be modulated by Zn^{2+}.

A proposed structure of the fibril formed from Aβ(10-35) and variants is seen in Figure 4.2 (Burkoth, Benzinger et al. 2000; Morgan, Dong et al. 2002). The peptide forms a single extended beta strand, showing as a single green line Figure 4.2a. The fibrils consist of β-strands aggregated into parallel in register β-sheets, with a spacing of 5 Å between strands within a sheet (Figure 4.2b). Hydrogen bonding within the sheet is parallel to the fibril axis. Along the packing dimension, β-sheets are laminated together, spaced by 10Å (Figure 4.2c), to give a rectangular fibril. In this model structure, the side chains of the histidine residues at positions 13 and 14 are directed to opposite surfaces of the β sheet, and spaced 5 Å apart along the sheet (Figure 4.2b) (Morgan, Dong et al. 2002). Moreover, if the sheets along the packing dimension within the fiber are parallel, H13 and H14 residues from different sheets would also be proximal (Figure 4.2c).

Therefore, both arrangements provide potential chelating Zn^{2+} (or Cu^{2+}) binding sites, either along or between the sheets, or, in combination of the two. Figure 4.2 forms our working model for interpreting XAS results.

Herein we describe experiments utilizing X-ray absorption spectroscopy (XAS) to extend the investigations of Dr. Lynn's group at Emory University on fibril formation by Aβ peptides and reveal direct structural information about the metal binding sites (including both Zn^{2+} and Cu^{2+}). Most importantly, these studies present vital structural details of Zn^{2+} and Cu^{2+} complexes along the self-assembly pathway, which is crucial for understanding and possible prevention of amyloid formation at the early stage of Alzheimer's disease. In addition, self-assembled structures at nanoscale levels could be applied as templates for constructing novel nano-materials. For example, Zn^{2+} on the self-assembled templates could be converted to ZnS, which is an important semiconducting nanofibril, as well as nanoribbon (Fan, Meng et al. 2006).

Methods

Sample Preparation (performed by David Lynn's group at Emory University) Both purified Aβ(13-21)K16A and Ac-Aβ(13-21)H14A peptides were dissolved completely in distilled deionized H_2O with sonication for 10 min and centrifuged at 16,110xg for 10 min to remove preformed amorphous aggregates, if any. The supernatant was used as the peptide stock solution. Samples with 1mM Aβ(13-21)K16A, 25mM MES buffer at pH 5.6, 10 mM NaCl and the test Zn^{2+} concentrations (0 or 1 mM) were prepared from peptide stock solution, 50 mM MES stock buffer at pH 5.6, 1 M stock NaCl solution and 100 mM stock $ZnCl_2$ solution. The Cu samples were prepared by the same method using $CuCl_2$ (Dong, Shokes et al. 2006).

X-ray absorption spectroscopy. The data were collected at a temperature of 10 K, which was maintained by a continuous flow liquid helium cryostat. The averaged XAS data represent 10

scans, each of 21 min duration. EXAFSPAK software (www-ssrl.slac.stanford.edu/exafspak.html) was used for data reduction and analysis. Detailed curve-fitting analysis for Zn-$(im)_{1-3}$ multiple-scattering was performed according to procedures published by George et al (Ferreira, Franco et al. 2002). The oxygen shell was added manually allowing the distance and DW factor to vary. The multiple scattering model, was based on tetra(imidazole)zinc(II) (Bear, Duggen et al. 1975) and tetrakis(imidazole) copper(II) (Fransson and Lundberg 1972). In Table 4.1, the Debye-Waller factor for Zn-N_{1-3} was held constant at 0.0029 $Å^2$, calculated from the above method without optimization. The Cu samples were analyzed in the same fashion except in Table 4.3 the Debye-Waller factor for Cu-N_{1-3} was held constant at 0.0028 $Å^2$. In Table 4.4, the Cu-O bond distance was extracted from Table 4.3 (Fits 4 and 10) and held constant at 1.99 Å. The Cu-N bond stretch for multiple scattering calculations was determined by Universal Force Field method to be 129 N/m.

Results and Discussion

Aβ(13-21), HHQKLVFFA, includes both the core segment, Aβ(17-21), known to be crucial for fibril formation, and the metal binding dyad (Figure 4.1). To isolate His13/14 as the sole binding elements, the K16A peptide HHQALVFFA-NH_2, Aβ(13-21)K16A, was prepared. Experiments by Dr. Lynn's group illustrated that different Zn^{2+} concentrations dramatically altered both self-assembly kinetics and fibril morphology (Dong, Shokes et al. 2006). High resolution images obtained from atomic force microscopy (AFM) and transmission electron microscopy (TEM) experiments, revealed formation of fibrils at Zn^{2+} to peptide ratios as low as 0.2. At higher Zn^{2+} to peptide ratios (~1.0), the appearance of long helical ribbons were observed among the fibrils (fibers/ribbons), and at large integer ratios these fiber/ribbons complexes were shown to aggregate.

Struck by the different morphologies accessible to Aβ(13-21)K16A, we investigated the coordination environment of Zn^{2+} in the different assemblies by XAS. The soluble assembled metal-Aβ complexes were separated by centrifugation, and the fibers/ribbons were investigated either as resuspended solutions or directly as hydrated pellets, both of which showed identical XAS spectra (Figure 4.3). Both the intensity and the position of the Zn K-edge and EXAFS were consistent with four light elements (nitrogen or oxygen) in the coordination sphere of Zn^{2+} in the fibers/ribbons (Figure 4.4a), as well as the supernatant samples. Curve fitting indicated either 3N(Im)/1O or 2N(Im)/2O atoms in the first Zn shell for the fiber/ribbon samples (Table 4.1 and 4.2) and 4O or 3O/1N(Im) in the supernatant (where N(Im) implies histidine imidazole coordination). The coincident appearances of the 3- and 4-Å peaks in the Fourier transform (Figure 4.4b) of the fiber/ribbon EXAFS data (inset of Figure 4.4b) are diagnostic for two distinct imidazole ligands. The Zn^{2+} coordination environment in the fibers, $[Zn^{2+}]$/[peptide] = 0.2 and 0.6, are essentially identical; however, both the Zn K-edge absorption and EXAFS change when the Zn^{2+} to Aβ(13-21)K16A ratio reaches 1.0. The unusual relative intensities at 3 Å and 4 Å, which are typically equal in height as shown in the low $[Zn^{2+}]$ samples, could be the result of angular distortion of the imidazoles. In summary, the local Zn^{2+} coordination environment changes coincident with the change in morphology.

To test whether the difference in coordination environments observed in XAS and the associated morphologies may reflect different intra- and inter-sheet Zn^{2+} chelation, Ac-Aβ(13-21)H14A (Ac-HAQKLVFFA-NH_2) was investigated. As indicated in Figure 4.1, removal of His14 should eliminate inter-sheet metal binding while preserving coordination along the sheet surface. Dr. Lynn's group confirmed that Ac-Aβ(13-21)H14A formed fibrils in the absence of Zn^{2+}, showing the characteristic β-signature, and in the presence of 1 equiv of Zn^{2+}, the β-

signature developed more rapidly at least up to a [Zn^{2+}]/[peptide] ratio of 2.0. The XAS results for the Zn^{2+} complex of Ac-Aβ(13-21)H14A were also consistent with a first Zn coordination shell of 3N(Im)/1O or 2N(Im)/2O atoms (Figure. 4.5 and Tables 4.1 and 4.2). The appearance of the 3- and 4-Å peaks in the Fourier transform of the EXAFS again are diagnostic for two imidazoles, consistent with two His13's on one face of the β-sheet chelating Zn^{2+}, similar to that seen for Aβ(13-21)K16A at low [Zn^{2+}]. Such intra-sheet His-Zn^{2+}-His chelation could stabilize the side chain packing along the sheet and therefore explain the acceleration of β sheet growth. The intensity of the first-shell Fourier transform peaks around 2 Å in the Ac-Aβ(13-21)H14A fibrils is greater than in the Aβ(13-21)K16A assemblies, implying that Ac-Aβ(13-21)H14A fibrils contain greater inherent local order (Figure 4.5b).

The stimulative and inhibitory effects of Cu^{2+} on Aβ aggregation have been well documented and predict that under normal physiological conditions, Cu^{2+} can actually compete with Zn(II) for histidine residues in Aβ peptide inhibiting Zn^{2+}-induced aggregation (Atwood, Moir et al. 1998; Miura, Suzuki et al. 2000). Experiments performed by Dr. Lynn's group found that Cu^{2+} inhibits the assembly process (fibril formation) of Aβ(13-21)K16A. They suggest that this occurs by distorting the backbone of Aβ(13-21)K16A through the binding of Cu^{2+} with histidine residues and main chain amide groups forming soluble Cu(II)-Aβ(13-21)K16A complexes (no detectable fibril formation). In contrast, it was found that Cu^{2+} stimulates fibril formation of Ac-Aβ(13-21)H14A-NH_2, suggesting that Cu^{2+} binding is capable of inducing fibril formation (Dong J, Lynn DG, private communication). Thus, to further understand the role of metals on amyloid formation, we examined the Cu^{2+} binding modes of Aβ(13-21) in solution (K16A peptide) and in insoluble aggregates (H14A peptide) by XAS in order correlate the morphological effects of Cu^{2+} with specific metal-binding geometries.

In Figure 4.6a, the Cu K edge data reveal slightly different spectra for soluble Cu^{2+}-Aβ(13-21)K16A and Cu^{2+}-Aβ(13-21)H14A (hydrated pellet), both spectra being consistent with the metal in the +2 oxidation state bound to four light scattering atoms. The FTs (Figure 4.6b) of both samples also reveal peaks at 3 and 4 Å, indicative of imidazole scattering. However, the FT peaks of the Cu^{2+}-Aβ(13-21)K16A complexes have slightly lower amplitude, suggesting less contribution from imidazole ligands or possibly destructive interference from other contributing ligands. Furthermore, the FT peak at around 2 Å in the Ac-Aβ(13-21)H14A fibrils is more intense than in the soluble Aβ(13-21)K16A complex, again implying that Ac-Aβ(13-21)H14A fibrils contain less heterogeneity and greater inherent local order (Figure 4.6b).These results suggest slightly different coordination spheres for the two Cu bound complexes, in agreement with the morphological effects of Cu^{2+} on fibril formation determined by Dr. Lynn's group.

The XAS results for the Cu^{2+}-fibrillar complex of Ac-Aβ(13-21)H14A were consistent with a first Cu coordination shell of 3N(Im)/1O or 2N(Im)/2O atoms (Figure 4.7 and Tables 4.3 and 4.4). The two imidazole ligands presumably arise from the two His13's on one face of the β-sheet, forming a His-Cu^{2+}-His chelation, identical to the Zn Ac-Aβ(13-21)H14A complex. Curve-fitting analysis of the soluble Cu^{2+}-Aβ(13-21)K16A complex indicated 3N/1O or 2N/2O (Table 4.3) atoms in the first shell, and multiple scattering fits are consistent with the presence of two imidazole ligands (Table 4.4). Overall the data suggest similar coordination environments (Cu-$(imid)_2(N/O)_2$) for the Cu bound forms of Aβ(13-21)K16A and Aβ(13-21)H14A.

Transition metals have been implicated in amyloid fibril assembly for several years, but their ability to alter fibril morphology is not generally appreciated. By resolving a single binding site in the amyloid array and observing the metal directly, we have taken the first steps to reveal how metal coordination may dictate amyloid assembly morphology. These data establish that the

single His13 in Aβ(13-21)H14A is sufficient to coordinate Zn^{2+} and Cu^{2+} productively for amyloid self-assembly and that His13 residues on two peptides chelate the metal along the entire face of each β-sheet. In Aβ(13-21)K16A, where the His13/His14 dyad is present, distinct Zn^{2+} coordination can be accessed at elevated [Zn^{2+}] exploiting the His residues on each side of the β-sheets to stabilize sheet/sheet associations (lamination) and the transition to the ribbon/tube morphology. These characteristic spectroscopic signatures can now be investigated in the full length Aβ assemblies allowing us to determine whether the different coordination complexes occur in the more complex structures, form with different metals, reveal distinctly different chemical reactivity, and/or mediate cellular toxicity. The emerging structures should also provide models for developing therapeutic intervention strategies.

Acknowledgment

The XAS data were collected at the Stanford Synchrotron Radiation Laboratory, a national user facility operated by Stanford University on behalf of the U.S. Department of Energy, Office of Basic Energy Sciences. The SSRL Structural Molecular Biology Program is supported by the Department of Energy, Office of Biological and Environmental Research, and by the National Institutes of Health, National Center for Research Resources, and Biomedical Technology Program. We thank DOE ER15377 (D.G.L.) and NIH GM42025 (R.A.S.) for support, NSF (CHE-0131013) for CD instrumentation, Emory microscopy core laboratory for TEM, and C.L. Emerson for AFM instrumentation.

References

Atwood, C. S., R. D. Moir, et al. (1998). "Dramatic aggregation of Alzheimer abeta by Cu(II) is induced by conditions representing physiological acidosis." J Biol Chem **273**(21): 12817-26.

Atwood, C. S., R. D. Moir, et al. (1998). "Dramatic aggregation of Alzheimer A beta by Cu(II) is induced by conditions representing physiological acidosis." Journal of Biological Chemistry **273**(21): 12817-12826.

Bear, C. A., K. A. Duggen, et al. (1975). Acta Crystallogr. Sec. B **31**: 2713.

Brown, A. M., D. M. Tummolo, et al. (1997). "Selective aggregation of endogenous beta-amyloid peptide and soluble amyloid precursor protein in cerebrospinal fluid by zinc." Journal of Neurochemistry **69**(3): 1204-1212.

Burkoth, T. S., T. L. S. Benzinger, et al. (2000). "Structure of the beta-amyloid((10-35)) fibril." Journal of the American Chemical Society **122**(33): 7883-7889.

Bush, A. I., W. H. Pettingell, et al. (1994). "Rapid Induction of Alzheimer a-Beta Amyloid Formation by Zinc." Science **265**(5177): 1464-1467.

Dong, J., J. E. Shokes, et al. (2006). "Modulating amyloid self-assembly and fibril morphology with Zn(II)." J Am Chem Soc **128**(11): 3540-2.

Fan, X., X. M. Meng, et al. (2006). "Dart-Shaped Tricrystal ZnS Nanoribbons." Angew Chem Int Ed Engl **45**(16): 2568-2571.

Ferreira, G. C., R. Franco, et al. (2002). "Unraveling the substrate-metal binding site of ferrochelatase: an X-ray absorption spectroscopic study." Biochemistry **41**(15): 4809-18.

Fransson, G. and B. K. Lundberg (1972). "Metal-Complexes with Mixed-Ligands .4. Crystal-Structure of Tetrakisimidazole Cu(Ii) Sulfate, Cu(C3h4n2)4so4." Acta Chemica Scandinavica **26**(10): 3969-3976.

Lakdawala, A. S., D. M. Morgan, et al. (2002). "Dynamics and fluidity of amyloid fibrils: a model of fibrous protein aggregates." J Am Chem Soc **124**(51): 15150-1.

Lynn, D. G. and S. C. Meredith (2000). "Review: Model peptides and the physicochemical approach to beta-amyloids." Journal of Structural Biology **130**(2-3): 153-173.

Masters, C. L., G. Simms, et al. (1985). "Amyloid Plaque Core Protein in Alzheimer-Disease and Down Syndrome." Proceedings of the National Academy of Sciences of the United States of America **82**(12): 4245-4249.

Miura, T., K. Suzuki, et al. (2000). "Metal binding modes of Alzheimer's amyloid beta-peptide in insoluble aggregates and soluble complexes." Biochemistry **39**(23): 7024-31.

Morgan, D. M., J. Dong, et al. (2002). "Metal switch for amyloid formation: insight into the structure of the nucleus." J Am Chem Soc **124**(43): 12644-5.

Morgan, D. M., A. Lakdawala, et al. (2002). "Self-assembly of abeta(10-35) fibrils." Abstracts of Papers of the American Chemical Society **223**: C21-C21.

Selkoe, D. J. (1994). "Alzheimer's disease: a central role for amyloid." J Neuropathol Exp Neurol **53**(5): 438-47.

Selkoe, D. J. (1994). "Amyloid beta-protein precursor: new clues to the genesis of Alzheimer's disease." Curr Opin Neurobiol **4**(5): 708-16.

Suh, S. W., K. B. Jensen, et al. (2000). "Histochemically-reactive zinc in amyloid plaques, angiopathy, and degenerating neurons of Alzheimer's diseased brains." Brain Research **852**(2): 274-278.

Suzuki, K., T. Miura, et al. (2001). "Inhibitory effect of copper(II) on zinc(II)-induced aggregation of amyloid beta-peptide." Biochem Biophys Res Commun **285**(4): 991-6.

Figure Legends

Figure 4.1. Schematic relationships among the β-Amyloid Precursor Protein (βAPP), the Amyloid-β protein (Aβ), and the peptide used herein (Aβ(13-21)K16A). Dotted lines represent the domain boundaries separating the extracellular (EC), transmembrane (TM), and cytoplasmic tail (CT) domains of βAPP. Substitution of K16 by A increases the hydrophobicity and amphiphilicity of the peptide, promoting fibril formation.

Figure 4.2. (a) Single extended β-strand in a six-sheet laminated fibril form; (b) stick representation of β-strands aggregated in parallel fashion with in-register β-sheets spaced 5 Å apart and hypothetical Zn(II) bridging strands within the sheet; (c) hypothetical Zn(II) binding sites between different β-sheets laminated together along the packing dimension with 10 Å spacing. Blue: nitrogen; red: oxygen; magenta: Zn.

Figure 4.3. Zn K-edge X-ray absorption spectrum (a) and Fourier transforms (k = 2 – 13 Å^{-1}; k^3 weighting) (b) of the EXAFS (inset of b) for 1:1 Zn^{2+}:Aβ(13-21)K16A, either as re-dissolved pellet (dashed line) or solid pellet (solid line). The Zn^{2+} environment is essentially identical, not affected by re-dissolution of the pellet.

Figure 4.4. Zn *K*-edge X-ray absorption spectrum (a) and Fourier transforms (k = 2 – 13 Å^{-1}; k^3 weighting) (b) of the EXAFS (inset of b) for Zn^{2+} in Aβ(13-21)K16A assemblies formed with initial [Zn^{2+}]/[Aβ(13-21)K16A] = 0.2 (dotted), 0.6 (dashed), and 1.0 (solid)

Figure 4.5. Zn K-edge X-ray absorption spectrum (a) and Fourier transforms (k = 2 – 13 Å^{-1}; k^3 weighting) (b) of the EXAFS (inset of b) for Zn^{2+} in Aβ(13-21)K16A assemblies formed with

initial $[Zn^{2+}]/[A\beta(13\text{-}21)K16A]=0.6$ (dashed) and 1.0 (dotted), as well as Ac-Aβ(13-21)H14A assemblies formed with initial $[Zn^{2+}]/[Ac\text{-}A\beta(13\text{-}21)H14A]=1.0$ (solid).

Figure 4.6. Cu-K edge X-ray absorption spectrum (a) and Fourier transforms (k = 2 – 13 $Å^{-1}$; k^3 weighting) (b) of the EXAFS (inset of b) for $[Cu^{2+}]/[A\beta(13\text{-}21)K16A]=1.0$ (dashed) and $[Cu^{2+}]/[Ac\text{-}A\beta(13\text{-}21)H14A]=1.0$ (solid).

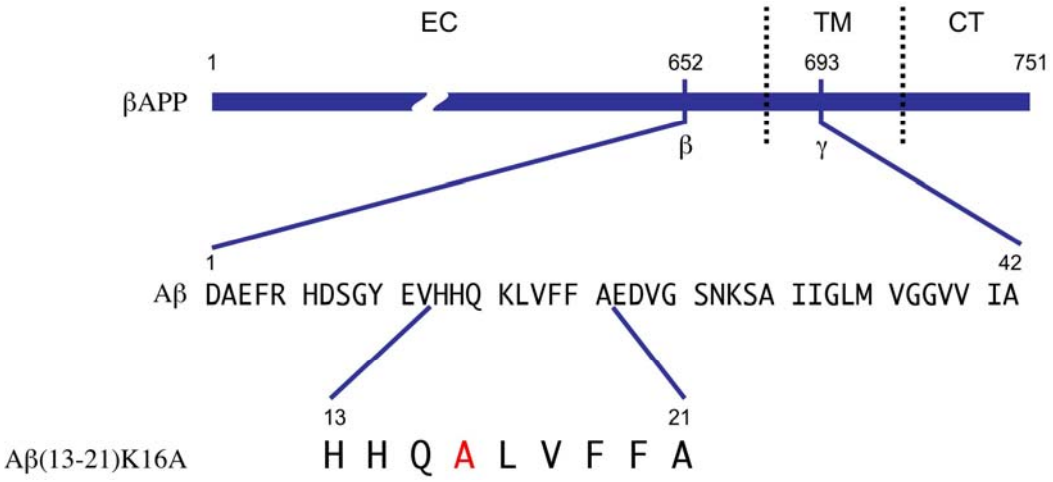
EC
TM
CT
1
652
693
751
βAPP
β
γ
1
42
Aβ DAEFR HDSGY EVHHQ KLVFF AEDVG SNKSA IIGLM VGGVV IA
13
21
Aβ(13-21)K16A
H H Q A L V F F A

Figure 4.1

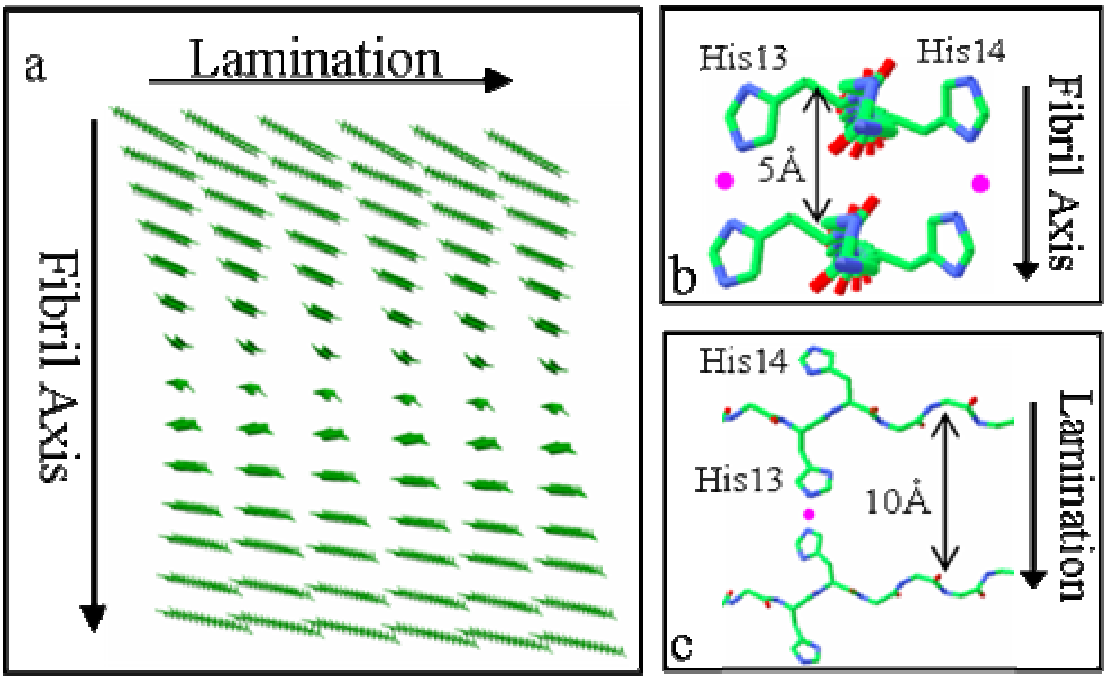
a
Lamination
Fibril Axis
His13
His14
5Å
Fibril Axis
b
His14
His13
10Å
Lamination
c

Figure 4.2

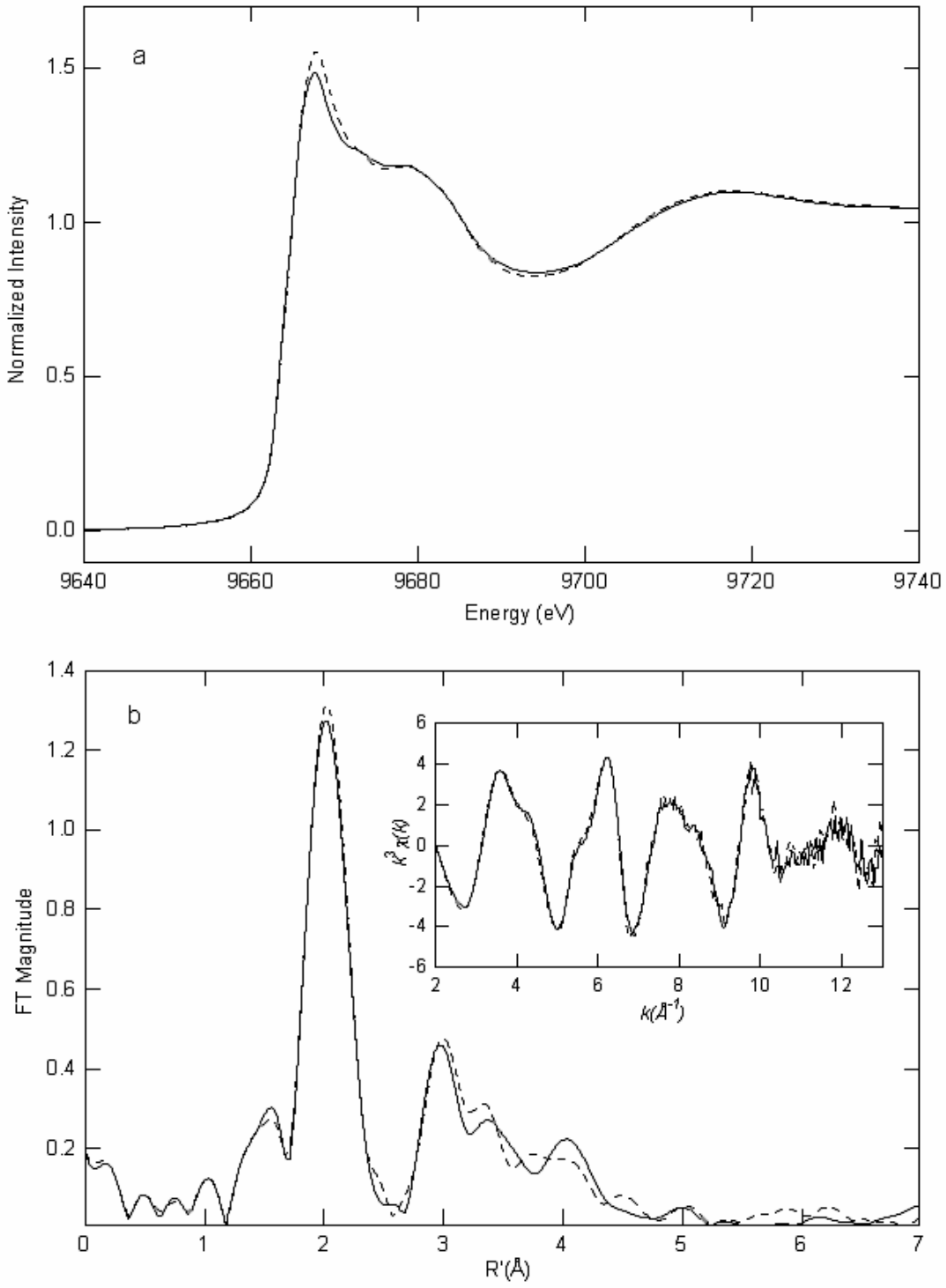
a
Normalized Intensity
Energy (eV)
b
FT Magnitude
R'(Å)
$k^3\chi(k)$
$k(Å^{-1})$

Figure 4.3

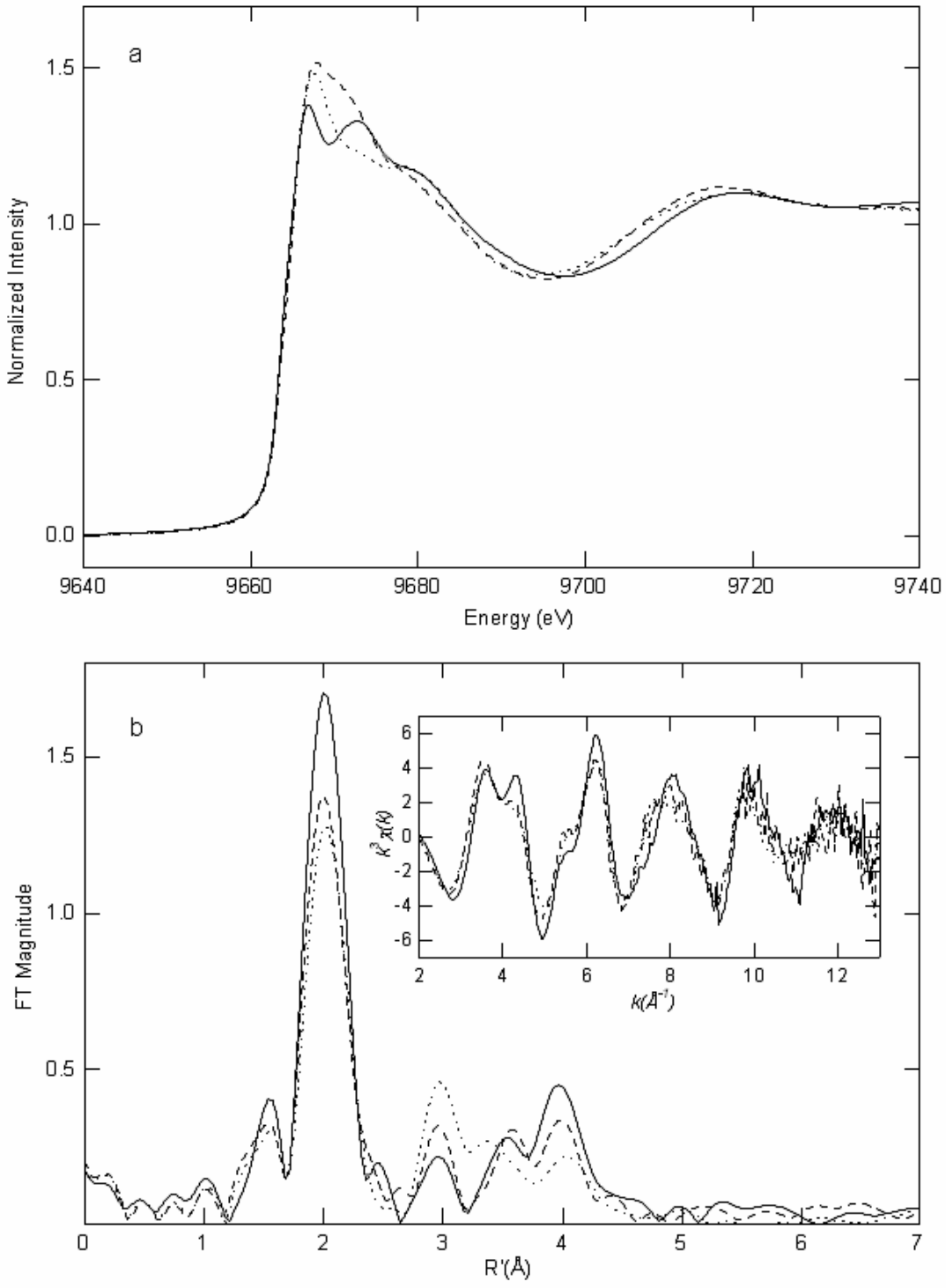
a
Normalized Intensity
Energy (eV)
b
FT Magnitude
R'(Å)
$k^3\chi(k)$
$k(Å^{-1})$

Figure 4.4

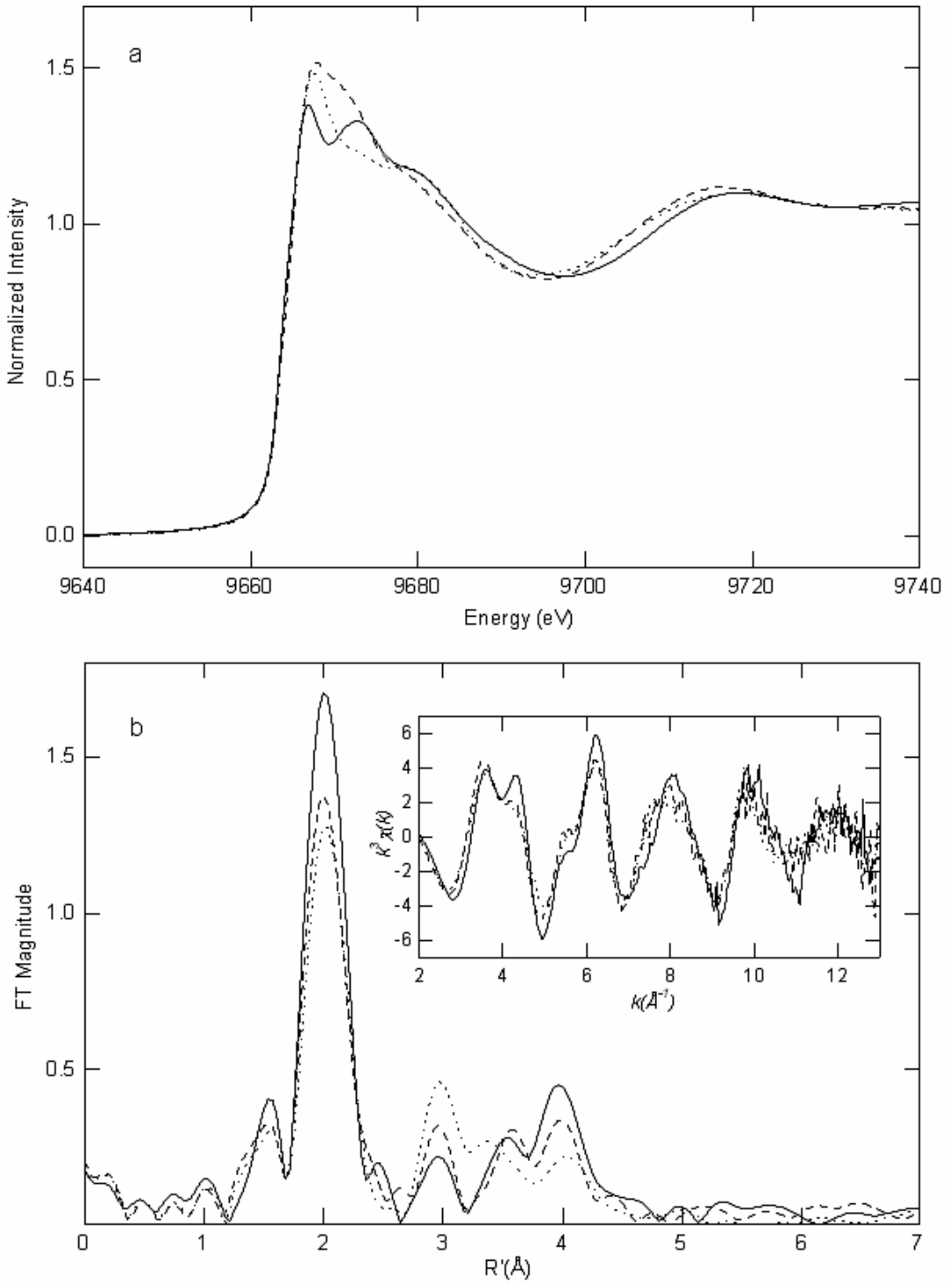
a
Normalized Intensity
Energy (eV)
b
FT Magnitude
R'(Å)
$k^3\chi(k)$
$k(Å^{-1})$

Figure 4.5

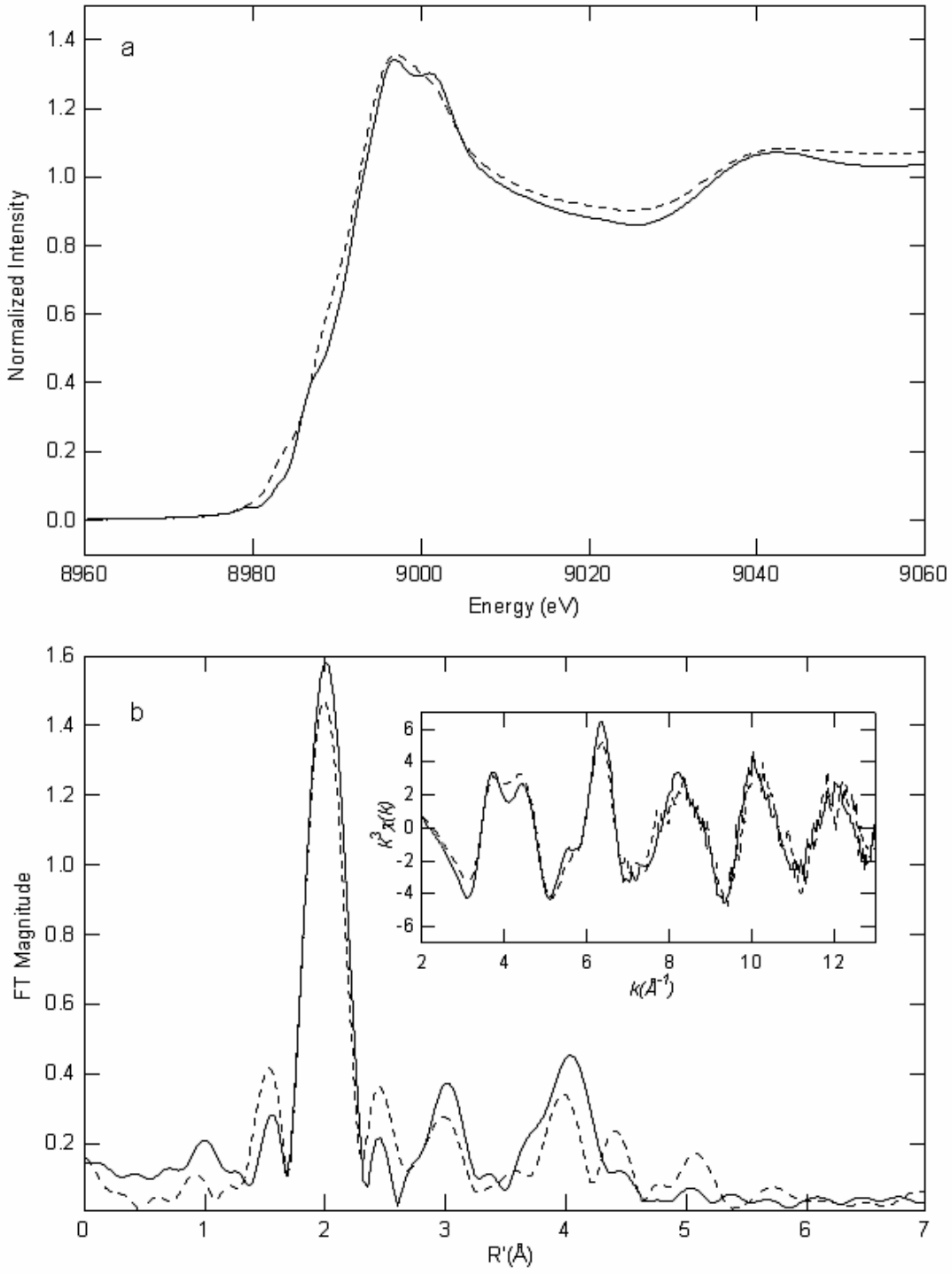
a
Normalized Intensity
Energy (eV)
b
FT Magnitude
R'(Å)
$k^3\chi(k)$
$k(Å^{-1})$

Figure 4.6

Table 4.1. Curve fitting results for EXAFS[a]

Sample filename (k range) $\Delta k^3\chi$	Fit	Shell	R_{as} (Å)	σ_{as}^2 (Å^2)	ΔE_0 (eV)	f[b]	BVS[c]
A-β(13-21)K16A	1	Zn-N_4	2.01	0.0047	–8.25	0.111	2.13
Z10PA (Δk = 2-13 Å^{-1})	2	Zn-N_5	2.01	0.0063	–8.44	0.108	2.66
$\Delta k^3\chi$ = 8.65	3	Zn-N_3	1.97	[0.0029]	–8.49	0.109	2.16
		Zn-O_1	2.06	0.0006			
	4	Zn-N_2	1.95	[0.0029]	–8.20	0.110	2.08
		Zn-O_2	2.03	0.0026			
	5	Zn-N_1	1.92	[0.0029]	–8.18	0.111	2.03
		Zn-O_3	2.00	0.0037			
	6	Zn-O_4	2.01	0.0048	–8.25	0.113	1.75
A-β(13-21)K16A	7	Zn-N_4	2.00	0.0044	–10.09	0.121	2.18
Z06PA (Δk = 2-13 Å^{-1})	8	Zn-N_5	2.00	0.0058	–10.25	0.116	2.73
$\Delta k^3\chi$ = 9.26	9	Zn-N_3	1.97	[0.0029]	–10.17	0.120	2.17
		Zn-O_1	2.05	0.0015			
	10	Zn-N_2	1.96	[0.0029]	–9.55	0.119	2.07
		Zn-O_2	2.02	0.0036			
	11	Zn-N_1	1.94	[0.0029]	–9.29	0.118	2.03
		Zn-O_3	1.99	0.0046			

	12	Zn-O_4	1.98	0.0057	–9.19	0.119	1.90
A-β(13-21)K16A	13	Zn-N_4	2.00	0.0050	–10.45	0.137	2.19
Z02RA (Δk = 2-13 Å^{-1})	14	Zn-N_5	2.00	0.0065	–10.64	0.132	2.73
$\Delta k^3\chi$ = 9.75	15	Zn-N_3	1.96	[0.0029]	–10.73	0.135	2.22
		Zn-O_1	2.05	0.0009			
	16	Zn-N_2	1.95	[0.0029]	–10.12	0.135	2.03
		Zn-O_2	2.05	0.0036			
	17	Zn-N_1	1.93	[0.0029]	–9.95	0.134	2.01
		Zn-O_3	2.00	0.0048			
	18	Zn-O_4	1.97	0.0064	–9.77	0.134	1.95
A-β(13-21)H14A	19	Zn-N_4	1.99	0.0029	–6.94	0.090	2.24
Z20PB (Δk = 2-13 Å^{-1})	20	Zn-N_5	1.99	0.0041	–7.33	0.085	2.80
$\Delta k^3\chi$ = 11.84	21	Zn-N_3	1.97	[0.0029]	–7.35	0.090	2.21
		Zn-O_1	2.01	0.0010			
	22	Zn-N_2	1.96	[0.0029]	–6.71	0.089	2.14
		Zn-O_2	1.99	0.0023			
	23	Zn-N_1	1.93	[0.0029]	–6.25	0.088	2.08
		Zn-O_3	1.98	0.0029			
	24	Zn-O_4	1.97	0.0040	–6.25	0.088	1.95

[a] Shell is the chemical unit defined for the multiple scattering calculation. Subscripts denote the number of scatterers per metal. R_{as} is the metal-scatterer distance. σ_{as}^2 is a mean square deviation in R_{as}. ΔE_0 is the shift in E_0 for the theoretical scattering functions.

[b] f' is a normalized error (chi-squared):

$$f' = \frac{\left\{ \sum_i \left[k^3 \left(\chi_i^{obs} - \chi_i^{calc} \right) \right]^2 / N \right\}^{1/2}}{\left[\left(k^3 \chi^{obs} \right)_{max} - \left(k^3 \chi^{obs} \right)_{min} \right]}$$

[c] BVS=$\Sigma\exp[(r_o-r)/0.37]$, r_0(Zn(II)-O)=1.704, r_0(Zn(II)-N)=1.776. (Thorp, 1991)

[d] Numbers in square brackets were constrained to be either a multiple of the above value ($\Delta_{as}2$) or to maintain a constant difference from the above value (R_{as}, ΔE_0,).

Table 4.2. Curve fitting results for EXAFS[a]

Sample filename (k range) $\Delta k^3\chi$	Fit	Shell	R_{as} (Å)	σ_{as}^2 (Å^2)	ΔE_0 (eV)	f[b]	BVS[c]
A-β(13-21)K16A	1	Zn-O_3	2.01	0.0061	–3.85	0.096	1.94
Z10PA (Δk = 2-13 Å^{-1})		Zn-N_1	1.95	0.0025			
$\Delta k^3\chi$ = 8.65		Zn-C_1	[2.92]	[0.0036]			
		Zn-C_1	[2.99]	[0.0033]			
		Zn-N_1	[4.06]	[0.0038]			
		Zn-C_1	[4.07]	[0.0049]			
	2	Zn-O_2	2.06	0.0053	–0.43	0.084	1.95
		Zn-N_2	1.97	0.0026			
		Zn-C_2	[2.95]	[0.0036]			
		Zn-C_2	[3.02]	[0.0034]			
		Zn-N_2	[4.10]	[0.0039]			
		Zn-C_2	[4.11]	[0.0050]			
	3	Zn-O_1	2.08	0.0021	0.90	0.085	2.09
		Zn-N_3	1.98	0.0035			
		Zn-C_3	[2.97]	[0.0045]			
		Zn-C_3	[3.03]	[0.0043]			
		Zn-N_3	[4.12]	[0.0048]			
		Zn-C_3	[4.13]	[0.0059]			

A-β(13-21)K16A	4	$Zn\text{-}O_3$	2.03	0.0066	–3.17	0.107	1.85
Z06PA (Δk = 2-13 Å^{-1})		$Zn\text{-}N_1$	1.96	0.0002			
$\Delta k^3\chi$ = 9.26		$Zn\text{-}C_1$	[2.93]	[0.0013]			
		$Zn\text{-}C_1$	[3.00]	[0.0011]			
		$Zn\text{-}N_1$	[4.08]	[0.0016]			
		$Zn\text{-}C_1$	[4.08]	[0.0027]			
	5	$Zn\text{-}O_2$	2.06	0.0050	–0.90	0.102	1.95
		$Zn\text{-}N_2$	1.97	0.0015			
		$Zn\text{-}C_2$	[2.95]	[0.0025]			
		$Zn\text{-}C_2$	[3.01]	[0.0023]			
		$Zn\text{-}N_2$	[4.10]	[0.0028]			
		$Zn\text{-}C_2$	[4.10]	[0.0039]			
	6	$Zn\text{-}O_1$	2.10	0.0029	–0.95	0.105	2.07
		$Zn\text{-}N_3$	1.98	0.0025			
		$Zn\text{-}C_3$	[2.97]	[0.0036]			
		$Zn\text{-}C_3$	[3.04]	[0.0033]			
		$Zn\text{-}N_3$	[4.13]	[0.0038]			
		$Zn\text{-}C_3$	[4.14]	[0.0049]			
A-β(13-21)K16A	7	$Zn\text{-}O_3$	2.02	0.0067	1.48	0.125	1.90
Z02RA (Δk = 2-13 Å^{-1})		$Zn\text{-}N_1$	1.95	0.0010			

$\Delta k^3\chi = 9.75$		$Zn\text{-}C_1$	[2.91]	[0.0021]			
		$Zn\text{-}C_1$	[2.98]	[0.0019]			
		$Zn\text{-}N_1$	[4.05]	[0.0024]			
		$Zn\text{-}C_1$	[4.05]	[0.0035]			
	8	$Zn\text{-}O_2$	2.06	0.0051	−1.69	0.121	1.98
		$Zn\text{-}N_2$	1.96	0.0020			
		$Zn\text{-}C_2$	[2.94]	[0.0031]			
		$Zn\text{-}C_2$	[3.00]	[0.0028]			
		$Zn\text{-}N_2$	[4.08]	[0.0033]			
		$Zn\text{-}C_2$	[4.09]	[0.0044]			
	9	$Zn\text{-}O_1$	2.09	0.0048	1.44	0.123	2.08
		$Zn\text{-}N_3$	1.98	0.0039			
		$Zn\text{-}C_3$	[2.97]	[0.0050]			
		$Zn\text{-}C_3$	[3.04]	[0.0047]			
		$Zn\text{-}N_3$	[4.13]	[0.0052]			
		$Zn\text{-}C_3$	[4.13]	[0.0063]			
A-β(13-21)H14A	10	$Zn\text{-}O_3$	1.99	0.0038	0.86	0.075	2.01
Z20PB (Δk = 2-13 $Å^{-1}$)		$Zn\text{-}N_1$	1.94	0.0018			
$\Delta k^3\chi = 11.84$		$Zn\text{-}C_1$	[2.91]	[0.0027]			
		$Zn\text{-}C_1$	[2.98]	[0.0025]			
		$Zn\text{-}N_1$	[4.05]	[0.0030]			

	$Zn\text{-}C_1$	[4.06]	[0.0033]			
11	$Zn\text{-}O_2$	2.01	0.0030	–0.17	0.067	2.09
	$Zn\text{-}N_2$	1.96	0.0030			
	$Zn\text{-}C_2$	[2.93]	[0.0040]			
	$Zn\text{-}C_2$	[3.00]	[0.0038]			
	$Zn\text{-}N_2$	[4.08]	[0.0043]			
	$Zn\text{-}C_2$	[4.08]	[0.0054]			
12	$Zn\text{-}O_1$	2.02	0.0043	2.00	0.070	2.15
	$Zn\text{-}N_3$	1.98	0.0023			
	$Zn\text{-}C_3$	[2.97]	[0.0034]			
	$Zn\text{-}C_3$	[3.03]	[0.0032]			
	$Zn\text{-}N_3$	[4.12]	[0.0037]			
	$Zn\text{-}C_3$	[4.13]	[0.0048]			

[a] Shell is the chemical unit defined for the multiple scattering calculation. Subscripts denote the number of scatterers per metal. R_{as} is the metal-scatterer distance. σ_{as}^2 is a mean square deviation in R_{as}. ΔE_0 is the shift in E_0 for the theoretical scattering functions.

[b] f' is a normalized error (chi-squared):

$$f' = \frac{\left\{ \sum_i \left[k^3 \left(\chi_i^{obs} - \chi_i^{calc} \right) \right]^2 / N \right\}^{1/2}}{\left[\left(k^3 \chi^{obs} \right)_{max} - \left(k^3 \chi^{obs} \right)_{min} \right]}$$

[c] BVS=$\Sigma\exp[(r_o-r)/B]$, B=0.37, r_0(Zn(II)-O)=1.704, r_0(Zn(II)-N)=1.776. (Thorp, 1991)

[d] Numbers in square brackets were constrained to be either a multiple of the above value ($\Delta_{as}2$) or to maintain a constant difference from the above value (R_{as}, ΔE_0,).

Table 4.3. Curve fitting results for Cu EXAFS[a]

Sample filename (k range) $\Delta k^3\chi$	Fit	Shell	R_{as} (Å)	σ_{as}^2 (Å^2)	ΔE_0 (eV)	f[b]	BVS[c]
A-β(13-21)K16A + Cu	1	Cu-N_4	1.97	0.0035	–7.12	0.090	2.21
C10SA (Δk = 2-13 Å^{-1})	2	Cu-N_5	1.97	0.0050	–6.98	0.095	2.77
$\Delta k^3\chi$ = 10.03	3	Cu-N_3	1.96	[0.0028]	–6.25	0.089	2.09
		Cu-O_1	2.00	0.0050			
	4	Cu-N_2	1.94	[0.0028]	–6.32	0.090	2.02
		Cu-O_2	1.99	0.0029			
	5	Cu-N_1	1.83	[0.0028]	–8.74	0.090	2.13
		Cu-O_3	1.96	0.0087			
	6	Cu-O_4	1.95	0.0049	–5.44	0.096	1.77
A-β(13-21)H14A + Cu	7	Cu-N_4	1.97	0.0030	–6.70	0.082	2.21
C10PB (Δk = 2-13 Å^{-1})	8	Cu-N_5	1.98	0.0044	–6.82	0.084	2.70
$\Delta k^3\chi$ = 11.56	9	Cu-N_3	1.95	[0.0028]	–6.95	0.082	2.13
		Cu-O_1	2.01	0.0006			
	10	Cu-N_2	1.92	[0.0028]	–7.06	0.083	2.06
		Cu-O_2	1.99	0.0011			
	11	Cu-N_1	1.87	[0.0028]	–7.16	0.084	1.98
		Cu-O_3	1.97	0.0019			

12	Cu-O_4	1.97	0.0043	–6.57	0.088	1.67

[a] Shell is the chemical unit defined for the multiple scattering calculation. Subscripts denote the number of scatterers per metal. R_{as} is the metal-scatterer distance. σ_{as}^2 is a mean square deviation in R_{as}. ΔE_0 is the shift in E_0 for the theoretical scattering functions.

[b] f' is a normalized error (chi-squared):

$$f' = \frac{\left\{ \sum_i \left[k^3 \left(\chi_i^{obs} - \chi_i^{calc} \right) \right]^2 / N \right\}^{1/2}}{\left[\left(k^3 \chi^{obs} \right)_{max} - \left(k^3 \chi^{obs} \right)_{min} \right]}$$

[c] BVS=$\Sigma\exp[(r_o\text{-}r)/B]$, B=0.37,], r_0(Cu(II)-N)=1.751, r_0(Cu(II)-O)=1.649 (Thorp, 1991)

[d] Numbers in square brackets were constrained to be either a multiple of the above value ($\Delta_{as}2$) or to maintain a constant difference from the above value (R_{as}, ΔE_0,).

Table 4.4. Curve fitting results for Cu EXAFS[a]

Sample filename (k range) $\Delta k^3\chi$	Fit	Shell	R_{as} (Å)	σ_{as}^2 (Å2)	ΔE_0 (eV)	f[b]	BVS[c]
A-β(13-21)K16A + Cu	1	$Cu\text{-}O_3$	[1.99]	0.0074	–0.36	0.092	1.78
C10SA (Δk = 2-13 Å^{-1})		$Cu\text{-}N_1$	1.95	–0.002			
$\Delta k^3\chi$ = 10.03		$Cu\text{-}C_1$	[2.90]	[–0.0003]			
		$Cu\text{-}C_1$	[2.95]	[–0.0003]			
		$Cu\text{-}N_1$	[4.02]	[–0.0004]			
		$Cu\text{-}C_1$	[4.06]	[–0.0004]			
	2	$Cu\text{-}O_2$	[1.99]	0.0053	–0.05	0.089	1.96
		$Cu\text{-}N_2$	1.95	0.0030			
		$Cu\text{-}C_2$	[2.90]	[0.0039]			
		$Cu\text{-}C_2$	[2.96]	[0.0039]			
		$Cu\text{-}N_2$	[4.03]	[0.0047]			
		$Cu\text{-}C_2$	[4.06]	[0.0057]			
	3	$Cu\text{-}O_1$	[1.99]	0.0006	0.88	0.093	2.15
		$Cu\text{-}N_3$	1.95	0.0061			
		$Cu\text{-}C_3$	[2.91]	[0.0081]			
		$Cu\text{-}C_3$	[2.96]	[0.0081]			
		$Cu\text{-}N_3$	[4.03]	[0.0097]			
		$Cu\text{-}C_3$	[4.06]	[0.0117]			

A-β(13-21)H14A + Cu	4	$Cu\text{-}O_3$	1.98	0.0047	–2.11	0.077	1.81
C10PB (Δk = 2-13 Å^{-1})		$Cu\text{-}N_1$	1.95	0.0017			
$\Delta k^3\chi$ = 11.56		$Cu\text{-}C_1$	[2.90]	[0.0022]			
		$Cu\text{-}C_1$	[2.95]	[0.0022]			
		$Cu\text{-}N_1$	[4.02]	[0.0026]			
		$Cu\text{-}C_1$	[4.06]	[0.0032]			
	5	$Cu\text{-}O_2$	1.99	0.0030	–0.13	0.071	1.96
		$Cu\text{-}N_2$	1.95	0.0038			
		$Cu\text{-}C_2$	[2.91]	[0.0050]			
		$Cu\text{-}C_2$	[2.96]	[0.0050]			
		$Cu\text{-}N_2$	[4.03]	[0.0060]			
		$Cu\text{-}C_2$	[4.06]	[0.0072]			
	6	$Cu\text{-}O_1$	2.00	0.0068	2.28	0.069	2.09
		$Cu\text{-}N_3$	1.96	0.0048			
		$Cu\text{-}C_3$	[2.93]	[0.0063]			
		$Cu\text{-}C_3$	[2.98]	[0.0063]			
		$Cu\text{-}N_3$	[4.05]	[0.0075]			
		$Cu\text{-}C_3$	[4.09]	[0.0091]			

[a] Shell is the chemical unit defined for the multiple scattering calculation. Subscripts denote the number of scatterers per metal. R_{as} is the metal-scatterer distance. σ_{as}^2 is a mean square deviation in R_{as}. ΔE_0 is the shift in E_0 for the theoretical scattering functions.

[b] f' is a normalized error (chi-squared):

$$f' = \frac{\left\{ \sum_i \left[k^3 \left(\chi_i^{obs} - \chi_i^{calc} \right) \right]^2 / N \right\}^{1/2}}{\left[\left(k^3 \chi^{obs} \right)_{max} - \left(k^3 \chi^{obs} \right)_{min} \right]}$$

[c] BVS=$\Sigma\exp[(r_o-r)/B]$, B=0.37,], r_0(Cu(II)-N)=1.751, r_0(Cu(II)-O)=1.649 (Thorp, 1991)

[d] Numbers in square brackets were constrained to be either a multiple of the above value ($\Delta_{as}2$) or to maintain a constant difference from the above value (R_{as}, ΔE_0,).

CHAPTER 5

STRUCTURAL ELEMENTS OF METAL SELECTIVITY IN METAL SENSOR PROTEINS

Introduction

About one-third of all proteins exploit specific metal ions to assist in macromolecular folding and or function at the active site of metalloenzymes (Rosenzweig 2002). All cells restrict the number of bioavailable metal atoms to avoid any excess that would otherwise compete with native metal ion sites that do not support biological activity (O'Halloran 1993). Essentially all cell types contain intracellular metal sensors that detect surplus metal ions and control the expression of genes encoding proteins that expel or sequester the extra ions. For some metals and some cell types, a complementary set of sensors detect deficiency and regulate genes encoding proteins that acquire more of the required ions (Hantke 2001; Busenlehner, Pennella et al. 2003). It is currently poorly understood how such metal-sensing metalloregulators accurately discriminate between various metal ions.

Arsenic is a well-known poison and anti-microbial agent. Excess concentrations of this and other metalloids (or metals) are toxic to many living organisms. To cope with exposure to these metal(loid)s, nature has developed a set of P-type ATPase efflux pumps and metal-sequestering proteins that effectively remove the metal(loid)s from the cytosol (Xu, Zhou et al. 1998). Expression of the pumps and sequestering proteins is controlled by metal-responsive regulatory proteins. In the absence of metal(loid), the ArsR-type regulators bind the operator/promoter (O/P) region of the relevant metal homeostasis operon, repressing

transcription. As the concentration of metal(loid) increases, the metal(loid)-binding site of the metalloregulator becomes occupied, creating a conformational change of the regulator which causes it to release the O/P DNA, allowing expression of the operon. Related metalloregulatory systems are also involved in metal homeostasis of essential metals (e.g., Zn).

Several members of the ArsR/SmtB family have been identified, including: Cd(II),Pb(II),Bi(III)-responsive CadC (Rensing, Sun et al. 1998; Sun, Wong et al. 2001), Zn(II)-responsive SmtB (Huckle, Morby et al. 1993), Zn(II)-responsive ZiaR (Thelwell, Robinson et al. 1998) Co(II),Zn(II)-responsive CzrA (Kuroda, Hayashi et al. 1999; Singh, Xiong et al. 1999), Ni(II),Co(II)-responsive NmtR (Cavet, Meng et al. 2002), and the prototypical member, ArsR (Xu, Zhou et al. 1998). The groups of our collaborators, D. P. Giedroc (Texas A&M University) and N. J. Robinson (University of Newcastle) have contributed much to the molecular level understanding of metalloregulation in this family. During the past several years, they have accumulated a great deal of evidence in support of a hypothesis that individual members of the ArsR/SmtB family are characterized by essentially two types of metal binding sites, designated α5 and α3N, that play distinct roles in regulation and metal selectivity, depending on the system (Pennella, Arunkumar et al. 2006). A sequence comparison for proteins discussed herein is shown in Figure 5.1 and highlights these sites.

In particular, searches of the *Mycobacterium tuberculosis* genome sequence have revealed a gene encoding NmtR, an SmtB-like protein. The association of NmtR with NmtA, a P-type ATPase, suggested its role as a metalloregulator. *In vivo* and *in vitro* experiments have been performed in which NmtR is identified as a Ni-responsive metalloregulator. In a series of clever experiments, Giedroc and Robinson have demonstrated that although NmtR binds Zn more tightly than Ni, Zn-responsive SmtB binds Zn more tightly than NmtR (Cavet, Meng et al.

2002). *In vitro* experiments indicate that NmtR *is* Zn-responsive, however *in vivo* experiments, in which both SmtB and NmtR are available in the cellular environment, demonstrate that NmtR does not respond to Zn, presumably because SmtB ensures that there is essentially no free Zn present. Thus, nature's method for metalloregulation has resulted in a system where each metalloregulator has *both* an absolute binding preference for its relevant metal *and* a comparative advantage over other regulators for that metal. Rather, it is only necessary for the latter characteristic to be true. In effect, one can imagine that Zn-responsive regulators first ensure that there is no free Zn in the cell. Next, free Ni, Co, Cu, etc., are sequentially sequestered by the appropriate regulators. This hypothesis provides an interesting framework upon which to base structural characterizations of the metal binding sites.

Here our group reports insights gained from the XAS study of two additional family members, *Staphylococcus aureus* CzrA and *Mycobacterium tuberculosis* NmtR. CzrA and NmtR share 30% sequence identity and a high degree of similarity (60%) yet respond to distinct but partially overlapping metal profiles *in vivo*. *S. aureus* CzrA is a Co(II)/Zn(II)-specific sensor that regulates the expression of the *czr* operon, which encodes a Co(II)/Zn(II)-facilitated pump, CzrB, that effluxes metal out of the cell (Kuroda, Hayashi et al. 1999; Singh, Xiong et al. 1999). Electromobility-shift assays and *in vivo* expression studies perfomed by Giedroc's group indicate that Zn(II) is the strongest inducer of CzrA regulation, with Co(II) also capable of regulation but only at higher concentrations than Zn(II). Other metals, including Ni(II), have little to no effect on derepression of the *czr* operon (Kuroda, Hayashi et al. 1999; Singh, Xiong et al. 1999). The situation is precisely opposite for *M. tuberculosis* NmtR, with Ni(II) the strongest inducer of NmtR-dependent regulation of the *nmt* operon, which encodes a P-type ATPase metal efflux pump, NmtA (Cavet, Meng et al. 2002). Co(II) is an intermediate inducer, whereas Zn(II) has no

effect *in vivo* on derepression (Cavet, Meng et al. 2002). XAS results have been obtained for Ni(II), Zn(II), and Co(II) bound forms of NmtR and CzrA. XAS experiments demonstrate that both regulators bind Ni(II) in a hexadentate fashion, whereas Zn(II) (and Co(II)) CzrA is bound in a tetradentate environment. The Co(II) NmtR exhibits a unique split shell, hexadentate environment. These results provide insight into the mechanism for metal(loid) discrimination in metalloregulators.

Materials and Methods

Sample Preparation (performed by David P. Geidroc's group at Texas A&M University). The growth, expression, and purification of NmtR and CzrA were carried out using the procedure described previously for SmtB (VanZile, Cosper et al. 2000), except that DTT was excluded from the purification because CzrA and NmtR do not contain cysteine residues. After purification, purified CzrA or NmtR were dialyzed against 6 L of Buffer S (10 mM HEPES, 0.1 M NaCl, pH 7.0) with changes every 4 h for a total of 24 h at 4 °C. N-terminal sequencing of CzrA and NmtR (5 cycles) revealed that both proteins do not possess the expected N-terminal methionine residue.

X-ray Absorption Spectroscopy. Ni, Zn, and Co XAS data were collected at 10 K on NmtR and CzrA samples of 1.0-1.6 mM metal at Stanford Synchrotron Radiation Laboratory, beamline 9-3, with the SPEAR storage ring operating at 3.0 GeV. The beamline used focusing optics and a fully tuned monochromator containing a Si[220] crystal. A 30-element Ge solid-state X-ray fluorescence detector was employed for data collection and utilized Soller slits and a Z–1 fluorescence filter for background rejection. All data collection parameters were as described previously (VanZile, Cosper et al. 2000). EXAFS analysis was performed with EXAFSPAK software (www-ssrl.slac.stanford.edu/exafspak.html) according to standard procedures (Scott

1985). Multiple scattering models, calculated using FEFF version 8.2 (Ankudinov, Ravel et al. 1998; Poiarkova and Rehr 1999), were based on bis(acetato)-bis(imidazole)zinc(II) (Horrocks, Ishley et al. 1980), tetrakis(imidazole)zinc(II) (Bear, Duggen et al. 1975), hexakis(imidazole)nickel(II) chloride tetrahydrate (Konopelski, Reimann et al. 1976), tetrakis(2-methylimidazol-3-yl)cobalt(II) bis(cyanamidonitrate) (Hvastijova, Boca et al. 2003), bis(acetato)-bis(imidazole)cobalt(II) (Gadet 1974), as described (Yamaguchi, Cosper et al. 1999). The carboxylate ligand used in best fits for M(II)-NmtR and M(II)-CzrA (M = Zn or Co) displays a M-O-C angle of 108° and a coplanar M-O-C-O unit.

Results

Comparison of the extended x-ray absorption fine structure (EXAFS) and Fourier transforms (FTs) for Ni(II)-, Zn(II)- or Co(II)- bound forms of NmtR, CzrA, and SmtB [the last published previously (VanZile, Cosper et al. 2000) and reproduced here for comparison] reveals a distinction between the metal binding sites of SmtB and those of NmtR and CzrA (Figures 5.2, 5.3, 5.4). Noticeable differences in the EXAFS arise in the region near $k \approx 4$ Å^{-1}. This region is sensitive to variations in high-frequency oscillations that are commonly associated with the multiple-scattering contribution from the outer-shell atoms of the imidazole ring of histidine. An increase in the number of histidine ligands causes splitting of the main peak in this region, also visualized as increased intensity in the high-R region of the FT plot, specifically at ca. 3 and 4 Å, which is diagnostic for histidine ligation. The absence of a 3 Å peak, in the presence of a 4 Å peak in the FT, has been assigned previously as the result of destructive interference between the outer-shell contributions from carboxylate and histidine ligands (Ankudinov, Ravel et al. 1998; VanZile, Cosper et al. 2000). This is most clearly observed in the Zn FTs (Figures 5.3B) and supports the binding of a carboxylate-containing residue to each metal (Co-CzrA also follows

this trend; Figure 5.4B). In addition, the Zn(II) and Co(II) CzrA EXAFS (inset Figures 5.3B and 5.4B) are consistent with an increase in imidazole ligation in NmtR and CzrA, relative to SmtB. Another key difference between SmtB and NmtR/CzrA is the ~2.3-Å shoulder in the main FT peak that appears in Zn(II) and Co(II) SmtB (Figures 5.3B and 5.4B). This shoulder arises from the contribution of a first-shell sulfur ligand contributed by cysteine only in SmtB (VanZile, Cosper et al. 2000).

The results of extensive curve-fitting analysis of these samples are consistent with the observation that NmtR and CzrA have increased contribution from imidazole containing ligands and no contribution from sulfur-containing ligands, consistent with the fact that neither CzrA nor NmtR have cysteine residues (Figure 5.1). Best fits for both Ni(II) NmtR (Fit 6, Table 5.1) and Ni(II) CzrA (Fit 13, Table 5.1) indicate a coordination environment containing three histidine ligands and three other oxygen- or nitrogen-containing ligands. The ca. octahedral Ni(II) environment is also supported by the very low intensity of the 1s-3d transition in the pre-edge region (Figure 5.2A). Similarly, Zn(II) NmtR and Zn(II) CzrA are best fit with three histidine ligands (a conclusion recently strengthened by NMR data (Pennella, Arunkumar et al. 2006)), although in striking contrast to the Ni(II) complexes, the coordination geometry of the Zn(II)-binding site is most likely tetrahedral rather than octahedral (Fits 7, 14; Table 5.2). This would be consistent with the tetrahedral coordination geometry associated with the Co(II) complex of CzrA (Fit 15, Table 5.3), but in contrast to Co(II) NmtR (Fit 8, Table 5.3), which clearly adopts a higher coordination number than the Zn(II) NmtR. Furthermore, Co(II) NmtR adopts a unique hexadentate coordination sphere, different from Ni(II) NmtR.

XAS studies involving Co(II) bound CzrA suggest a tetrahedral Asp-His_3 ligand set for the site (Figure 5.4B), highly similar to the characterized Zn(II) sites. This structural information

implies that CzrA requires a tetrahedral site to regulate DNA binding negatively with Co(II) and Zn(II). In contrast, Co(II) NmtR exhibits XAS data consistent with a five- or six-coordinate site that has two first-shell peaks at ca. 1.9 and 2.1 Å consisting mainly of weak scattering atoms (N/O) (Figure 5.4B). Detailed curve-fitting analysis of Co(II) NmtR suggests a best fit of two imidazole ligands, one in each first shell and both in combination with two additional N/O ligands (Fit 8, Table 5.3). Both Co(II) substituted samples are in agreement with electronic absorption spectra suggesting a four-coordinate species for Co(II) CzrA and a five- or six-coordinate site for Co(II) NmtR (Pennella, Shokes et al. 2003; Pennella, Arunkumar et al. 2006).

XAS results for Ni(II), Zn(II), and Co(II) bound forms of NmtR demonstrate that NmtR binds Ni(II) and Co(II) in a hexadentate fashion, whereas Zn(II) is bound in a tetradentate environment. These results provide insight into the mechanism for metal discrimination in metalloregulators. Sequence alignments have revealed two amino acid residues, His109 and His116 that are present in NmtR, but not in SmtB (Figure 5.1). Mutation of these residues results in inducer non-responsive repressors. Thus, in NmtR there appear to be additional metal-binding residues available that allow NmtR to form hexadentate complexes while SmtB prefers to form tetradentate complexes. These data provide a framework for understanding metal selectivity.

Discussion

The SmtB/ArsR family of metalloregulators is uniquely characterized by the presence of two metal-binding sites, neither of which is absolutely conserved across the family (Busenlehner, Pennella et al. 2003; Pennella, Arunkumar et al. 2006). Some SmtB/ArsR members possess only the α3N site, others just the α5 site, while some, including cyanobacterial zinc sensors SmtB and ZiaR, appear to possess both. Recent work from our and our collaborators' laboratories has helped define the coordination environments of the α3N and α5 metal-binding sites of SmtB

(VanZile, Cosper et al. 2000; VanZile, Chen et al. 2002; VanZile, Chen et al. 2002). These studies reveal that the histidine/carboxylate-containing α5 site is responsible for binding Zn(II) in a tetrahedral coordination complex and allosterically regulating binding of SmtB to the *smt* operon. The α3N site, which contains at least one cysteine thiolate ligand (Cys14), not present in CzrA or NmtR (VanZile, Chen et al. 2002) (*cf.* Figure 5.1), plays some other role. These findings are fully compatible with characterization of mutant SmtBs *in vivo* (Turner, Glands et al. 1996). The α3N metal site possesses a higher affinity for Zn(II) in the free protein at equilibrium; this is the Zn(II) complex characterized in previous EXAFS studies and reproduced here for comparison (Figure 5.3) (VanZile, Cosper et al. 2000).

The protein determinants of metal ion specificity are not currently well defined. An attractive hypothesis is that proteins simply follow the trends predicted by traditional inorganic chemistry. Unfortunately, those trends have not provided a complete explanation for why certain metal ions are preferred by certain proteins. Sometimes the metal ion that binds with the highest affinity to the protein is not the metal ion that provides *in vivo* functionality, complicating the study of metal ion specificity (Cavet, Meng et al. 2002). Our results provide a basis for bridging the gap between inorganic and biological chemistry that can be applied to the understanding of nature's selection process.

SmtB and CzrA which favor Zn(II) coordination at the α5 site, utilize carboxylate and imidazole ligands to bind harder Lewis acids, such as Co(II), Ni(II), and Zn(II). NmtR, which discriminates toward Ni(II) and Co(II), also uses imidazoles. CadC and ArsR possess α3N and α3 metal sites that have all-cysteinyl coordination spheres that prefer softer Lewis acids, such as Cd(II), Pb(II), and Bi(III) (Busenlehner, Cosper et al. 2001; Busenlehner, Apuy et al. 2002; Busenlehner, Weng et al. 2002). Interestingly, *S. aureus* pI258 CadC contains an intact α5 metal

site that has been shown to bind Zn(II) and Co(II) directly; however, the binding of metal here is not regulatory for DNA binding *in vitro* (Busenlehner, Weng et al. 2002) or *in vivo* (Wong, Lin et al. 2002).

Here, we provide spectroscopic evidence for the coordination environment of the metalloregulatory sites of *S. aureus* CzrA and *M. tuberculosis* NmtR in an attempt to determine how these proteins functionally discriminate between different transition metals. The spectroscopic properties of both CzrA and NmtR lend support to the model in which ligands located in the α5 site of the proteins contribute to binding Co(II), Ni(II), or Zn(II) (Figure 5.1). XAS data for Zn(II) CzrA, Zn(II) NmtR, and Co(II) CzrA are consistent with a tetrahedral coordination model that utilizes three histidines and one carboxylate-containing residue to ligate the metal ion. By contrast, XAS data for Ni(II) NmtR and Ni(II) CzrA indicate a six-coordinate environment containing at least three histidine ligands and three other oxygen- or nitrogen-containing ligands (Co(II) also binds to NmtR in a hexadentate fashion).

In addition, Giedroc's studies with SmtB made the prediction that CzrA would only contain a metal site between the α5 helices, since it lacks the N-terminal "arm" (Figure 5.1). In collaboration with Drs. Sacchettini and Eicken, Giedroc has obtained a 2.2 Å resolution crystal structure of the homodimeric Zn_2-CzrA. They find that two symmetry-related tetrahedral Asp-His_3 Zn(II) sites bridge the dimer, exactly as predicted. This structural information implies that CzrA requires a tetrahedral site to negatively regulate DNA binding with Co(II) and Zn(II). Co XAS data of a CzrA/NmtR hybrid protein reveals highly similar patterns to data for Co(II) CzrA (XAS data not shown) also suggesting a tetrahedral Co(II)-Asp-His_3 coordination site (Fit 22, Table 5.3). Proposed XAS experiments of H86Q and H86C mutants should provide more

detailed information on the structure of the chelates in each case, and help us further understand the effect of the protein environment on metal binding specificity and metal responsiveness.

Acknowledgments

The XAS data were collected at SSRL, which is operated by the Department of Energy, Division of Chemical Sciences. The SSRL Biotechnology program is supported by the National Institutes of Health, Biomedical Resource Technology Program, Division of Research Resources. We thank Dr. Larry Dangott in the Protein Chemistry Laboratory at Texas A&M University for his determination of the N-terminal sequences of CzrA and NmtR. These studies were supported in part by the National Institutes of Health (GM42569 to D. P. G. and GM42025 to R. A .S.) and the Robert A. Welch Foundation (A-1295 to D. P. G). M. A. P. was supported in part by an NIH Chemistry-Biology Interface Training Grant (T32 GM 08523).

References

Ankudinov, A. L., B. Ravel, et al. (1998). "Real-space multiple-scattering calculation and interpretation of x-ray-absorption near-edge structure." Physical Review B **58**(12): 7565-7576.

Bear, C. A., K. A. Duggen, et al. (1975). Acta Crystallogr. Sec. B **31**: 2713.

Busenlehner, L. S., J. L. Apuy, et al. (2002). "Characterization of a metalloregulatory bismuth(III) site in Staphylococcus aureus pI258 CadC repressor." J Biol Inorg Chem **7**(4-5): 551-9.

Busenlehner, L. S., N. J. Cosper, et al. (2001). "Spectroscopic properties of the metalloregulatory Cd(II) and Pb(II) sites of S. aureus pI258 CadC." Biochemistry **40**(14): 4426-36.

Busenlehner, L. S., M. A. Pennella, et al. (2003). "The SmtB/ArsR family of metalloregulatory transcriptional repressors: Structural insights into prokaryotic metal resistance." FEMS Microbiol Rev **27**(2-3): 131-43.

Busenlehner, L. S., T. C. Weng, et al. (2002). "Elucidation of primary (alpha(3)N) and vestigial (alpha(5)) heavy metal-binding sites in Staphylococcus aureus pI258 CadC: evolutionary implications for metal ion selectivity of ArsR/SmtB metal sensor proteins." J Mol Biol **319**(3): 685-701.

Cavet, J. S., W. Meng, et al. (2002). "A Nickel-Cobalt-sensing ArsR-SmtB Family Repressor. CONTRIBUTIONS OF CYTOSOL AND EFFECTOR BINDING SITES TO METAL SELECTIVITY." J Biol Chem **277**(41): 38441-8.

Cook, W. J., S. R. Kar, et al. (1998). "Crystal structure of the cyanobacterial metallothionein repressor SmtB: a model for metalloregulatory proteins." J Mol Biol **275**(2): 337-46.

Gadet, A. (1974). "Crystalline Structure of Cobalt Compounds Cobalt (Imidazole)2 (Acetate)2." Acta Crystallographica Section B-Structural Science **B 30**(FEB15): 349-353.

Hantke, K. (2001). "Iron and metal regulation in bacteria." Curr Opin Microbiol **4**(2): 172-7.

Horrocks, W. D., Jr., J. N. Ishley, et al. (1980). "Structural and electronic mimics of the active site of cobalt(II)-substituted zinc metalloenzymes." J Inorg Biochem **12**(2): 131-41.

Huckle, J. W., A. P. Morby, et al. (1993). "Isolation of a prokaryotic metallothionein locus and analysis of transcriptional control by trace metal ions." Mol Microbiol **7**(2): 177-87.

Hvastijova, M., R. Boca, et al. (2003). "Cyanamidonitrate-cobalt(II) complexes of pyrazole and imidazole ligands. X-ray structure of [Co(NO2NCN)(2)(pyrazole)(4)] and [Co(2-methylimidazole)(4)](NO2NCN)(2)." Inorganica Chimica Acta **343**: 217-223.

Konopelski, J. P., C. W. Reimann, et al. (1976). Acta Crystallogr. Sec. B **32**: 2911-2913.

Kuroda, M., H. Hayashi, et al. (1999). "Chromosome-determined zinc-responsible operon czr in Staphylococcus aureus strain 912." Microbiol Immunol **43**(2): 115-25.

O'Halloran, T. V. (1993). "Transition metals in control of gene expression." Science **261**(5122): 715-25.

Pennella, M. A., A. I. Arunkumar, et al. (2006). "Individual metal ligands play distinct functional roles in the zinc sensor Staphylococcus aureus CzrA." J Mol Biol **356**(5): 1124-36.

Pennella, M. A., J. E. Shokes, et al. (2003). "Structural elements of metal selectivity in metal sensor proteins." Proc Natl Acad Sci U S A **100**(7): 3713-8.

Poiarkova, A. V. and J. J. Rehr (1999). "Multiple-scattering x-ray absorption fine-structure Debye-Waller factor calculations." Phys. Rev. B **59**(2): 948-957.

Rensing, C., Y. Sun, et al. (1998). "Pb(II)-translocating P-type ATPases." J Biol Chem **273**(49): 32614-7.

Rosenzweig, A. C. (2002). "Metallochaperones: bind and deliver." Chem Biol **9**(6): 673-7.

Scott, R. A. (1985). "Measurement of metal-ligand distances by EXAFS." Methods Enzymol. **117**: 414-459.

Singh, V. K., A. Xiong, et al. (1999). "ZntR is an autoregulatory protein and negatively regulates the chromosomal zinc resistance operon znt of Staphylococcus aureus." Mol Microbiol **33**(1): 200-7.

Sun, Y., M. D. Wong, et al. (2001). "Role of cysteinyl residues in sensing Pb(II), Cd(II), and Zn(II) by the plasmid pI258 CadC repressor." J Biol Chem **276**(18): 14955-60.

Thelwell, C., N. J. Robinson, et al. (1998). "An SmtB-like repressor from Synechocystis PCC 6803 regulates a zinc exporter." Proc Natl Acad Sci U S A **95**(18): 10728-33.

Turner, J. S., P. D. Glands, et al. (1996). "Zn2+-sensing by the cyanobacterial metallothionein repressor SmtB: different motifs mediate metal-induced protein-DNA dissociation." Nucleic Acids Res **24**(19): 3714-21.

VanZile, M. L., X. Chen, et al. (2002). "Allosteric negative regulation of smt O/P binding of the zinc sensor, SmtB, by metal ions: a coupled equilibrium analysis." Biochemistry **41**(31): 9776-86.

VanZile, M. L., X. Chen, et al. (2002). "Structural characterization of distinct alpha3N and alpha5 metal sites in the cyanobacterial zinc sensor SmtB." Biochemistry **41**(31): 9765-75.

VanZile, M. L., N. J. Cosper, et al. (2000). "The zinc metalloregulatory protein Synechococcus PCC7942 SmtB binds a single zinc ion per monomer with high affinity in a tetrahedral coordination geometry." Biochemistry **39**(38): 11818-29.

Wong, M. D., Y. F. Lin, et al. (2002). "The soft metal ion binding sites in the Staphylococcus aureus pI258 CadC Cd(II)/Pb(II)/Zn(II)-responsive repressor are formed between subunits of the homodimer." J Biol Chem **277**(43): 40930-6.

Xu, C., T. Zhou, et al. (1998). "Metalloid resistance mechanisms in prokaryotes." J Biochem (Tokyo) **123**(1): 16-23.

Yamaguchi, K., N. J. Cosper, et al. (1999). "Characterization of metal-substituted Klebsiella aerogenes urease." J Biol Inorg Chem **4**(4): 468-77.

Figure Legends

Figure 5.1. A multiple sequence alignment of *Synechococcus* PCC 7942 SmtB (P30340), *S. aureus* CzrA (O85142), and *M. tuberculosis* NmtR (NP_218262.1) (Pennella, Shokes et al. 2003). Residues that are identical (*****), residues that are strongly similar (:), and residues that are weakly similar (.) are denoted below the alignment. Secondary structure elements are denoted above the alignment and are based on the crystal structure of apo-SmtB (Cook, Kar et al. 1998) and chemical-shift indexing for CzrA (Busenlehner, Pennella et al. 2003). Conserved metal-binding residues located in the α5 site are boxed, as are proposed ligands to the α3N site in SmtB (C14, H18, C61, D64) (VanZile, Chen et al. 2002; VanZile, Chen et al. 2002).

Figure 5.2. Ni K-edge X-ray absorption spectrum (a) and Fourier transforms (k = 2 – 12 Å^{-1}; k^3 weighting) (b) of the EXAFS (inset of b) for Ni(II)-NmtR (solid), Ni(II)-CzrA (dotted), and Ni(II)-SmtB ((VanZile, Cosper et al. 2000); dashed).

Figure 5.3. Zn K-edge X-ray absorption spectrum (a) and Fourier transforms (k = 2 – 12 Å^{-1}; k^3 weighting) (b) of the EXAFS (inset of b) for Zn(II)-NmtR (solid), Zn(II)-CzrA (dotted), and Zn(II)-SmtB ((VanZile, Cosper et al. 2000); dashed).

Figure 5.4. Co K-edge X-ray absorption spectrum (a) and Fourier transforms (k = 2 – 12 Å^{-1}; k^3 weighting) (b) of the EXAFS (inset of b) for Co(II)-NmtR (solid), Co(II)-CzrA (dotted), and Co(II)-SmtB ((VanZile, Cosper et al. 2000); dashed).

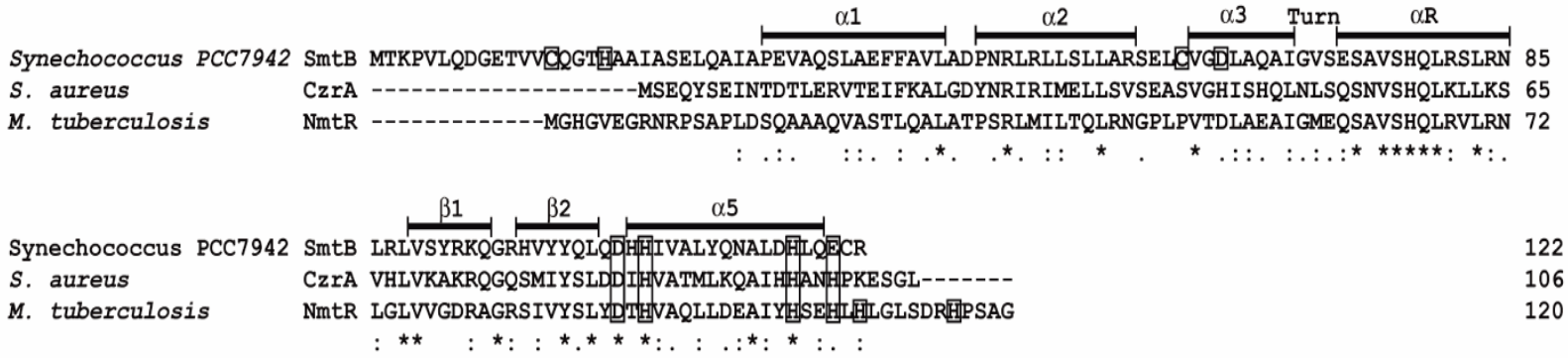
α1
α2
α3
Turn
αR
Synechococcus PCC7942 SmtB MTKPVLQDGETVVQQGTHAAIASELQAIAPEVAQSLAEFFAVLADPNRLRLLSLLARSELCVGDLAQAIGVSESAVSHQLRSLRN 85
S. aureus CzrA ----------MSEQYSEINTDTLERVTEIFKALGDYNRIRIMELLSVSEASVGHISHQLNLSQSNVSHQLKLLKS 65
M. tuberculosis NmtR ----------MGHGVEGRNRPSAPLDSQAAAQVASTLQALATPSRLMILTQLRNGPLPVTDLAEAIGMEQSAVSHQLRVLRN 72
β1
β2
α5
Synechococcus PCC7942 SmtB LRLVSYRKQGRHVYYQLQDHHIVALYQNALDHLQECR 122
S. aureus CzrA VHLVKAKRQGQSMIYSLDDIHVATMLKQAIHHANHPKESGL------- 106
M. tuberculosis NmtR LGLVVGDRAGRSIVYSLYDTHVAQLLDEAIYHSEHLHLGLSDRHPSAG 120

Figure 5.1

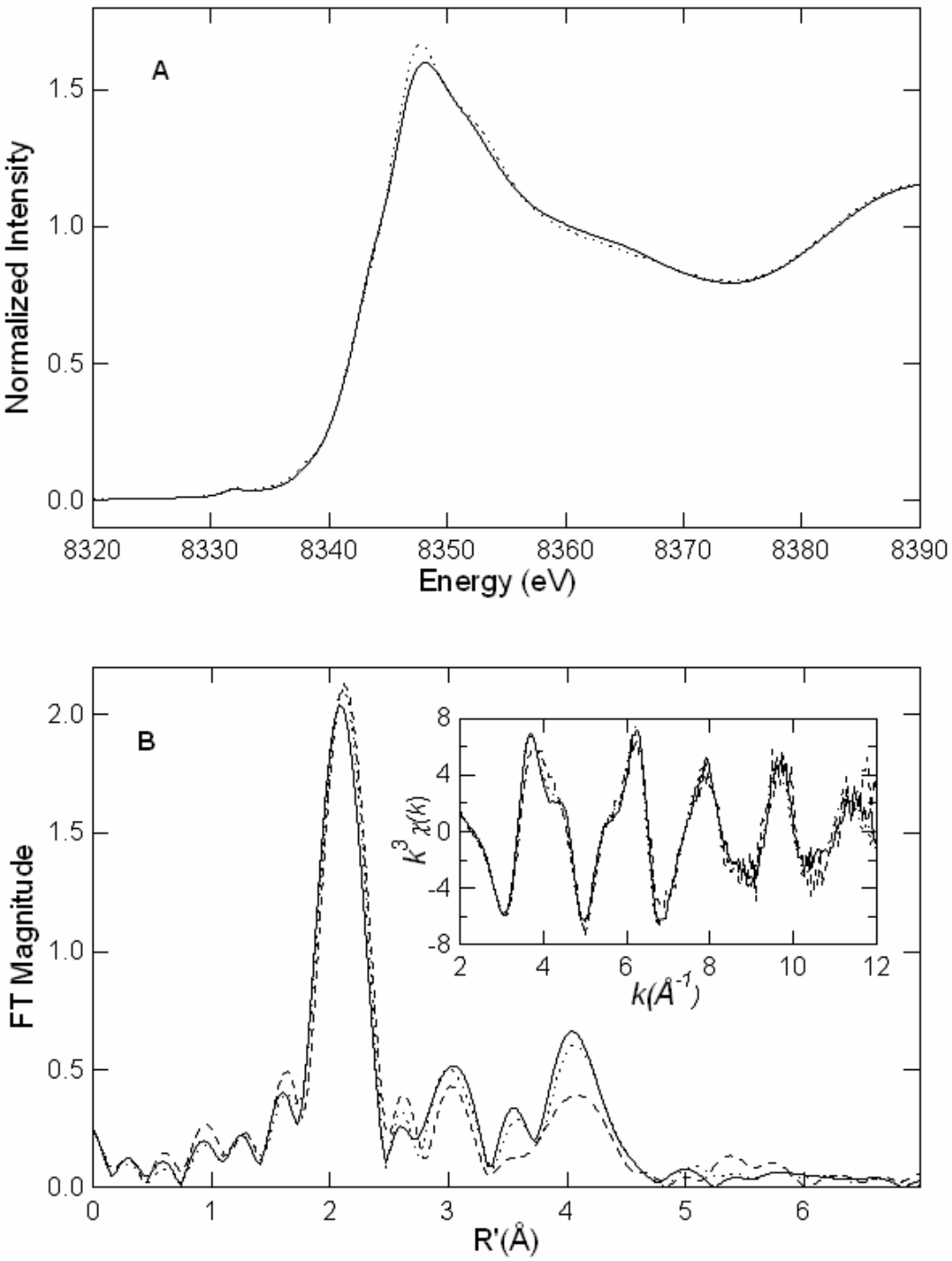
A
Normalized Intensity
Energy (eV)
B
FT Magnitude
R'(Å)
$k^3\chi(k)$
$k(Å^{-1})$

Figure 5.2

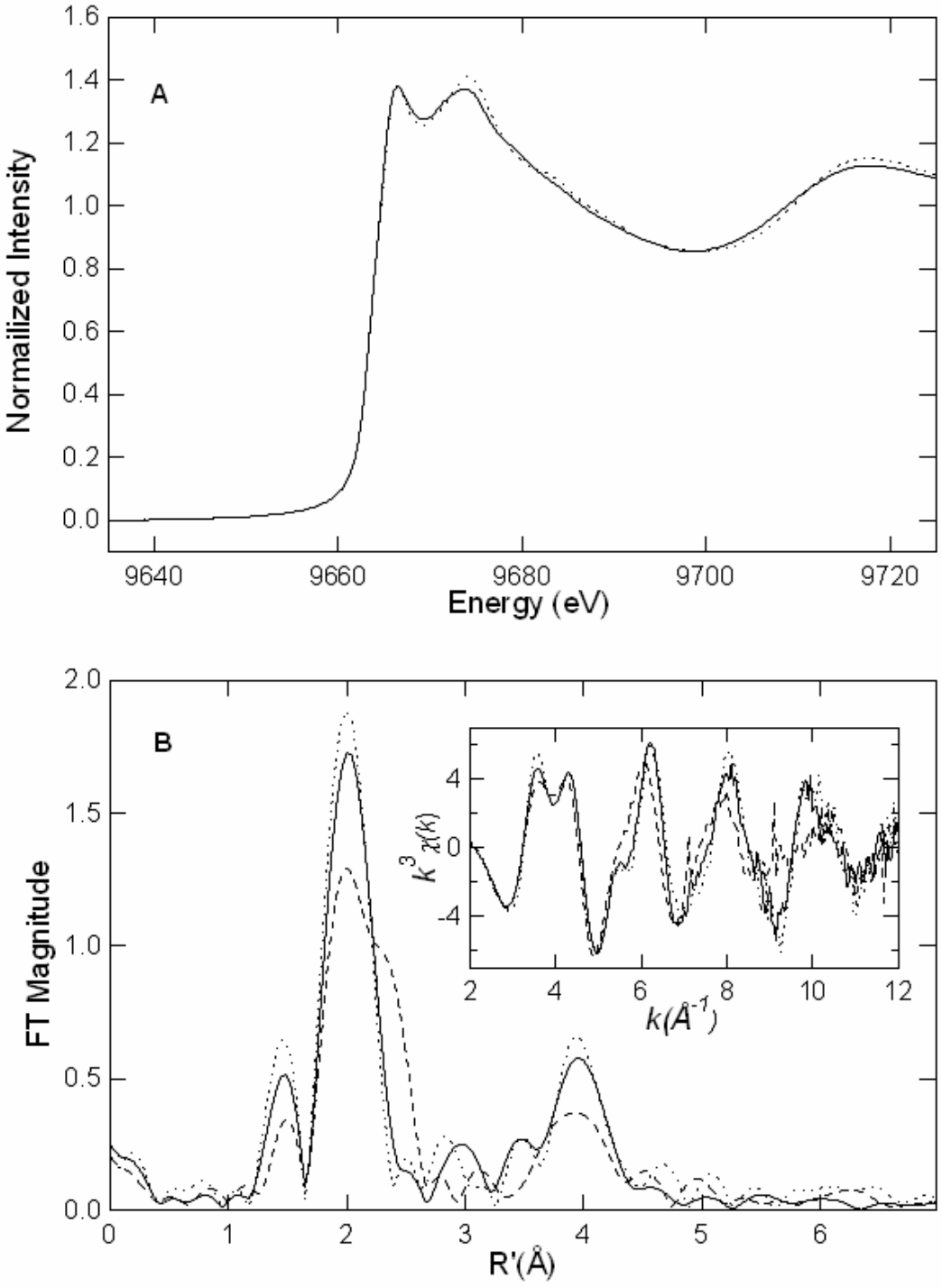
A
Normailized Intensity
Energy (eV)
B
FT Magnitude
R'(Å)
$k^3\chi(k)$
$k(Å^{-1})$

Figure 5.3

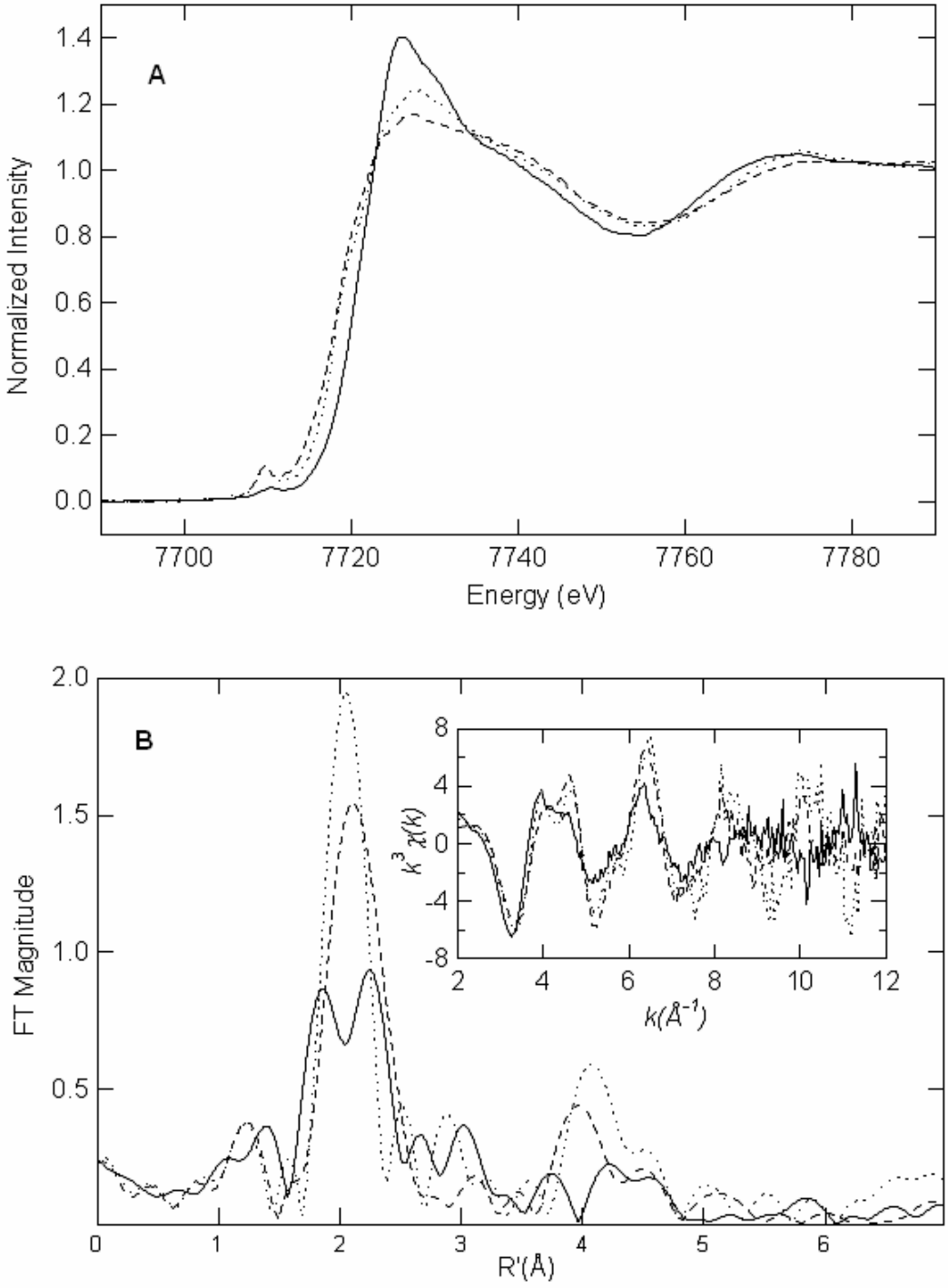
A
Normalized Intensity
Energy (eV)
B
FT Magnitude
R'(Å)
$k^3\chi(k)$
$k(Å^{-1})$

Figure 5.4

Table 5.1. Curve fitting results for Ni EXAFS[a]

Sample filename (k range) $\Delta k^3\chi$	Fit	Shell	R_{as} (Å)	σ_{as}^2 (Å^2)	ΔE_0 (eV)	f[b]	BVS[c]
NmtR	1	Ni-N_4	2.07	0.0018	–3.95	0.110	1.28
NNM0B (2-12 Å^{-1})	2	Ni-N_5	2.08	0.0030	–3.55	0.100	1.55
$\Delta k^3\chi$ = 13.89	3	Ni-N_6	2.08	0.0041	–3.63	0.095	1.86
	4	Ni-N_7	2.08	0.0051	–3.70	0.094	2.17
	5	Ni-N_6	2.08	0.0044	7.03	0.064	
		Ni-C_2	3.02	0.0001			
		Ni-C_2	[3.13]	[0.0001]			
		Ni-N_2	[4.17]	[0.0001]			
		Ni-C_2	[4.24]	[0.0001]			
	6	Ni-N_6	2.08	0.0045	7.20	0.061	
		Ni-C_3	3.02	0.0025			
		Ni-C_3	[3.13]	[0.0026]			
		Ni-N_3	[4.17]	[0.0035]			
		Ni-C_3	[4.24]	[0.0035]			
	7	Ni-N_6	2.08	0.0045	7.22	0.063	
		Ni-C_4	3.01	0.0051			
		Ni-C_4	[3.13]	[0.0053]			
		Ni-N_4	[4.16]	[0.0071]			

		Ni-C_4	[4.24]	[0.0072]			
CzrA	8	Ni-N_4	2.09	0.0015	–3.40	0.110	1.21
NCZ0A (2-12 Å^{-1})	9	Ni-N_5	2.09	0.0027	–3.06	0.098	1.51
$\Delta\, k^3\chi = 13.96$	10	Ni-N_6	2.09	0.0039	–3.17	0.091	1.81
	11	Ni-N_7	2.09	0.0050	–3.33	0.087	2.11
	12	Ni-N_6	2.09	0.0041	6.98	0.061	
		Ni-C_2	3.03	0.0006			
		Ni-C_2	[3.14]	[0.0006]			
		Ni-N_2	[4.18]	[0.0008]			
		Ni-C_2	[4.25]	[0.0008]			
	13	Ni-N_6	2.09	0.0042	7.09	0.061	
		Ni-C_3	3.02	0.0033			
		Ni-C_3	[3.14]	[0.0034]			
		Ni-N_3	[4.17]	[0.0045]			
		Ni-C_3	[4.25]	[0.0046]			
	14	Ni-N_6	2.09	0.0041	7.13	0.063	
		Ni-C_4	3.02	0.0062			
		Ni-C_4	[3.13]	[0.0064]			
		Ni-N_4	[4.16]	[0.0075]			
		Ni-C_4	[4.24]	[0.0087]			

[a] Shell is the chemical unit defined for the multiple scattering calculation. Subscripts denote the number of scatterers per metal. R_{as} is the metal-scatterer distance. σ_{as}^2 is a mean square deviation in R_{as}. ΔE_0 is the shift in E_0 for the theoretical scattering functions.

[b] f' is a normalized error (chi-squared):

$$f' = \frac{\left\{ \sum_i \left[k^3 \left(\chi_i^{obs} - \chi_i^{calc} \right) \right]^2 / N \right\}^{1/2}}{\left[\left(k^3 \chi^{obs} \right)_{max} - \left(k^3 \chi^{obs} \right)_{min} \right]}$$

[c] BVS=$\Sigma\exp[(r_o-r)/0.37]$, r_0(Ni(II)-N)=1.647 (Thorp, 1991)

[d] Numbers in square brackets were constrained to be either a multiple of the above value ($\Delta_{as}2$) or to maintain a constant difference from the above value (R_{as}, ΔE_0,).

Table 5.2. Curve fitting results for Zn EXAFS[a]

Sample filename (k range) $\Delta k^3\chi$	Fit	Shell	R_{as} (Å)	σ_{as}^2 (Å^2)	ΔE_0 (eV)	f[b]	BVS[c]
NmtR	1	Zn-N_4	2.00	0.0031	–6.49	0.112	2.18
ZNM0B (2-12 Å^{-1})	2	Zn-N_5	2.00	0.0045	–6.62	0.105	2.72
$\Delta k^3\chi$ = 11.85	3	Zn-N_6	2.00	0.0058	–6.73	0.102	3.28
	4	Zn-N_4	2.00	0.0032	3.24	0.081	
		Zn-C_2	2.98	0.0019			
		Zn-C_2	[3.05]	[0.0020]			
		Zn-N_2	[4.13]	[0.0027]			
		Zn-C_2	[4.18]	[0.0027]			
	5	Zn-N_4	2.00	0.0033	3.29	0.071	
		Zn-C_3	2.98	0.0040			
		Zn-C_3	[3.04]	[0.0046]			
		Zn-N_3	[4.13]	[0.0063]			
		Zn-C_3	[4.17]	[0.0064]			
	6	Zn-N_4	2.00	0.0033	3.27	0.081	
		Zn-C_4	2.98	0.0073			
		Zn-C_4	[3.04]	[0.0074]			
		Zn-N_4	[4.13]	[0.0101]			
		Zn-C_4	[4.17]	[0.0102]			

	7	Zn-O_1	1.99	0.0017	5.62	0.069	
		Zn-C_1	[2.78]	[0.0024]			
		Zn-O_1	[3.12]	[0.0027]			
		Zn-N_3	1.99	0.0041			
		Zn-C_3	2.96	0.0033			
		Zn-C_3	[3.03]	[0.0033]			
		Zn-N_3	[4.15]	[0.0046]			
		Zn-C_3	[4.16]	[0.0046]			
CzrA	8	Zn-N_4	1.97	0.0022	–9.77	0.119	2.36
ZCZ0A (2-12 Å^{-1})	9	Zn-N_5	1.98	0.0035	–8.27	0.112	2.88
$\Delta\, k^3\chi = 11.93$	10	Zn-N_6	1.98	0.0048	–7.94	0.111	3.45
	11	Zn-N_4	1.99	0.0023	3.04	0.099	
		Zn-C_2	2.97	0.0041			
		Zn-C_2	[3.04]	[0.0042]			
		Zn-N_2	[4.12]	[0.0057]			
		Zn-C_2	[4.16]	[0.0057]			
	12	Zn-N_4	1.99	0.0024	3.02	0.097	
		Zn-C_3	2.97	0.0077			
		Zn-C_3	[3.03]	[0.0078]			
		Zn-N_3	[4.11]	[0.0106]			

	$Zn-C_3$	[4.15]	[0.0107]		
13	$Zn-N_4$	1.99	0.0025	3.02	0.097
	$Zn-C_4$	2.96	0.0108		
	$Zn-C_4$	[3.03]	[0.0111]		
	$Zn-N_4$	[4.11]	[0.0150]		
	$Zn-C_4$	[4.15]	[0.0152]		
14	$Zn-O_1$	2.00	0.0005	5.49	0.083
	$Zn-C_1$	[2.79]	[0.0006]		
	$Zn-O_1$	[3.15]	[0.0007]		
	$Zn-N_3$	1.97	0.0024		
	$Zn-C_3$	2.96	0.0040		
	$Zn-C_3$	[3.02]	[0.0040]		
	$Zn-N_3$	[4.14]	[0.0055]		
	$Zn-C_3$	[4.15]	[0.0055]		

[a] Shell is the chemical unit defined for the multiple scattering calculation. Subscripts denote the number of scatterers per metal. R_{as} is the metal-scatterer distance. σ_{as}^2 is a mean square deviation in R_{as}. ΔE_0 is the shift in E_0 for the theoretical scattering functions.

[b] f' is a normalized error (chi-squared):

$$f' = \frac{\left\{ \sum_i \left[k^3 \left(\chi_i^{obs} - \chi_i^{calc} \right) \right]^2 / N \right\}^{1/2}}{\left[\left(k^3 \chi^{obs} \right)_{max} - \left(k^3 \chi^{obs} \right)_{min} \right]}$$

[c] BVS=$\Sigma\exp[(r_o-r)/0.37]$, r_0(Zn(II)-N)=1.776. (Thorp, 1991)

[d] Numbers in square brackets were constrained to be either a multiple of the above value ($\Delta_{as}2$) or to maintain a constant difference from the above value (R_{as}, ΔE_0,).

Table 5.3. Curve fitting results for Co EXAFS[a]

Sample filename (k range) $\Delta k^3\chi$	Fit	Shell	R_{as} (Å)	σ_{as}^2 (Å^2)	ΔE_0 (eV)	f[b]	BVS[c]
Co(II)-NmtR	1	Co-N_4	2.05	0.0129	0.61	0.119	
CNM0A (2-13Å^{-1})	2	Co-N_2	1.95	0.0024	–0.61	0.104	
$\Delta k^3\chi$ = 12.14		Co-N_2	2.12	0.0007			
	3	Co-N_2	1.93	0.0022	–1.09	0.098	
		Co-N_3	2.11	0.0032			
	4	Co-N_3	1.96	0.0052	–1.40	0.098	
		Co-N_2	2.13	0.0008			
	5	Co-N_3	1.94	0.0048	–1.69	0.095	
		Co-N_3	2.12	0.0030			
	6	Co-N_4	1.96	0.0076	–2.03	0.095	
		Co-N_2	2.14	0.0010			
	7	Co-N_2	1.91	0.0023	–1.46	0.095	
		Co-N_4	2.10	0.0055			
	8	Co-N_3	1.92	0.0039	10.08	0.080	
		Co-C_1	[2.87]	[0.0033]			
		Co-C_1	[2.98]	[0.0033]			
		Co-N_1	[4.01]	[0.0029]			
		Co-C_1	[4.08]	[0.0036]			

		Co-N_3	2.10	0.0025		
		Co-C_1	[3.02]	[0.0033]		
		Co-C_1	[3.14]	[0.0032]		
		Co-N_1	[4.16]	[0.0040]		
		Co-C_1	[4.23]	[0.0047]		
CzrA	9	Co-N_4	2.00	0.0023	–0.95	0.119
CCZ0B (2-12 Å^{-1})	10	Co-N_5	2.00	0.0036	–1.33	0.119
$\Delta\, k^3\chi = 12.76$	11	Co-N_6	1.99	0.0048	–1.76	0.124
	12	Co-N_4	2.00	0.0019	8.27	0.096
		Co-C_2	[2.97]	[0.0026]		
		Co-C_2	[3.06]	[0.0024]		
		Co-N_2	[4.16]	[0.0032]		
		Co-C_2	[4.14]	[0.0034]		
	13	Co-N_4	2.00	0.0022	8.53	0.101
		Co-C_3	[2.97]	[0.0030]		
		Co-C_3	[3.06]	[0.0027]		
		Co-N_3	[4.15]	[0.0037]		
		Co-C_3	[4.14]	[0.0040]		
	14	Co-N_4	2.00	0.0027	8.47	0.113
		Co-C_4	[2.97]	[0.0036]		

		Co-C_4	[3.06]	[0.0033]		
		Co-N_4	[4.16]	[0.0045]		
		Co-C_4	[4.14]	[0.0049]		
	15	Co-O_1	1.98	0.0001	10.41	0.098
		Co-C_1	[2.80]	[0.0001]		
		Co-O_1	[3.16]	[0.0001]		
		Co-N_3	1.99	0.0034		
		Co-C_3	[2.95]	[0.0050]		
		Co-C_3	[3.05]	[0.0052]		
		Co-N_3	[4.13]	[0.0071]		
		Co-C_3	[4.11]	[0.0070]		
CzrA/NmtR Hybrid	16	Co-N_4	2.00	0.0028	–1.79	0.108
CHZ0A (2-12 Å^{-1})	17	Co-N_5	2.00	0.0043	–2.08	0.109
$\Delta k^3\chi = 12.88$	18	Co-N_6	2.00	0.0057	–2.25	0.115
	19	Co-N_4	2.01	0.0029	7.90	0.094
		Co-C_2	[2.98]	[0.0039]		
		Co-C_2	[3.08]	[0.0036]		
		Co-N_2	[4.17]	[0.0048]		
		Co-C_2	[4.15]	[0.0052]		
	20	Co-N_4	2.00	0.0032	6.93	0.101

	$Co-C_3$	[2.97]	[0.0044]		
	$Co-C_3$	[3.06]	[0.0040]		
	$Co-N_3$	[4.15]	[0.0054]		
	$Co-C_3$	[4.14]	[0.0059]		
21	$Co-N_4$	1.99	0.0038	2.08	0.112
	$Co-C_4$	[2.96]	[0.0052]		
	$Co-C_4$	[3.06]	[0.0048]		
	$Co-N_4$	[4.16]	[0.0064]		
	$Co-C_4$	[4.13]	[0.0070]		
22	$Co-O_1$	2.00	0.0014	10.22	0.090
	$Co-C_1$	[2.83]	[0.0020]		
	$Co-O_1$	[3.20]	[0.0022]		
	$Co-N_3$	1.99	0.0039		
	$Co-C_3$	[2.90]	[0.0058]		
	$Co-C_3$	[3.05]	[0.0060]		
	$Co-N_3$	[4.14]	[0.0081]		
	$Co-C_3$	[4.12]	[0.0081]		

[a] Shell is the chemical unit defined for the multiple scattering calculation. Subscripts denote the number of scatterers per metal. R_{as} is the metal-scatterer distance. σ_{as}^2 is a mean square deviation in R_{as}. ΔE_0 is the shift in E_0 for the theoretical scattering functions.

[b] f' is a normalized error (chi-squared):

$$f' = \frac{\left\{ \sum_i \left[k^3 \left(\chi_i^{obs} - \chi_i^{calc} \right) \right]^2 / N \right\}^{1/2}}{\left[\left(k^3 \chi^{obs} \right)_{max} - \left(k^3 \chi^{obs} \right)_{min} \right]}$$

[c] $BVS = \Sigma \exp[(r_o - r)/0.37]$

[d] Numbers in square brackets were constrained to be either a multiple of the above value ($\Delta_{as}2$) or to maintain a constant difference from the above value (R_{as}, ΔE_0,).

CHAPTER 6

TRANSPROT AND REGULATION OF HEAVY METALS IN THE ENVIRONMENT

Introduction

High levels of toxic metals in polluted areas have evolved bacteria expressing genes with resistance mechanisms to toxic metals and metalloids. Not only do these genes have the ability to bind and transport heavy metals both intracellularly and across cell membranes, they have been shown to reduce toxic metals to a volatile or non-reactive state (Solioz and Vulpe 1996). Several resistance mechanisms exist among bacteria, including the efflux of metals out of the cell by membrane transporters, reduction of metals to less toxic species, and chelation of metals by cytoplasmic proteins. Integral to each mechanism is the regulation of gene expression by metalloregulatory proteins and their ability to tightly control the intracellular concentrations of heavy metals (Silver and Phung 1996; Nies 2003).

These bacteria express heavy metal resistance genes, including a family coding for CPx-type ATPases (a subgroup of P-type ATPases), that all share the defining CPx (x=C, H, S) and HMA motifs (Solioz and Vulpe 1996). The physiological role of the highly conserved cysteine, proline, cysteine/histidine/serine motif found near the C terminus is still under investigation; it has been postulated to take part in the transduction of heavy metals. The CPx-type ATPases are also classified by a putative heavy metal binding domain found near the N terminus of the protein. The GMTCXXC sequence motif (the so-called HMA motif) is deemed the framework necessary for proteins to bind metal ions. HMA motifs are common to Cd, Cu, and Zn resistance

CPx-type ATPases and are also found in other heavy metal resistance operons (e.g. *mer* operon) (Solioz and Vulpe 1996).

CadA is a CPx-type ATPase from *Listeria monocytogenes* and plays an important role in the efflux mechanism used for Cd(II) resistance (Lebrun, Audurier et al. 1994). Experiments by Lucia Banci and colleagues have demonstrated that CadA has the ability to transport both Cd(II) and Zn(II) (unpublished results from Dr. Banci's lab on CadA). Interestingly, the sequence homology of CadA with *Escherichia coli* ZntA (Zn(II) CPx-type ATPase) is high and structural comparisons of divalent cation transporters (e.g. CadA (Banci, Bertini et al. 2006) and ZntA (Banci, Bertini et al. 2002)) also suggest structural homology among HMA motifs and similar metal-binding sites (Banci, Bertini et al. 2006). Thus, to compare the binding ligands and coordination geometry of CPx-type ATPases, our lab has characterized the metal-binding site of Cd(II)-bound CadA from *L. monocytogenes* (constructed as an N-terminal fragment called NTKII) utilizing X-ray absorption spectroscopy (Banci, Bertini et al. 2006).

As stated above, the unique CXXC binding motif also exists in mercury resistance operons, found in certain prokaryotes. These genes make up an intricate detoxification system that is used to shuttle Hg(II) into the cell and reduce it to volatile Hg(0) (Brunker, Rother et al. 1996). The intracellular process is catalyzed by the mercuric reductase, MerA, which is dependent on NADPH for reduction (Sahlman, Lambeir et al. 1984). Reduction of organic mercury compounds (e.g. methylmercury) requires the presence of MerB, an organomercurial lyase, that catalyzes the cleavage of the carbon-mercury bond forming a reduced organic product and inorganic ionic mercury (the latter of which is further reduced by MerA to Hg(0)) (Benison, Di Lello et al. 2004). Elemental mercury then exits the cell by passive diffusion through the cell

membrane. Transcription of the *mer* operon is tightly controlled by the Hg(II)-responsive metallorgulatory protein MerR (Brunker, Rother et al. 1996).

Since the discovery of a detoxification system for Hg(II), scientist have begun to engineer methods for bioremediation of mercury in the environment. One technique involves the construction of transgenic plants that have the ability to sequester Hg(II) ions and reduce them to Hg(0), before removing it from the system (Bizily, Rugh et al. 2000). This reduction process is catalyzed by incorporating *mer*A and *mer*B genes into transgenic plants (Rugh, Wilde et al. 1996; Bizily, Rugh et al. 2000). Determination of the Hg coordination spheres in these proteins would provide a more detailed understanding of the mechanistic aspects of the Hg resistance, as well as suggest possible engineering methods for bioremediation strategies.

Studies have shown that MerB requires sulfhydryl-bound substrates and has the ability to reduce a large array of organic mercurial compounds. MerB also requires a thiol cofactor for reduction (Begley, Walts et al. 1986). A number of cofactors acceptable to MerB have been characterized, including cysteine, glutathione, and β-mercaptoethanol. In contrast, when dithiothreitol (DTT) was used as a cofactor, it was found to inhibit the reaction (Begley, Walts et al. 1986; Pitts and Summers 2002). To further investigate the ability of DTT to inhibit MerB, Dr. Omichinski's lab prepared a stable MerB complex consisting of MerB, one mercuric ion, and a molecule of DTT. Utilizing XAS, our lab has determined the metal-binding site of the complex to be most consistent with a HgS_3 model (Benison, Di Lello et al. 2004).

Positive and negative transcription of the *mer* operon is controlled by the Hg(II)-responsive metallorgulatory protein, MerR (Barkay, Miller et al. 2003). MerR activates transcription by binding to the operator *merO* in the presence of Hg(II) and preventing transcription when binding *merO* in the absence of Hg(II). Studies have revealed that MerR

consists of a N-terminal DNA binding domain, a C-terminal Hg(II) binding domain, and an interdomain region of unknown function (Song, Caguiat et al. 2004). In the MerR dimer, the C-terminal domain has been shown to bind Hg(II) via three cysteine residues (two from one monomer and one from the other) (Zeng, Stalhandske et al. 1998). To facilitate the study of MerR's metal-binding domain, Dr. Summer's lab constructed a single polypeptide consisting of two tandem direct repeats of α-helix 5 of Tn*21* MerR. In this 107-residue protein, the two α-helices are free to fold back upon each other to form an antiparallel coiled coil, thereby mimicking in a single chain the MerR binding domain ordinarily constituted by the interaction of two monomers. XAS experiments were employed to compare the Hg(II) binding site(s) of this small protein with those of wild-type MerR (Song, Caguiat et al. 2004).

Results and Discussion

Cd binding domain of the P1-type ATPase CadA. We used Cd XAS to provide information about the coordination sphere of cadmium in NTKII. Cd K edge, EXAFS, and Fourier transforms for NTKII either with or without tris(2-carboxyethyl)phosphine hydrochloride (TCEP) are displayed in Figure 6.1 and the results of curve-fitting of Cd EXAFS are provided in Table 6.1. Edge, EXAFS, and FTs are very similar for both NTKII samples. Cd K edges are quite broad owing to core hole lifetime broadening, but the edges in Figure 6.1A are indicative of Cd in a predominantly S environment. EXAFS and FTs also indicate the presence of a first shell of ligands at a distance (2.4–2.5 Å) that is expected for Cd–S bonds and curve-fitting results show that the first coordination sphere is dominated by S-containing ligands at ca 2.5 Å (Table 6.1). Compared in Table 6.1 are potential first-coordination spheres of CdS_xO_{4-x} (x = 4–2). The Cd–S Debye–Waller factor (σ_{as}^2) for CdS_4 fits is significantly larger than expected (0.0071 versus 0.0026 $Å^2$ for Cd-substituted rubredoxin (F. Bonomi, M. K. Eidsness & R.A.S, unpublished

observations) and the bond valence sum (BVS) parameter is significantly greater than the expected valence (2.30). Comparing CdS_3O_1 and CdS_2O_2 fits, Cd–S Debye–Waller factors are lower and BVS is closer to 2.00 for fits with three S-containing ligands.

As only two thiolate ligands are present in the sequence at Cys14 and Cys17 and CdNTKII forms a homodimeric complex containing one cadmium atom per monomer, we propose, on the basis of XAS, that the two cadmium ions share two thiolate ligands, one from each NTKII monomer, creating a dinuclear cluster (Figure 6.1A inset). In this model, the other Cys on each NTKII monomer is the third thiolate ligand. In agreement with this model, attempts to fit a Cd–Cd interaction converge for the TCEP sample only (cf. small FT peak in Figure 6.1B) with a Cd–Cd distance of ca 3.7 Å and a Debye–Waller factor of 0.0059 $Å^2$. The XAS data are also consistent with ^{113}Cd NMR data collected by Dr. Banci and colleagues (Banci, Bertini et al. 2006).

Cd(II) binding to NTKII induces protein dimerization in vitro with a Cd(II)/monomer stoichiometry of 1:1. XAS and NMR data suggest that the Cd(II) ions participate directly in dimerization as shown in the inset of Figure 6.1A (Banci, Bertini et al. 2006). This is favored by the coordination properties of Cd(II), which tends to prefer high coordination numbers, usually between four and six (Holm, Kennepohl et al. 1996). In particular, with increasing numbers of Cys thiolates as ligands, the coordination number of four becomes predominant (Cambridge Structural Database). Indeed, Cys-rich metalloproteins such as zinc and cadmium metallothioneins always bind these metal ions in a tetrahedral coordination environment (Henkel and Krebs 2004). Even if the homodimeric complex is not physiologically relevant, the dimerization should occur in vitro to better satisfy the coordination chemistry requirements of Cd(II) and the extensive solvent accessibility of the metal binding site makes this feasible. The

local structural environment of the Cd(II) ions, as characterized through Cd K edge X-ray absorption spectroscopy, supports that oxygen participates in the metal coordination sphere. Indeed, assuming four-coordinate Cd(II), a CdS_3O_1 first shell should be observed in a dinuclear cluster, whereas isolated monomeric Cd(II) sites would exhibit a CdS_2O_2 first shell (assuming a solvent (H_2O)-derived species as fourth ligand) and dimerization would have to occur by some undefined allosteric effect of Cd(II) binding. Our results (Table 6.1) suggest that either of these first coordination spheres is possible, although CdS_3O_1 exhibits more reasonable BVS values.

Another expected consequence of the proposed dinuclear site is the presence of a Cd–Cd FT peak. In the Cambridge Structural Database Cd–Cd distances for bis-thiolate bridged Cd(II) dinuclear clusters with predominant thiolate ligation range from 3.48 - 3.69 Å. The only possible reflection of such an interaction is the small FT peak (Figure 6.1B) at ~3.8 Å and this can be fitted with a 3.7 Å Cd–Cd distance in the TCEP-containing sample only. The Debye–Waller σ_{as}^2 value for the Cd–Cd shell in the fit of the TCEP-containing sample EXAFS data is 0.0059 $Å^2$, close to 0.0070 $Å^2$ reported for Cd–Cd in $[Cd_4(SPh)_{10}]^{2-}$ (Pickering, Prince et al. 1999), but the latter Cd–Cd distance is 4.3 Å and the bridging is different from that proposed here. Other Cd(II) dinuclear models display 3.8 Å - 3.9 Å Cd–Cd distances (Perez-Lourido, Romero et al. 1999), allowed by a less symmetrical bridging environment with one Cd bridging thiolate bond longer than the other (for each Cd(II)). This would imply a Cd(II) first-shell environment with significant static disorder in the Cd–S shell. Assuming that the Cd–S Debye–Waller factor for Cd-substituted rubredoxin (σ_{as}^2 = 0.0026 $Å^2$; other reported Cd-S σ_{as}^2 values are slightly higher, for example, σ_{as}^2 = 0.0031 $Å^2$ for $[Cd(SPh)_4]^{2-}$ (Pickering, Prince et al. 1999)) represents the vibrational component (four identical Cd–S bond lengths), we can use the observed Cd–S σ_{as}^2 (0.0054 $Å^2$) for NTKII samples to extract the contribution of static bond length disorder to the

Cd–S shell, yielding $\Delta R \approx 0.1$ Å (Banci, Bertini et al. 2006). This would represent the largest difference consistent with our data between the one long and two short Cd–S distances in a distorted dinuclear site and could result in a longer Cd–Cd distance depending on Cd–S–Cd angles. At longer Cd–Cd distances, the Debye–Waller factor would increase further and the Cd–Cd FT peak could easily become undetectable. It is also possible that the dynamics observed by NMR (Banci, Bertini et al. 2006) contain a component of dinuclear site dynamics that could contribute an additional vibrational Debye–Waller factor component to the Cd–Cd interaction. Thus, although the dinuclear structure proposed in the inset of Figure 6.1A is not required by the EXAFS data, it is definitely consistent with these data.

EXAFS Studies of the MerB/Hg/DTT Complex. To determine the geometry of ligands associated with Hg(II), EXAFS data were collected on the MerB/Hg/DTT complex. The EXAFS data of the MerB/Hg/DTT complex are most consistent with a coordination sphere for mercury consisting of three sulfur atoms (Table 6.2 and Figure 6.2). The measured Hg-S bond distance of 2.42 Å coincides with other mononuclear, mercuric-thiolate compounds that have a coordination number of three (Utschig, Wright et al. 1993). A search of the Cambridge Structural Database has confirmed that the Hg-S bond length is a sensitive indicator of coordination number: di-, tri-, and tetra-coordinate mononuclear mercuric-thiolate complexes have Hg-S bond lengths of 2.34 ± 0.02, 2.44 ± 0.04, and 2.54 ± 0.03 Å, respectively (Table 6.3). Also, although models with two, three, or four sulfurs all can provide good fits to the data, the Debye-Waller factor value (σ_{as}^2) for the HgS_3 case is the most physically reasonable one. In combination with the NMR data from Dr. Omichinski's lab, the EXAFS data are consistent with a model for the MerB/Hg/DTT complex in which two sulfurs from DTT and one sulfur from the protein bind to the mercuric ion (Benison, Di Lello et al. 2004).

It has been observed previously that DTT inhibits MerB (Begley, Walts et al. 1986; Pitts and Summers 2002), but the mechanism of the inhibition was not clearly understood. NMR experiments demonstrated that the inhibition by DTT is due to the formation of a stable MerB/Hg/DTT complex, preventing the release of the mercuric ion product. On the basis of XAS experiments, we conclude that the mercury in the MerB/Hg/DTT complex is bound in a coordination sphere consisting of three sulfur atoms and that two of the sulfur atoms originate from DTT. The third sulfur atom arises from a cysteine residue (predicted to be C96) of MerB (Benison, Di Lello et al. 2004).

XAS of Hg(II)-protein complexes. Previous XAS work with MerR (Zeng, Stalhandske et al. 1998) and deletion derivatives of it (Zeng, Stalhandske et al. 1998) revealed an unusual tricoordinate HgS_3 structure for the MerR-Hg binding center. Here we found that the XAS spectra of MBD and MerR indicated a very similar coordination of mercury in both proteins (Figure 6.3A), consistent with previous observations of MerR purified under denaturing conditions (Utschig, Wright et al. 1993; Zeng, Stalhandske et al. 1998) and of native His-tagged MerR (Utschig, Wright et al. 1993; Zeng, Stalhandske et al. 1998). The FTs (Figure 6.3B) of the EXAFS data (Figure 6.3B, inset) for both MerR and MBD indicated a single shell of scatterers at about 2.4 to 2.5 Å, consistent with the average Hg-S bond distance of 2.43 Å (range, 2.41 to 2.51 Å) in MerR, as measured previously (Utschig, Wright et al. 1993). The EXAFS curve-fitting results (Table 6.4) indicate that the average Hg-S bond length of MBD is slightly longer than that of MerR, although still within the range for three-coordinate Hg-S sites. (Average Hg-S bond lengths for two- and four-coordinate sites are 2.34 and 2.54 Å, respectively – Table 6.3.) However, the larger Debye-Waller factor (σ_{as}^2) for MBD suggests that the Hg(II)-binding site of MBD is more disordered than that of MerR, as also indicated by the relatively damped FT peak

intensity for MBD (Figure 6.3B). The XAS data establishes MerR and MBD has a highly similar Hg(II) coordination environments.

References

Banci, L., I. Bertini, et al. (2002). "A new zinc-protein coordination site in intracellular metal trafficking: solution structure of the Apo and Zn(II) forms of ZntA(46-118)." J Mol Biol **323**(5): 883-97.

Banci, L., I. Bertini, et al. (2006). "Structural basis for metal binding specificity: the N-terminal cadmium binding domain of the P1-type ATPase CadA." J Mol Biol **356**(3): 638-50.

Barkay, T., S. M. Miller, et al. (2003). "Bacterial mercury resistance from atoms to ecosystems." FEMS Microbiol Rev **27**(2-3): 355-84.

Begley, T. P., A. E. Walts, et al. (1986). "Mechanistic studies of a protonolytic organomercurial cleaving enzyme: bacterial organomercurial lyase." Biochemistry **25**(22): 7192-200.

Benison, G. C., P. Di Lello, et al. (2004). "A stable mercury-containing complex of the organomercurial lyase MerB: catalysis, product release, and direct transfer to MerA." Biochemistry **43**(26): 8333-45.

Bizily, S. P., C. L. Rugh, et al. (2000). "Phytodetoxification of hazardous organomercurials by genetically engineered plants." Nat Biotechnol **18**(2): 213-7.

Brunker, P., D. Rother, et al. (1996). "Regulation of the operon responsible for broad-spectrum mercury resistance in Streptomyces lividans 1326." Mol Gen Genet **251**(3): 307-15.

Henkel, G. and B. Krebs (2004). "Metallothioneins: zinc, cadmium, mercury, and copper thiolates and selenolates mimicking protein active site features--structural aspects and biological implications." Chem Rev **104**(2): 801-24.

Holm, R. H., P. Kennepohl, et al. (1996). "Structural and Functional Aspects of Metal Sites in Biology." Chem Rev **96**(7): 2239-2314.

Lebrun, M., A. Audurier, et al. (1994). "Plasmid-borne cadmium resistance genes in Listeria monocytogenes are similar to cadA and cadC of Staphylococcus aureus and are induced by cadmium." J Bacteriol **176**(10): 3040-8.

Nies, D. H. (2003). "Efflux-mediated heavy metal resistance in prokaryotes." FEMS Microbiol Rev **27**(2-3): 313-39.

Perez-Lourido, P., J. Romero, et al. (1999). "Synthesis and Characterization of Zinc and Cadmium Compounds with Arenephosphinothiol Ligands. Crystal and Molecular Structures of [Cd(2){2-(Ph(2)PO)C(6)H(4)S}(4)], [Zn{2-(Ph(2)P)-6-(Me(3)Si)C(6)H(3)S}(2)], [Cd{2-(Ph(2)PO)-6-(Me(3)Si)C(6)H(3)S}(2)(CH(3)OH)], and [Zn{PhPO(C(6)H(4)S-2)(2)}(bipy)]." Inorg Chem **38**(16): 3709-3715.

Pickering, I. J., R. C. Prince, et al. (1999). "X-ray absorption spectroscopy of cadmium phytochelatin and model systems." Biochim Biophys Acta **1429**(2): 351-64.

Pitts, K. E. and A. O. Summers (2002). "The roles of thiols in the bacterial organomercurial lyase (MerB)." Biochemistry **41**(32): 10287-96.

Rugh, C. L., H. D. Wilde, et al. (1996). "Mercuric ion reduction and resistance in transgenic Arabidopsis thaliana plants expressing a modified bacterial merA gene." Proc Natl Acad Sci U S A **93**(8): 3182-7.

Sahlman, L., A. M. Lambeir, et al. (1984). "The reaction between NADPH and mercuric reductase from Pseudomonas aeruginosa." J Biol Chem **259**(20): 12403-8.

Silver, S. and L. T. Phung (1996). "Bacterial heavy metal resistance: new surprises." Annu Rev Microbiol **50**: 753-89.

Solioz, M. and C. Vulpe (1996). "CPx-type ATPases: a class of P-type ATPases that pump heavy metals." Trends Biochem Sci **21**(7): 237-41.

Song, L., J. Caguiat, et al. (2004). "Engineered single-chain, antiparallel, coiled coil mimics the MerR metal binding site." J Bacteriol **186**(6): 1861-8.

Utschig, L. M., J. G. Wright, et al. (1993). "Biochemical and spectroscopic probes of mercury(II) coordination environments in proteins." Methods Enzymol **226**: 71-97.

Zeng, Q., C. Stalhandske, et al. (1998). "The core metal-recognition domain of MerR." Biochemistry **37**(45): 15885-95.

Figure Legends

Figure 6.1. Cd K-edge X-ray absorption spectrum (A) and Fourier transforms (k = 2 – 13 Å^{-1}; k^3 weighting) (B) of the EXAFS (inset of B) for CadA NTKII (solid) and CadA NTKII + TCEP (dashed). The proposed metal binding model is shown in the inset of A

Figure 6.2. Experimental k^3-weighted Hg EXAFS spectra (A) and its Fourier transforms (k = 2 – 12 Å^{-1}) (B) for MerB/Hg/DTT (solid) and theoretical best fit (dashed) corresponding to a coordination shell of HgS_3 using the parameters of Fit 3, Table 3.

Figure 6.3. Hg L_3-edge X-ray absorption spectrum (A) and Fourier transforms (k = 2 – 12 Å^{-1}; k^3 weighting) (B) of the EXAFS (inset of B) for MerR-*Strep*-tag (solid) and MBD-*Strep*-tag (dashed).

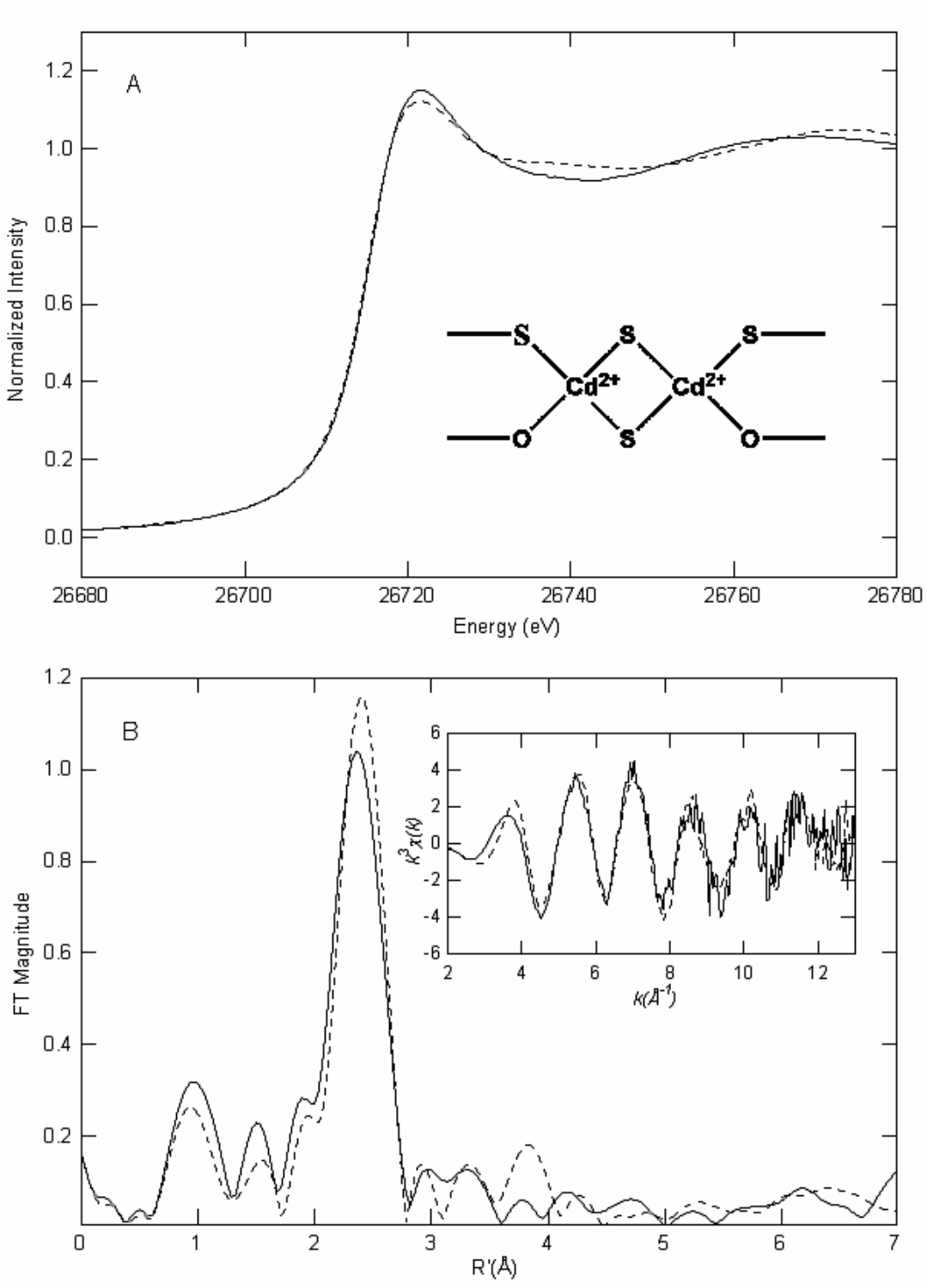
A
Normalized Intensity
Energy (eV)
S
S
S
Cd2+
Cd2+
O
S
O
B
FT Magnitude
R'(Å)
k3χ(k)
k(Å-1)

Figure 6.1

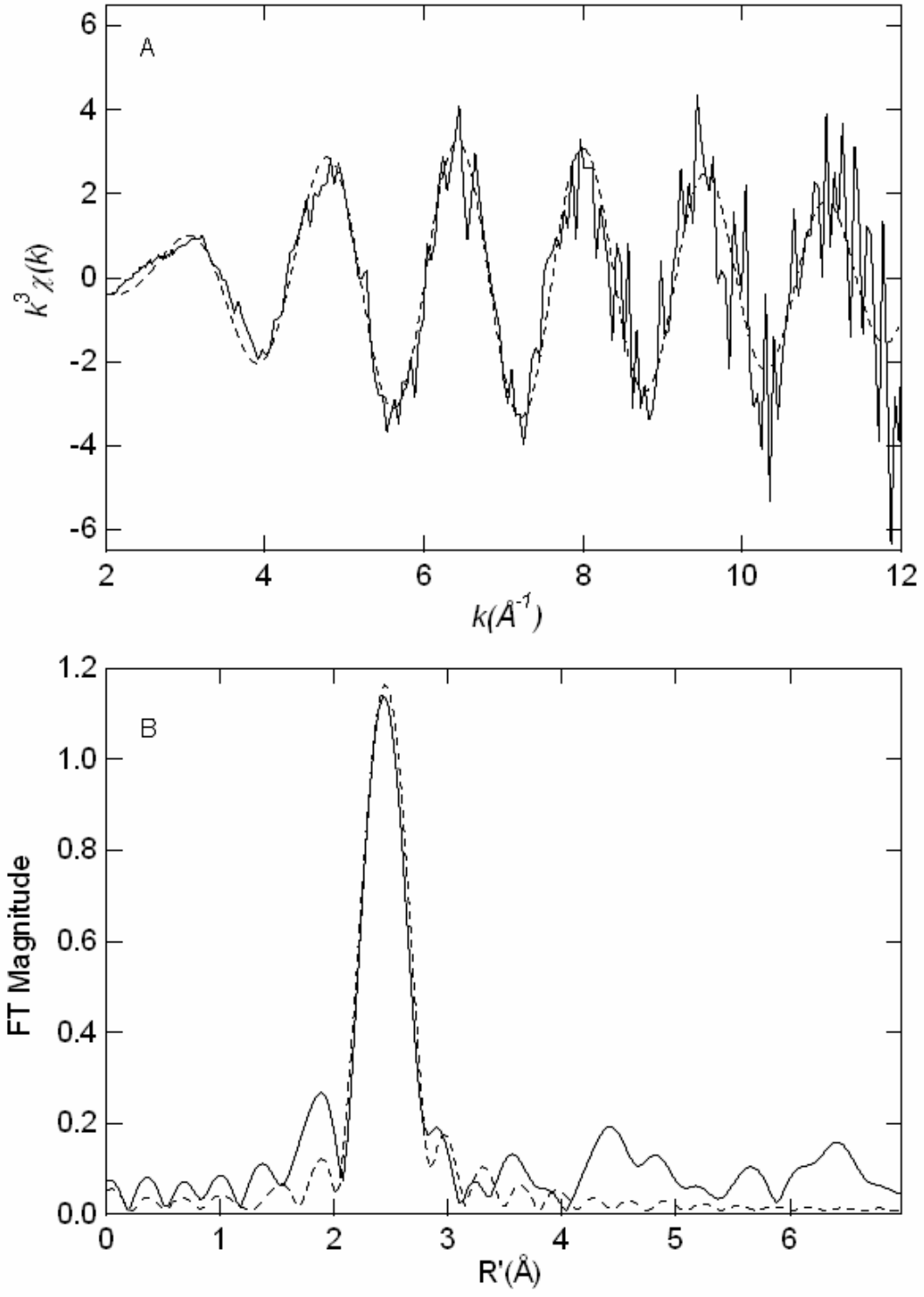

Figure 6.2

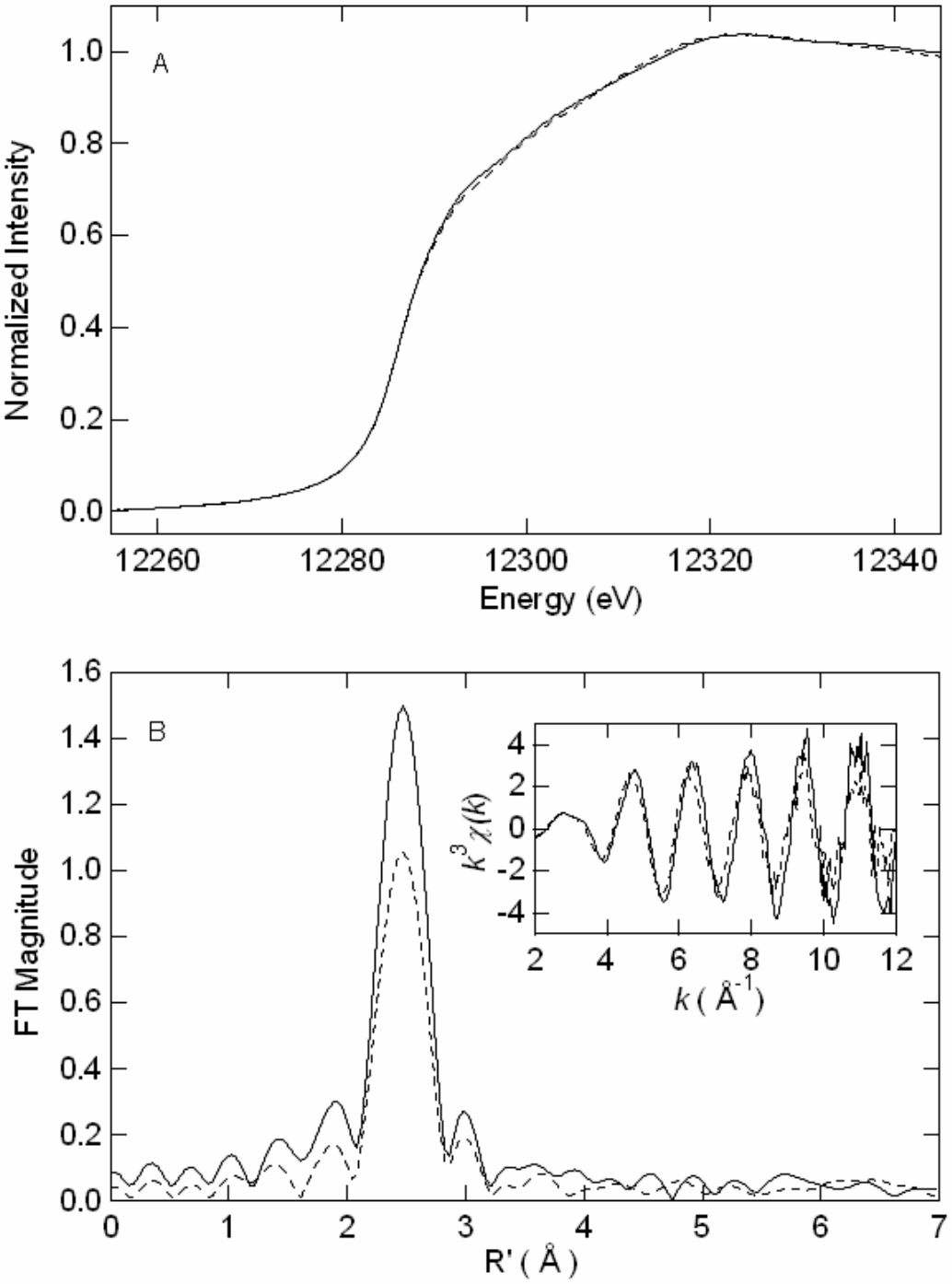
A
Normalized Intensity
1.0
0.8
0.6
0.4
0.2
0.0
12260
12280
12300
12320
12340
Energy (eV)
B
FT Magnitude
1.6
1.4
1.2
1.0
0.8
0.6
0.4
0.2
0.0
0
1
2
3
4
5
6
7
R' (Å)
$k^3\chi(k)$
4
2
0
-2
-4
2
4
6
8
10
12
k (Å^{-1})

Figure 6.3

Table 6.1. Curve fitting results for Cd EXAFS[a]

Sample filename (k range) $\Delta k^3\chi$	Fit	Shell	R_{as} (Å)	σ_{as}^2 (Å^2)	ΔE_0 (eV)	f[b]	BVS[c]
CdNTK	1	Cd-S_3	2.49	0.0054	–11.97	0.129	1.81
DNK0 (2-13 Å^{-1})	2	Cd-S_4	2.49	0.0071	–10.51	0.112	2.42
$\Delta k^3\chi$ = 8.70	3	Cd-S_3	2.51	0.0054	–7.82	0.111	2.10
		Cd-O_1	2.26	0.0023			
	4	Cd-S_2	2.54	0.0035	–4.74	0.111	1.76
		Cd-O_2	2.29	0.0028			
CdNTK + TCEP	5	Cd-S_3	2.50	0.0048	–8.00	0.093	1.77
DNKP (2-13 Å^{-1})	6	Cd-S_4	2.50	0.0065	–8.34	0.085	2.36
$\Delta k^3\chi$ = 8.02	7	Cd-S_3	2.51	0.0048	–7.36	0.085	2.12
		Cd-O_1	2.24	0.0062			
	8	Cd-S_2	2.53	0.0032	–3.50	0.087	1.79
		Cd-O_2	2.29	0.0045			
	9	Cd-S_3	2.51	0.0046	–7.07	0.077	2.12
		Cd-O_1	2.24	0.0064			
		Cd-Cd	3.66	0.0059			

[a] Shell is the chemical unit defined for the multiple scattering calculation. Subscripts denote the number of scatterers per metal. R_{as} is the metal-scatterer distance. σ_{as}^2 is a mean square deviation in R_{as}. ΔE_0 is the shift in E_0 for the theoretical scattering functions.

[b] f' is a normalized error (chi-squared):

$$f' = \frac{\left\{ \sum_i \left[k^3 \left(\chi_i^{obs} - \chi_i^{calc} \right) \right]^2 / N \right\}^{1/2}}{\left[\left(k^3 \chi^{obs} \right)_{max} - \left(k^3 \chi^{obs} \right)_{min} \right]}$$

[c] BVS=$\Sigma\exp[(r_o-r)/B]$, B=0.37,], r_0(Cd(II)-S)=2.304, , r_0(Cd(II)-O)=1.904. (Brown & Altermatt, 1993)

Table 6.2. Curve fitting results for Hg L_3 EXAFS[a]

Sample filename (k range) $\Delta k^3\chi$	Fit	Shell	R_{as} (Å)	σ_{as}^2 (Å^2)	ΔE_0 (eV)	f'[b]
MerB+Hg^{++}+DTT	1	Hg-S	2.42	–0.0010	–3.93	0.103
HBDTA (2-12 Å^{-1})	2	Hg-S_2	2.42	0.0025	–1.91	0.091
$\Delta k^3\chi$ = 10.74	3	Hg-S_3	2.43	0.0051	–0.73	0.092
	4	Hg-S_4	2.43	0.0074	–0.02	0.099

[a] Shell is the chemical unit defined for the multiple scattering calculation. Subscripts denote the number of scatterers per metal. R_{as} is the metal-scatterer distance. σ_{as}^2 is a mean square deviation in R_{as}. ΔE_0 is the shift in E_0 for the theoretical scattering functions.

[b] f' is a normalized error (chi-squared):

$$f' = \frac{\left\{ \sum_i \left[k^3 \left(\chi_i^{obs} - \chi_i^{calc} \right) \right]^2 / N \right\}^{1/2}}{\left[\left(k^3 \chi^{obs} \right)_{max} - \left(k^3 \chi^{obs} \right)_{min} \right]}$$

Table 6.3: Hg-S Bond distances of 2,-, 3-, and 4-coordinate HgS Compounds[a]

CSD code	Hg-S_2	**CSD code**	Hg-S_3	**CSD code**	Hg-S_4
BEPQAO	2.30	DELFIG	2.43	BULZUD	2.55
	2.30		2.40		2.53
BINMIU	2.36		2.51		2.52
	2.36	JEFVIZ	2.45		2.55
JETYOW	2.35		2.44	LAJGUY	2.52
	2.35		2.44		2.52
JAPROH	2.36	KELVUS	2.40		2.52
	2.36		2.46		2.52
KELWEP	2.32		2.47	NIRJIH	2.51
	2.32	KINZAI	2.40		2.54
MECBHG	2.35		2.49		2.60
	2.35		2.40		2.53
NUCFIA	2.34	VOXTOR	2.46	TPTCHG	2.51
	2.34		2.40		2.55
MEPMEP10	2.33		2.48		2.58
	2.33				2.49
MERSET01	2.34			WEMTOX	2.54
	2.34				2.56
MERMES	2.36				2.55
	2.36				2.57
NEHDOT	2.33			SLINIK	2.56

	2.35		2.56
			2.55
			2.56
Average	2.34	2.44	2.54
Standard Deviation	0.02	0.04	0.03

[a] Representative mononuclear mercuric thiolate compounds were taken from the Cambridge Structural Datbase (CSD). Bond lengths are reported in angstroms.

Table 6.4. Curve fitting results for Hg L_3 EXAFS[a]

Sample filename (k range) $\Delta k^3\chi$	Fit	Shell	R_{as} (Å)	σ_{as}^2 (Å^2)	ΔE_0 (eV)	f[b]
MerR-Hg	1	Hg-S_2	2.45	0.0001	0.27	0.053
HRO2A (2-12 Å^{-1})	2	Hg-S_3	2.45	0.0024	0.81	0.069
$\Delta k^3\chi$=8.07	3	Hg-S_4	2.45	0.0043	1.34	0.099
MBD-Hg	4	Hg-S_2	2.46	0.0027	-2.69	0.075
HD02A (2-12 Å^{-1})	5	Hg-S_3	2.46	0.0052	-2.28	0.073
$\Delta k^3\chi$=6.92	6	Hg-S_4	2.46	0.0075	-1.51	0.088

[a] Shell is the chemical unit defined for the multiple scattering calculation. Subscripts denote the number of scatterers per metal. R_{as} is the metal-scatterer distance. σ_{as}^2 is a mean square deviation in R_{as}. ΔE_0 is the shift in E_0 for the theoretical scattering functions.

[b] f' is a normalized error (chi-squared):

$$f' = \frac{\left\{\sum_i \left[k^3\left(\chi_i^{obs} - \chi_i^{calc}\right)\right]^2 / N\right\}^{1/2}}{\left[\left(k^3\chi^{obs}\right)_{max} - \left(k^3\chi^{obs}\right)_{min}\right]}$$

CHAPTER 7

CONCLUSION

The focus of my research utilizes the technique X-ray absorption spectroscopy (XAS) to characterize the binding sites of numerous transition metals in different proteins and peptides. XAS allows us to determine how many of what type of ligands are at what distance form the metal. The success of each project relies on our fruitful collaborations with many researchers around the world. Herein, I summarize projects in which I have taken part but which have not yet been mentioned, first discussing the reason for the project and then reviewing the major results of the studies and their importance.

***DapE*-encoded N-succinyl-L,L-diaminopimelic acid desuccinylase (Dr. Richard Holz, Utah State University).** The *meso*-diaminopimelate (mDAP)/lysine biosynthetic pathway offers several potential anti-bacterial targets that have yet to be explored (Scapin and Blanchard 1998). Since both products of this pathway, mDAP and lysine, are essential components for the synthesis of the peptidoglycan cell wall in Gram-negative and some Gram-positive bacteria, inhibitors of enzymes within this pathway may provide a new class of antibiotics (Levy 1998). One of the enzymes in this pathway (Velasco, Leguina et al. 2002), the *dapE*-encoded N-succinyl-L,L-diaminopimelic acid desuccinylase (DapE), catalyzes the hydrolysis of N-succinyl-L,L-diaminopimelate to L,L-diaminopimelate and succinate (Born, Zheng et al. 1998). It has been shown that deletion of the gene encoding DapE is lethal to *Helicobacter pylori* and *Mycobacterium smegmatis* (Pavelka and Jacobs 1996; Karita, Etterbeek et al. 1997). Even in the presence of lysine-supplemented media, the DapE deletion cell line of *H. pylori* was unable to

grow. Therefore, DapEs are essential for cell growth and proliferation making them potential molecular targets for a new and novel class of antibiotics. We recorded the Zn EXAFS spectra of DapE from *Haemophilus influenzae* in the presence of one or two equivalents of Zn(II) (*i.e.* [Zn_(DapE)] and [ZnZn(DapE)]). The Fourier transforms of the Zn EXAFS are dominated by a peak at *ca*. 2.0 Å, which can be fit for both [Zn_(DapE)] and [ZnZn(DapE)] assuming ca. 5 (N,O) scatterers at 1.96 and 1.98 Å, respectively. A second-shell feature at *ca.* 3.34 Å appears in the [ZnZn(DapE)] EXAFS spectrum but is significantly diminished in [Zn_(DapE)]. These data show that DapE contains a dinuclear Zn(II) active site (Figure 7.1).

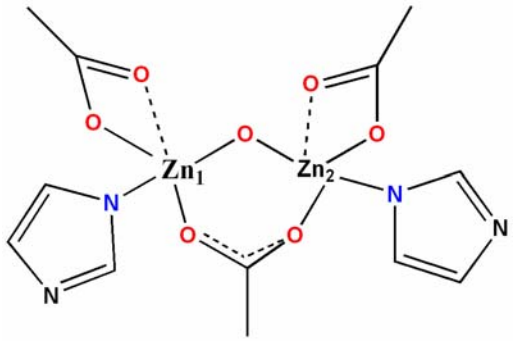

Figure 7.1. Proposed active site of DapE from *Haemophilus influenzae.*

Since no X-ray crystallographic data are available for any DapE enzyme, these data provide the first glimpse at the active site of DapE enzymes. In addition, the EXAFS data for DapE incubated with two competitive inhibitors, 2-carboxyethylphosphonic acid (CEPA) and 5-mercaptopentanoic acid, were recorded, establishing the binding modes of phosphonate- and thiolate-containing inhibitors. The structural data obtained for CEPA bound to [ZnZn(DapE)] also provides an initial understanding of the transition state for the hydrolysis reaction catalyzed by DapE. Since most pharmaceuticals target the transition state of enzymatic reactions, the structural aspects of [ZnZn(DapE)]-CEPA are particularly important for the rational design of new potent inhibitors of DapE enzymes. This work was published in *Journal of American Chemical Society* (Cosper, Bienvenue et al. 2003), and was abstracted by SSRL as one of their Science Highlights (http://www-ssrl.slac.stanford.edu/research/highlights_archive/dape.html).

Arsenate Reductase *AtACR2* Expression in Transgenic *Arabidopsis* (Dr. Richard Meagher, University of Georgia). X-ray absorption spectroscopy (XAS) was utilized to investigate the speciation of arsenic in transgenic *Arabidopsis* plant samples (As(III) vs. As(V) vs. As(III)-tris glutathione) used for phytoremediation in As-contaminated sites. The As K edge spectra illustrate that none of the plant samples analyzed contain significant (if any) arsenate (data not shown). Investigation of the FTs of the plant samples reveal highly similar data for the RNA knockdown plant samples (AtACR2Ri lines, 21-3 Plant and 3-9) and As(III)-tris-glutathione samples In contrast, the wild-type sample has a reduction in the FT peak at ~2.3 Å and a slight increase of the peak at ~1.7 Å compared to the other plants samples, suggesting that some arsenite is still present in the wild-type sample. Due to the pH dependence of As standards in the K-edge region, different XAS simulations were used to determine the percentage of arsenite in each sample (As K-edge simulation presented in Figure 7.2) (Pickering, Prince et al. 2000) . The wild-type sample was estimated to contain ~37% arsenite, while both RNA knockdown plants were estimated to contain ~17% arsenite.

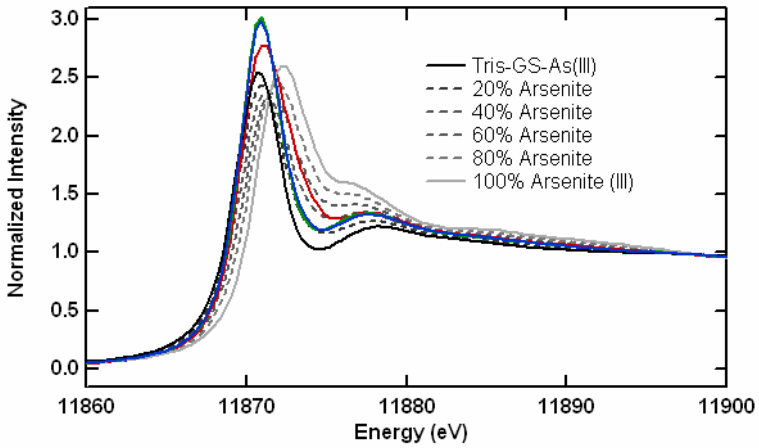

Figure 7.2. As K-edge spectra curve-fitting simulation for standards As(III)(GS)3 (gray) and arsenite (black) and individual calculated percentages (black-dashed-see legend) of arsenite. As K-edge spectra for frozen shoots from WT plants (red) and AtACR2Ri lines, 21-3 (green) and 3-9 (blue) are also shown.

The pH-dependent structural transitions of an archaeal high-potential Rieske [2Fe-2S] center (Dr. Toshio Iwasaki, Nippon Medical School). In the cytochrome bc_1/b_6f complex of aerobic respiratory chains and photosynthesis, the Rieske [2Fe-2S] center plays crucial roles in the proton acceptance and substrate binding at the quinol-oxidizing Q_o site, in relation to the protonation status of histidine N_ε (Berry, Guergova-Kuras et al. 2000; Crofts 2004). We have investigated the pH-dependent transitions of a Rieske [2Fe-2S] cluster in the hyperthermostable archaeal sulredoxin, with a specific aim of characterizing the fully deprotonated form by X-ray absorption spectroscopy. At least two alkaline species were detected with the reduced conformation, and the second transition (around pH 13) accompanies significant electronic and geometric changes of the Fe(II) site of the [2Fe-2S] cluster core, wherein the average Fe-N_{imid} bond distance of the reduced cluster decreases from 2.09 Å to 1.99 Å (Figure 7.3). The structural bias can be ascribed to the conformational adaptation of the surrounding protein, as well as deprotonation of the histidine N_ε at very alkaline pH. In contrast, these parameters remain constant at least up to pH 10. The average Fe-N_{imid} bond distance increased by ~0.08 Å upon reduction, indicating the oxidation state-dependent but essentially pH-independent changes of the [2Fe-2S] cluster core around physiological conditions.

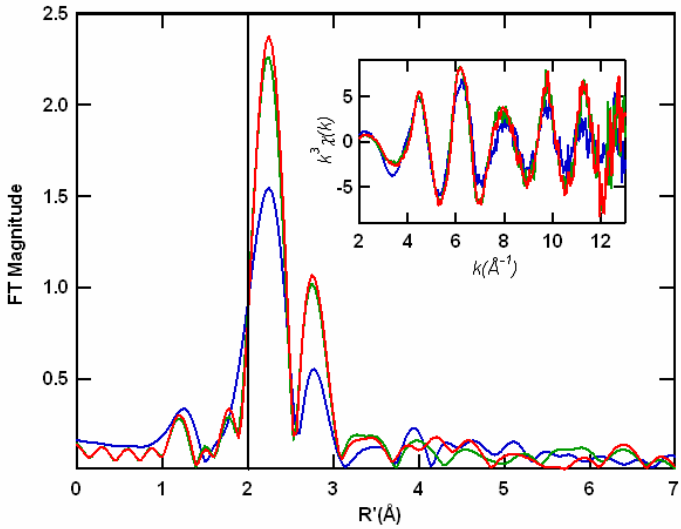

Figure 7.3. FTs (k = 2-13 $Å^{-1}$) of k^3-weighted Fe EXAFS (inset) for dithionite-reduced sulredoxin at pH 5.2 (green), 9.4 (red), and 13.2 (blue). A vertical line is drawn at R' = 2.0 Å for comparison of FT peak positions

Structural characterization of the Zn site in heterodisulfide reductase (Dr. Reiner Hedderich, MPI, Marburg). As mentioned previously, heterodisulfide reductase (HDR) is an iron-sulfur enzyme that mediates the reversible conversion of the heterodisulfide, CoM-S-S-CoB, into the sulfhydryls CoM-SH and CoB-SH in methanogenic archaea (Duin, Madadi-Kahkesh et al. 2002). The enzyme is composed of three different subunits: HdrA, HdrB, and HdrC (Hedderich, Koch et al. 1994). Moreover, metal analysis on HDR has indicated the presence of zinc. We measured Zn XAS of oxidized HdrABC, HdrABC + CoM-SH, and HdrB, clearly illustrating that HdrABC contains a Zn-site and that this Zn site is located on subunit HdrB. The data suggest similar coordination environments for Zn in the presence or absence of CoM-SH, arguing against any interaction of CoM-S$^-$ with the Zn site (Figure 7.4). It should be noted that the HdrABC + CoM-SH data suggest a slight increase of nitrogen scattering compared to the sample in the absence of CoM-SH. Comparison of the HdrB and HdrABC samples also reveals highly similar data consistent with a Zn-S_3N_1 model (Figure 7.4). These data provide the first detailed structural analysis of the Zn(II) site in HDR.

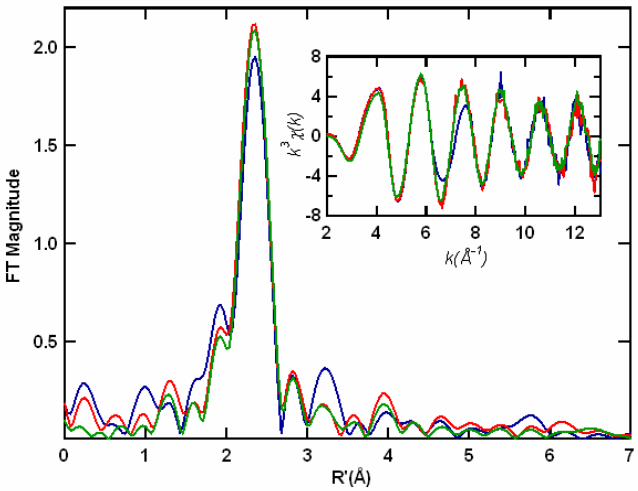

Figure 7.4. FTs (k = 2-13 Å^{-1}) of k^3-weighted Zn EXAFS for oxidized HdrABC (red), oxidized HdrABC + CoM-SH (blue), and HdrB (green)

Zinc binding to GATA proteins (Dr. James G. Omichinski, University of Montreal, and Hilary Godwin, Northwestern University). Vertebrate GATA proteins that contain a structural zinc-binding domain regulate processes that are critical for growth and development in

many species, including humans (Omichinski, Clore et al. 1993; Trainor, Omichinski et al. 1996). GATA proteins contain a N-terminal GATA finger and a C-terminal GATA finger that both require Zn for DNA binding, regulation of transcription, and protein folding (Omichinski, Clore et al. 1993). We measured Zn XAS data on the C-terminal finger from chicken GATA-1 confirming a ZnS_4 coordination environment for the active site (Ghering, Shokes et al. 2004). To help determine the Zn-S_4 coordination model, the comparative analysis method developed by Penner-Hahn and co-workers (Clark-Baldwin, Tierney et al. 1998) was used to better define *x* in a model $ZnN_{4-x}S_x$ coordination sphere (see Figure 1.2). The analysis further illustrated that the chicken GATA-1 XAS data are most consistent with a ZnS_4 model. The structural characterization of the metal site in chicken GATA-1 contributes to a more complete understanding of how Zn(II) regulates the function of these proteins in different species (Ghering, Shokes et al. 2004).

Hyperthermophilic Archaeal Rieske-type [2Fe-2S] Ferredoxin from *Sulfolobus solfataricus* (Dr. Toshio Iwasaki, Nippon Medical School). Proteins containing Rieske-type [2Fe-2S] clusters play vital roles in a number of essential biological functions, including electron transfer in respiratory chains, photosynthetic chains, and even biodegradation pathways for aromatic and alkene compounds (Mason and Cammack 1992; Trumpower and Gennis 1994; Berry, Guergova-Kuras et al. 2000). Rieske-type clusters form a redox-active site having two cysteine residues bound to one iron atom and two histidine residues coordinated to the other iron site (Beinert 2000). Our collaborators engineered two site-directed variants, His64→Cys (H64C) and His44→Cys (H44C) from the archaeal Rieske-type ferredoxin (ARF); however, only the H64C variant allowed the assembly of a stable [2Fe-2S] cluster with one histidine and three cysteine residues. Fe XAS experiments on wild-type ARF and the H64C variant reveal more

sulfur scatterers for H64C, as expected (Kounosu, Li et al. 2004). These data also illustrate the crucial role His44 plays in the formation and/or stability of Rieske-type [2Fe-2S] cluster in ARF.

In addition, Dr. Iwasaki's lab successfully designed and engineered a mononuclear iron site in sulredoxin (another Rieske-type [2Fe-2S] protein) that mimics the iron site in rubredoxin (Rd) (Iwasaki, Kounosu et al. 2005). The variant was constructed utilizing site-directed mutagenesis by replacing His 44 with Ile, Lys45 with Cys, and His64 with Cys forming a H44I/K45C/H64C variant. XAS experiments reveal identical coordination spheres for the oxidized iron-triple variant and oxidized *Clostridium pasteurianum* Fe-Rd which is known to have iron coordinated by four sulfurs (Iwasaki, Kounosu et al. 2005). These experiments present structural data for the first engineered mononuclear iron site in the Rieske-type protein scaffold, as well as a detailed look into the influence of histidine ligands on the formation and stability of Rieske-type [2Fe-2S] clusters.

[2Fe-2S] cluster degradation in hyperthermophilic archaeal succinate:caldariellaquinone oxidoreductase subunits (Dr. Toshio Iwasaki, Nippon Medical School). The biological [2Fe-2S] clusters play important roles in electron transfer and cellular signaling for a variety of organisms from archaea and bacteria to eukarya (Kent, Dreyer et al. 1982; Iverson, Luna-Chavez et al. 1999; Lancaster, Kroger et al. 1999; Page, Moser et al. 1999). The two recombinant hyperthermophilic archaeal [2Fe-2S] cluster-binding proteins, SdhC and the N-terminal domain fragment of SdhB, of *Sulfolobus tokodaii* respiratory complex II overproduced in *Escherichia coli* are thermostable as isolated, but moderately sensitive to reduction with excess dithionite (Iwasaki, Matsuura et al. 1995; Iwasaki, Wakagi et al. 1995; Iwasaki, Kounosu et al. 2002). We used iron K-edge X-ray absorption spectroscopy to monitor the structural changes of their Fe sites in the irreversible [2Fe-2S] cluster degradation process

(Li, Shokes et al. 2003). Regardless of the differences in the cluster-ligating cysteine motifs and the XAS-detectable $[2Fe\text{-}2S]^{2+}$ cluster environments, a complete reductive breakdown of the [2Fe-2S] clusters resulted in the appearance of a new Fourier transform (FT) peak at approximately 3.3 Å with a concomitant loss of the Fe-Fe interaction at ca. 2.7 Å for both proteins. On the basis of the unambiguous assignment of the 3.3 Å FT peak, our results suggest that a biological [2Fe-2S] cluster breakdown under reducing conditions generally releases Fe(II) from the polypeptide chain into the aqueous solution, binding to excess dithionite. The Fe(II) might then be recruited as a secondary ferrous iron source for de novo biosynthesis and/or regulation of iron-binding enzymes in the cellular system (Li, Shokes et al. 2003).

References

Beinert, H. (2000). "Iron-sulfur proteins: ancient structures, still full of surprises." J Biol Inorg Chem **5**(1): 2-15.

Berry, E. A., M. Guergova-Kuras, et al. (2000). "Structure and function of cytochrome bc complexes." Annu Rev Biochem **69**: 1005-75.

Born, T. L., R. Zheng, et al. (1998). "Hydrolysis of N-succinyl-L,L-diaminopimelic acid by the Haemophilus influenzae dapE-encoded desuccinylase: metal activation, solvent isotope effects, and kinetic mechanism." Biochemistry **37**(29): 10478-87.

Clark-Baldwin, K., D. L. Tierney, et al. (1998). "The limitations of X-ray absorption spectroscopy for determining the structure of zinc sites in proteins. When is a tetrathiolate not a tetrathiolate?" Journal of the American Chemical Society **120**(33): 8401-8409.

Cosper, N. J., D. L. Bienvenue, et al. (2003). "The dapE-encoded N-succinyl-l,l-diaminopimelic acid desuccinylase from Haemophilus influenzae is a dinuclear metallohydrolase." J Am Chem Soc **125**(48): 14654-5.

Crofts, A. R. (2004). "The cytochrome bc1 complex: function in the context of structure." Annu Rev Physiol **66**: 689-733.

Duin, E. C., S. Madadi-Kahkesh, et al. (2002). "Heterodisulfide reductase from Methanothermobacter marburgensis contains an active-site [4Fe-4S] cluster that is directly involved in mediating heterodisulfide reduction." Febs Letters **512**(1-3): 263-268.

Ghering, A. B., J. E. Shokes, et al. (2004). "Spectroscopic determination of the thermodynamics of cobalt and zinc binding to GATA proteins." Biochemistry **43**(26): 8346-55.

Hedderich, R., J. Koch, et al. (1994). "The heterodisulfide reductase from Methanobacterium thermoautotrophicum contains sequence motifs characteristic of pyridine-nucleotide-dependent thioredoxin reductases." Eur J Biochem **225**(1): 253-61.

Iverson, T. M., C. Luna-Chavez, et al. (1999). "Structure of the Escherichia coli fumarate reductase respiratory complex." Science **284**(5422): 1961-6.

Iwasaki, T., A. Kounosu, et al. (2002). "Novel [2Fe-2S]-type redox center C in SdhC of archaeal respiratory complex II from Sulfolobus tokodaii strain 7." J Biol Chem **277**(42): 39642-8.

Iwasaki, T., A. Kounosu, et al. (2005). "Rational design of a mononuclear metal site into the archaeal Rieske-type protein scaffold." J Biol Chem **280**(10): 9129-34.

Iwasaki, T., K. Matsuura, et al. (1995). "Resolution of the aerobic respiratory system of the thermoacidophilic archaeon, Sulfolobus sp. strain 7. I. The archaeal terminal oxidase supercomplex is a functional fusion of respiratory complexes III and IV with no c-type cytochromes." J Biol Chem **270**(52): 30881-92.

Iwasaki, T., T. Wakagi, et al. (1995). "Resolution of the aerobic respiratory system of the thermoacidophilic archaeon, Sulfolobus sp. strain 7. III. The archaeal novel respiratory complex II (succinate:caldariellaquinone oxidoreductase complex) inherently lacks heme group." J Biol Chem **270**(52): 30902-8.

Karita, M., M. L. Etterbeek, et al. (1997). "Characterization of Helicobacter pylori dapE and construction of a conditionally lethal dapE mutant." Infect Immun **65**(10): 4158-64.

Kent, T. A., J. L. Dreyer, et al. (1982). "Mossbauer studies of beef heart aconitase: evidence for facile interconversions of iron-sulfur clusters." Proc Natl Acad Sci U S A **79**(4): 1096-100.

Kounosu, A., Z. Li, et al. (2004). "Engineering a three-cysteine, one-histidine ligand environment into a new hyperthermophilic archaeal Rieske-type [2Fe-2S] ferredoxin from Sulfolobus solfataricus." J Biol Chem **279**(13): 12519-28.

Lancaster, C. R., A. Kroger, et al. (1999). "Structure of fumarate reductase from Wolinella succinogenes at 2.2 A resolution." Nature **402**(6760): 377-85.

Levy, S. B. (1998). "The challenge of antibiotic resistance." Sci Am **278**(3): 46-53.

Li, Z., J. E. Shokes, et al. (2003). "X-ray absorption spectroscopic analysis of reductive [2Fe-2S] cluster degradation in hyperthermophilic archaeal succinate:caldariellaquinone oxidoreductase subunits." Biochemistry **42**(50): 15003-8.

Mason, J. R. and R. Cammack (1992). "The electron-transport proteins of hydroxylating bacterial dioxygenases." Annu Rev Microbiol **46**: 277-305.

Omichinski, J. G., G. M. Clore, et al. (1993). "NMR structure of a specific DNA complex of Zn-containing DNA binding domain of GATA-1." Science **261**(5120): 438-46.

Page, C. C., C. C. Moser, et al. (1999). "Natural engineering principles of electron tunnelling in biological oxidation-reduction." Nature **402**(6757): 47-52.

Pavelka, M. S., Jr. and W. R. Jacobs, Jr. (1996). "Biosynthesis of diaminopimelate, the precursor of lysine and a component of peptidoglycan, is an essential function of Mycobacterium smegmatis." J Bacteriol **178**(22): 6496-507.

Pickering, I. J., R. C. Prince, et al. (2000). "Reduction and coordination of arsenic in Indian mustard." Plant Physiol **122**(4): 1171-7.

Scapin, G. and J. S. Blanchard (1998). "Enzymology of bacterial lysine biosynthesis." Adv Enzymol Relat Areas Mol Biol **72**: 279-324.

Trainor, C. D., J. G. Omichinski, et al. (1996). "A palindromic regulatory site within vertebrate GATA-1 promoters requires both zinc fingers of the GATA-1 DNA-binding domain for high-affinity interaction." Mol Cell Biol **16**(5): 2238-47.

Trumpower, B. L. and R. B. Gennis (1994). "Energy transduction by cytochrome complexes in mitochondrial and bacterial respiration: the enzymology of coupling electron transfer reactions to transmembrane proton translocation." Annu Rev Biochem **63**: 675-716.

Velasco, A. M., J. I. Leguina, et al. (2002). "Molecular evolution of the lysine biosynthetic pathways." J Mol Evol **55**(4): 445-59.